bioRxiv preprint doi: https://doi.org/10.1101/2021.11.22.469622; this version posted November 23, 2021. The copyright holder for this preprint (which was not certified by peer review) is the author/funder, who has granted bioRxiv a license to display the preprint in perpetuity. It is made available under aCC-BY-NC-ND 4.0 International license.

1 # Single-cell dissection of obesity-exercise axis in adipose-muscle tissues

2 Jiekun Yang[1,2]*, Maria Vamvini[3]*, Pasquale Nigro[3]*, Li-Lun Ho[1,2], Kiki Galani[1,2], Marcus Alva-
3 rez[4], Yosuke Tanigawa[1,2], Markku Laakso[6,7], Leandro Agudelo[1,2], Päivi Pajukanta[4,5], Roeland J.
4 W. Middelbeek[3], Kevin Grove[8], Laurie J. Goodyear[3†], Manolis Kellis[1,2†]

5 [1]Computer Science and Artificial Intelligence Laboratory, Massachusetts Institute of Technology, Cambridge, MA, USA. [2]
6 Broad Institute of MIT and Harvard, Cambridge, MA, USA. [3] Section on Integrative Physiology and Metabolism, Joslin Diabe-
7 tes Center, Harvard Medical School, Boston, MA, USA. [4] Department of Human Genetics, David Geffen School of Medicine at
8 UCLA, University of California, Los Angeles, Los Angeles, CA, USA. [5] Institute for Precision Health, David Geffen School of
9 Medicine at UCLA, University of California, Los Angeles, Los Angeles, CA, USA. [6] Institute of Clinical Medicine, Internal Medi-
10 cine, University of Eastern Finland, Kuopio, Finland. [7] Department of Medicine, Kuopio University Hospital, Kuopio, Finland. [8]
11 Novo Nordisk Research Center, Seattle, WA, USA. * Equal contributors. [†]Correspondence to: Laurie.Goodyear@joslin.har-
12 vard.edu, manoli@mit.edu

13 ## Abstract

14 Regular physical exercise has long been recognized to reverse the effects of diet-induced obesity, but
15 the molecular mechanisms mediating these multi-tissue beneficial effects remain uncharacterized.
16 Here, we address this challenge by studying the opposing effects of exercise training and high-fat diet
17 at single-cell, deconvolution and tissue-level resolutions across 3 metabolic tissues. We profile scRNA-
18 seq in 204,883 cells, grouped into 53 distinct cell subtypes/states in 22 major cell types, from subcuta-
19 neous and visceral white adipose tissue (WAT), and skeletal muscle (SkM) in mice with diet and exer-
20 cise training interventions. With a great number of mesenchymal stem cells (MSCs) profiled, we com-
21 pared depot-specific adipose stem cell (ASC) states, and defined 7 distinct fibro-adipogenic progenitor
22 (FAP) states in SkM including discovering and validating a novel CD140+/CD34+/SCA1- FAP popula-
23 tion. Exercise- and obesity-regulated proportion, transcriptional and cell-cell interaction changes were
24 most strongly pronounced in and centered around ASCs, FAPs, macrophages and T-cells. These
25 changes reflected thermogenesis-vs-lipogenesis and hyperplasia-vs-hypertrophy shifts, clustered in
26 pathways including extracellular matrix remodeling and circadian rhythm, and implicated complex sin-
27 gle- and multi-tissue communication including training-associated shift of a cytokine from binding to its
28 decoy receptor on ASCs to true receptor on M2 macrophages in vWAT. Overall, our work provides new
29 insights on the metabolic protective effects of exercise training, uncovers a previously-underappreci-
30 ated role of MSCs in mediating tissue-specific and multi-tissue effects, and serves as a model for multi-
31 tissue single-cell analyses in physiologically complex and multifactorial traits exemplified by obesity and
32 exercise training.

33 ## Introduction

34 Obesity is a complex disease with genetic, environmental and behavioral origins that poses a public
35 health problem of grave concern showing no signs of abating[1,2,3]. Key hallmarks of obesity include dys-
36 functional white adipose tissue (WAT) and chronic low-grade inflammation, which affect the function of
37 multiple organs. Obese individuals are at significantly increased risk of type 2 diabetes (T2D), cardio-
38 vascular and cerebrovascular disease, and certain types of cancers, all leading causes of death in de-
39 veloped countries[4]. Regular exercise is known to improve metabolic function in numerous tissues, and
40 to delay, prevent, or alleviate the effects of T2D, obesity, and cardiovascular disease[5]. Recent studies
41 show that exercise-induced adaptations to WAT and skeletal muscle contribute to the benefits of exer-
42 cise on health, with subcutaneous and visceral adipose depots exhibiting distinct adaptations to exer-
43 cise training[6–10].

bioRxiv preprint doi: https://doi.org/10.1101/2021.11.22.469622; this version posted November 23, 2021. The copyright holder for this preprint (which was not certified by peer review) is the author/funder, who has granted bioRxiv a license to display the preprint in perpetuity. It is made available under aCC-BY-NC-ND 4.0 International license.

44 WAT and skeletal muscle are highly heterogeneous and dynamic endocrine organs impacted by obe-
45 sity and exercise. WAT comprises mature adipocytes (~20-40% of the cellular content[11]) and the stro-
46 mal vascular fraction (SVF), that latter consisting of multiple cell types including preadipocytes, mesen-
47 chymal stem cells, and a variety of immune cells[12]. Skeletal muscle consists of myofibers, surrounded
48 by connective tissue, fibro-adipogenic progenitors (FAPs), and immune cells[13–16]. In WAT, obesity in-
49 duces inflammation, alters cellular composition, and leads to a maladaptive WAT expansion to accom-
50 modate the excessive caloric intake[17]; by contrast, exercise training stimulates WAT beiging, alters key
51 metabolic proteins, impacts tissue-tissue communication, and contributes to overall improved metabo-
52 lism[6,7,18–21]. In skeletal muscle, obesity induces altered metabolism, intramuscular fat accumulation, in-
53 creased insulin resistance, and impaired tissue regeneration and remodeling[22,23]; by contrast, training
54 induces improved regeneration potential, increased insulin sensitivity, and secretion of numerous auto-
55 crine, paracrine, or endocrine myokines mediating tissue crosstalk[24]. However, the genes and path-
56 ways mediating these opposing multi-tissue effects of exercise and obesity remain uncharacterized at
57 single-cell resolution, despite their extraordinary clinical importance for the development of new treat-
58 ments against T2D, metabolic diseases, and the obesity epidemic.

59 Here, we dissect the opposing effects of exercise training and diet-induced obesity in subcutaneous
60 WAT (scWAT), visceral WAT (vWAT), and skeletal muscle at both tissue-level and single-cell resolu-
61 tion. We study tissue-level changes across 60 samples, deconvolved changes in the most abundant
62 cell types, and single-cell changes in rarer cell types, by generating a single-cell atlas across 204,883
63 cells of 22 cell types and 53 cell states in obesity-exercise interventions across the three tissues (**Fig.
64 1a,b**). These include three distinct adipose stem cell (ASC) states in WAT depots showing shared and
65 distinct pathways and upstream regulators, and six FAP states in skeletal muscle including a previously
66 uncharacterized SCA1- subpopulation. Tissue-level analyses reveal exercise-induced upregulation of
67 lipid metabolism and cellular respiration and downregulation of immune and extracellular matrix (ECM)
68 pathways in all three tissues, and deconvolution reveals opposing changes in cell type abundance for
69 exercise training vs. obesity. Single-cell analyses reveal changes in cellular states, cell type-specific
70 gene expression/pathway/regulatory network changes, and cell-cell communication changes within and
71 across tissues. In all three tissues, exercise training leads to down-regulation of ECM remodeling and
72 up-regulation of circadian rhythmicity genes, driven primarily by mesenchymal stem cell (MSC) popula-
73 tions, and down-regulation of *Cdkn1a* and up-regulation of *Dbp* (two exercise-regulated genes) show
74 consistent genetic and transcriptional effects in human tissues. Overall, our results provide a reference
75 atlas of obesity-exercise single-cell changes in metabolic tissues, and reveal key roles for MSC in po-
76 tentially mediating tissue-specific and inter-tissue communication changes in response to obesity and
77 exercise interventions.

78 ## Results

79 ### Phenotypic response to diet-induced obesity and exercise, and profiling of three metabolic tissues

bioRxiv preprint doi: https://doi.org/10.1101/2021.11.22.469622; this version posted November 23, 2021. The copyright holder for this preprint (which was not certified by peer review) is the author/funder, who has granted bioRxiv a license to display the preprint in perpetuity. It is made available under aCC-BY-NC-ND 4.0 International license.

80 We subjected 6-week-old C57BL/6N male mice to diet-induced obesity (standard 10% vs. high-fat 60%,
81 weeks 0-6) and exercise training (sedentary vs. voluntary wheel running, weeks 3-6) interventions (**Fig.**
82 **1a,** N=51 across 4 groups). Phenotypically, high-fat-diet induced, and exercise attenuated, weight gain
83 and glucose intolerance (**Fig. 1c,f**); diet did not significantly impact running distance (**Fig. 1d**); and
84 high-fat-diet animals consumed significantly more calories, especially when sedentary (**Fig. 1e**); each
85 for both tissue-level and single-cell-level donors (**Supplementary Fig. 1a-e**).

86 We collected scWAT, vWAT and skeletal muscle (SkM) for both single-cell and tissue-level tran-
87 scriptomic profiling after fasting (6-hour) and exercise wash-out (24-hour locked wheels) to investigate
88 multi-tissue adaptations (**Fig. 1a**). For single-cell RNA-seq, we profiled 317,754 cells with 10X Ge-
89 nomics v3 across 42 libraries from 93 tissue samples (pooling 2-3 mice to obtain enough cells), captur-
90 ing 6501 cells per library, 2025 genes per cell, and 45,421 reads per cell on average (**Supplementary**
91 **Table 1**); after stringent quality control (QC), we report expression levels for a total of 17,341 genes
92 across 204,883 cells (**Table 1, Extended Data Fig. 1a, Supplementary Table 1**). For tissue-level
93 RNA-seq, we profiled 60 samples (4 groups x 5 mice x 3 tissues, no pooling), using 3′ Digital Gene Ex-
94 pression (DGE) RNA-seq. For both assays, the major drivers of variation were tissue, diet, and exer-
95 cise, but not batch (**Extended Data Fig. 1b**).

96 **Tissue-level gene and pathway alteration by obesity-exercise across three tissues**

97 We found 1386 tissue-level differentially-expressed genes (DEGs) across all three tissues (568 in
98 scWAT, 562 in vWAT, 256 in SkM; DESeq2-Negative-Binomial corrected P<0.05) and all three pairwise
99 intervention comparisons for "obesity" (high-fat vs. standard diet, for sedentary), "training" (exercise
100 training vs. sedentary, for standard diet), and "rescue" (exercise training vs. sedentary, for high-fat diet)
101 (**Table 2**, **Supplementary Table 2**), and performed gene ontology (GO) pathway enrichment, and pro-
102 tein-protein interaction (PPI) analyses to reveal common and distinct biological processes across inter-
103 ventions and tissues (**Fig. 2a-d**).

104 For the subset of DEGs identified in at least two comparisons in adipose tissues (59 in scWAT, 158 in
105 vWAT), nearly all (94%-95%) stemmed from opposite changes in obesity vs. training/rescue (**Fig. 2a-**
106 **b**). This anti-correlation held for all genes (not only DEGs), with obesity vs. rescue showing significant
107 negative correlation in both depots (Pearson scWAT $P<10^{-10}$, vWAT $P<10^{-16}$) and obesity vs. training
108 significantly anti-correlated in vWAT (Pearson $P<10^{-16}$, **Extended Data Fig. 1c**). However, the subset
109 of DEGs that met our stringent significance threshold in multiple interventions was small (10% and 28%
110 in scWAT vWAT respectively), and most DEGs were significantly-different in only one comparison (77%
111 and 59% in obesity only; 13% and 9% in rescue only; 0% and 4% in training only, in scWAT vWAT re-
112 spectively).

113 Adipose-depot DEGs included both known and novel metabolism-associated genes. Known genes in-
114 cluded obesity-upregulated and training/rescue-downregulated adiposity marker leptin[25] and browning
115 repressor *Aldh1a1*[26], obesity-downregulated and training/rescue-upregulated browning/beiging driver
116 *Ucp1*[26], metabolism regulator *Pparg*, and multiple thermogenic and browning/beiging markers (*Cidea*,

bioRxiv preprint doi: https://doi.org/10.1101/2021.11.22.469622; this version posted November 23, 2021. The copyright holder for this preprint (which was not certified by peer review) is the author/funder, who has granted bioRxiv a license to display the preprint in perpetuity. It is made available under aCC-BY-NC-ND 4.0 International license.

117 *Clstn3*, *Cox8b*, *Acsl1*, *Nr1d1*, *Adrb3*)[27,28]. Novel genes included training/rescue-upregulated circadian
118 rhythm regulators (*Dbp*, *Tef*, *Nr1d2*, *Per3*), and training/rescue down-regulated ECM remodelling genes
119 (*Thbs1*, *Sparc*).

120 For SkM (**Fig. 2c**), rescue/training up-regulated 51 genes, including fast muscle fiber marker *Myh1*[29],
121 and down-regulated 20 genes, including fat metabolism repressor *Pdk4*[30] and muscle-mass repressor
122 *Asb2*[31]. While there was a limited transcriptional response to high fat diet intervention in SkM, an obser-
123 vation previously reported in short-term high fat diet interventions[32], rescue showed significant anti-cor-
124 relation with obesity across all genes (Pearson $P<2.2x10^{-16}$, **Extended Data Fig. 1c**). Rescue also
125 showed more DEGs than training (n=164 vs. 21), suggesting a stronger response of SkM to training
126 under high-fat than standard diet. Similarly to WAT, training and rescue showed similar effect direc-
127 tions for most genes in SkM (**Extended Data Fig. 1c**).

128 These DEGs were enriched in tissue-specific pathways, including: (i) in scWAT, vessel morphogenesis
129 and cell migration (obesity: up, rescue: down), and ECM organization and insulin-like growth factor
130 (IGF) transport/uptake (obesity: up, **Fig. 2a**); (ii) in vWAT, immune pathways (obesity: up, rescue:
131 down), which included myeloid leukocyte migration, neutrophil degranulation, and antigen processing
132 and presentation (**Fig. 2b**); (iii) in SkM, muscle contraction processes and contraction-activated macro-
133 autophagy (rescue: down) (**Fig. 2c**).

134 DEGs were also enriched in three tissue-shared pathway groups, including: (i) lipid metabolism, with
135 both catabolic and anabolic fatty acid processes in all three tissues (obesity: down; rescue/training: up);
136 (ii) respiration-related pathways (obesity: down, rescue/training: up), i.e., oxidative phosphorylation and
137 detoxification of reactive oxygen species (ROS) in SkM, and cellular respiration and thermogenesis in
138 WAT, consistent with obesity-associated hypoxia when mature adipocytes expand to oxygen-diffusion
139 limit[33]; and (iii) basic metabolic processes (obesity: down, rescue: up), with monocarboxylic acid meta-
140 bolic process in WAT, and branched-chain amino acid catabolism in SkM.

141 Across tissues and interventions, DEGs clustered into biologically-meaningful modules of interacting
142 proteins (**Fig. 2d**). These include: (i) fatty acid biosynthesis/beta-oxidation/metabolism module (res-
143 cue/training up); (ii) cellular respiration modules (rescue/training up), including oxidative phosphoryla-
144 tion, TCA cycle, and ROS response; (iii) immune modules (rescue/training down), including antigen
145 presentation, neutrophil degranulation, immune cell migration, phagosome-related genes; (iv) other
146 modules (rescue/training down), including ECM-related genes, proliferation, and ribonucleotide biosyn-
147 thesis. For example, Cpt2 involved in long-chain fatty acid oxidation in the mitochondria[34] was down-
148 regulated by obesity in scWAT and up-regulated by rescue in scWAT and SkM, and Cdkn1a involved in
149 cellular senescence was down-regulated by rescue in scWAT and vWAT (**Fig. 2d**). Taken together,
150 these tissue-level results reveal the specific genes and pathways that likely mediate the known benefi-
151 cial effects of exercise training, specifically for improving fatty acid metabolism and cellular respiration
152 across all three metabolic tissues, and repressing immune, ECM, proliferation and tissue-specific path-
153 ways.

bioRxiv preprint doi: https://doi.org/10.1101/2021.11.22.469622; this version posted November 23, 2021. The copyright holder for this preprint (which was not certified by peer review) is the author/funder, who has granted bioRxiv a license to display the preprint in perpetuity. It is made available under aCC-BY-NC-ND 4.0 International license.

154 ## Single-cell atlas of metabolic tissues in obesity and exercise conditions

155 In addition to our tissue-level datasets, we also generated a single-cell atlas of 204,883 cells for obe-
156 sity-exercise interactions across the three tissues and the four intervention groups (**Fig. 3a, Extended**
157 **Data Fig. 2a-e**). To capture low-abundance cell types (e.g. ASCs in WAT, FAPs in SkM), we used a
158 single-cell library preparation that enriched for stromal vascular fraction (SVF) instead of parenchymal
159 cell types (e.g. mature adipocytes in WAT and muscle fibers in SkM) which are already well-captured
160 by tissue-level studies, and included lymph nodes in scWAT to capture immune cells migrating between
161 tissue and lymph nodes.

162 We annotated 22 cell types using marker gene expression in cell clusters (hierarchical & density-based)
163 of non-linear embeddings (tSNE, UMAP) for dimensionality-reduced data (top 50 PCs) (**Extended Data**
164 **Fig. 1a & 2f-i, Supplementary Table 3, Methods**). These include: (i) 3 types of stem cells, including
165 ASCs (MSCs in WAT), satellite cells (muscle stem cells in SkM), and FAPs (MSCs in SkM); (ii) 10
166 types of immune cells from both lymphoid and myeloid lineages; (iii) 2 types of connective cells, includ-
167 ing tenocytes in SkM and fibroblasts primarily in vWAT; (iv) 2 types of muscle cells, including muscle
168 fibers and smooth muscle cells; and (v) 4 additional cell types including endothelial, epithelial, epididy-
169 mis, and glial cells (**Fig. 3a**). Within each cell type, our analysis revealed subclusters driven by tissue
170 provenance (**Fig. 3b, Extended Data Fig. 3, Supplementary Table 4**) and to a lower degree by inter-
171 vention group (**Fig. 3c**). Integration of our single-cell data with publicly available single-cell studies high-
172 lighted the strength of our analysis to capture lower abundance cell types as described earlier (**Supple-**
173 **mentary Fig. 2**).

174 Subclustering revealed 42 cell subtypes/states for 11 (of the 22) cell types (**Extended Data Fig. 4**), dis-
175 tinguishing: (a) follicular vs. memory B-cells; (b) M1 vs. M2 macrophages; (c) T-cell subtypes including
176 CD8 naive, CD8 cytotoxic, CD4 naive, CD4 memory, T regulatory (Treg), NKT, and naive (Cd27-) vs.
177 memory (Cd27+) gamma-delta (Tgd); (d) dendritic cell (DC) subtypes conventional type 1, type 2, and
178 monocyte-derived; (e) inflammatory vs. patrolling monocytes; (f) six tenocyte subtypes, including *Pdg-*
179 *fra*+ tendon stem/progenitor cells (TSPCs), pre_Dpp4+, *Dpp4*+, *Col22a1*+, *Pappa2*+, and *Scx*-; (g) vas-
180 cular smooth muscle cells (SMCs) vs. SMC precursors vs. pericytes; (h) endothelial subtypes[35] associ-
181 ated with large vessel vs. large artery vs. capillary vs. lymphatic vessel; (i) myelinating vs. non-mye-
182 linating glial (Schwann) cells; (j) three subtypes of ASCs in WAT, including interstitial progenitor cells
183 (IPCs, marked by *Dpp4*+/*Pi16*+), committed pre-adipocytes (CPs, marked by *Icam1*+/*Fabp4*+), and adi-
184 pogenesis regulatory cells (Aregs, defined[36,37] as CD142+/*Fmo2*+), and a fourth subtype specific to
185 vWAT (pre_CP), lying between IPCs and CPs and expressing both *Dpp4* and *Icam1*; and (k) seven
186 subtypes of FAPs, which we discuss below. Two-dimensional embeddings of each tissue showed clear
187 distinctions of these cell subtypes (**Extended Data Fig. 5a-c**).

188 ## Molecular signatures of depot-specific adipose stem cell (ASC) states

bioRxiv preprint doi: https://doi.org/10.1101/2021.11.22.469622; this version posted November 23, 2021. The copyright holder for this preprint (which was not certified by peer review) is the author/funder, who has granted bioRxiv a license to display the preprint in perpetuity. It is made available under aCC-BY-NC-ND 4.0 International license.

189 We evaluated WAT transcriptional diversity as a marker of differentiation potential[38] (**Fig. 3d**). For
190 vWAT, we confirmed that IPCs show increased transcriptional diversity, consistent with their earlier dif-
191 ferentiation state[36]. In scWAT however, CPs and Aregs showed increased transcriptional diversity,
192 which may be related to their beiging and de-differentiation potential[33].

193 We sought co-expressed regulator/target-gene combinations (regulons) for each ASC subtype to gain
194 insights on their gene-regulatory circuitries. Depot-shared regulons (**Fig. 3e, blue; Supplementary Ta-**
195 **ble 6**) included: established regulons Klf3 and Creb5 for IPCs[39]; established regulons Cebpa, Pparg,
196 Gsc for CPs[39]; and for Aregs, a regulon controlled by thyroid hormone receptor beta (Thrb), whose ago-
197 nist (Resmetirom, MGL-3196) is in phase 3 clinical trial (NCT04951219) for Non-Alcoholic Fatty Liver
198 Disease (NAFLD), suggesting Resmetirom might also act on Aregs in both WAT depots.

199 Depot- and state-specific regulons included: in scWAT, IPC-highest Irx3 (lowest in CPs), consistent
200 with its early-adipocyte-differentiation role[40]; in vWAT, IPC-enriched Foxo1, consistent with its regula-
201 tory role in ASC differentiation[41]; in scWAT, Areg-enriched Nr2f2 and Meox2 regulons consistent with
202 previous results[36,37], and scWAT-specific pro-adipogenic[36] Klf5, Klf15, and Zfp467 regulons; in vWAT
203 Aregs, human- and mouse-vWAT-specific[42] (vs. scWAT) *Nr2f1*, suggesting Areg-enriched roles (in-
204 stead of pan-vWAT); in vWAT pre-CPs, potential IPC-to-CP lineage restriction (commitment) regulators
205 Foxc1, implicated in mesodermal commitment, and Nfil3, implicated in circadian rhythm and IGF-1 re-
206 ceptor signaling pathways.

207 Seven distinct fibro-adipogenic progenitor (FAP) states and a novel FAP population in skeletal mus-
208 cle

209 We classified the ~55K FAPs into seven distinct cellular states using mouse and human markers[14–16]:
210 (i) multipotent IPC_SkMs, sharing IPC markers with WAT; (ii) FAP_Cxcl14+, also found in other mouse
211 studies[14]; (iii) FAP_Prg4+, also found in human[16]; (iv) adipogenesis-regulating FAP_Aregs similar to ad-
212 ipose tissue Aregs[15]; (v) FAP post injury representing an inflammatory post-injury state; (vi) Mesoangio-
213 blasts (MABs), marked by *Alpl*+; (vii) a previously-unreported, Sca1- subpopulation of FAPs, discussed
214 in more detail below (**Extended Data Fig. 4k**). The first six subtypes were all positive for *Pdgfra*, *Cd34*
215 and *Ly6a* (**Extended Data Fig. 5d**), all seven were detectable in previous single-cell data[13,14] (**Ex-**
216 **tended Data Fig. 5e**), and all lacked *Peg3* markers of PW1+/Pax7- interstitial cells (PIC)[43] and *Abcg2*
217 markers of muscle side population cells (SP)[44] except for the population of post-injury FAPs, suggesting
218 its overlap with PICs and SPs (**Extended Data Fig. 5f**).

219 Surprisingly, while FAPs are usually defined using interchangeable combinations of canonical markers
220 *Pdgfra*+, *Cd34+,* and Sca1+, we found a new FAP population negative for Sca1 (**Extended Data Fig.**
221 **5d**)[45]. According to CytoTRACE differentiation prediction[38], Sca1- FAPs showed a more differentiated
222 state (less transcriptional diversity) than Sca1+ FAPs (**Fig. 3f**). We validated Sca1- FAPs for both tri-
223 ceps and gastrocnemius muscle by stringent fluorescence-activated cell sorting (FACS) and gating,
224 and used qPCR to verify expression of Sca1+ marker genes (*Pdgfra*, *Ly6a, Dpt*) vs Sca1- markers

bioRxiv preprint doi: https://doi.org/10.1101/2021.11.22.469622; this version posted November 23, 2021. The copyright holder for this preprint (which was not certified by peer review) is the author/funder, who has granted bioRxiv a license to display the preprint in perpetuity. It is made available under aCC-BY-NC-ND 4.0 International license.

225 (*Pdgfra*, Apoe), and lack of markers for endothelial cells (*Pecam1)*, tenocytes (*Scx)*, or glial cells (*Plp1)*
226 (**Fig. 3g, Extended Data Fig. 5g,h, Supplementary Table 7**).

227 Marker genes for the seven FAP states were enriched in shared and unique pathways (**Fig. 3h, Sup-**
228 **plementary Table 8**). Shared pathways across seven states included core matrisome, matrisome as-
229 sociated, IGF transport and uptake, and aging, suggesting FAP as a key contributor to ECM[46], IGF sig-
230 naling[47], and aging[48] in SkM. Unique pathways included: senescence, response to mechanical stimulus
231 and apoptotic signaling pathways in all states except for IPC_SkM, suggesting specific FAP states me-
232 diating muscle regeneration in response to muscle damage[49]; gliogenesis and neuron death in
233 FAP_Prg4+, MAB and Sca1- FAP, suggesting their involvement in neurodegeneration-mediated mus-
234 cle atrophy[50]; IL6-mediated signaling pathway in Sca1- FAP, highlighting its potential to promote mus-
235 cle atrophy and fibrosis[50] and mediate muscle glucose uptake, increased insulin sensitivity, and in-
236 creased fatty acid oxidation[24].

237 FAP state-specific regulons supported their respective functions (**Fig. 3i, Supplementary Table 6**): in
238 FAP_post_injury, Osr1 regulon, which marks adult FAPs activated by acute injury[51]; in FAP_Prg4+,
239 Creb5, Klf3, and Lmx1a regulons, consistent with its enriched cellular response to lipid and adipogene-
240 sis pathways[52] and suggesting its potential role in ectopic fat deposition in SkM; in MAB, Gli1 regulon,
241 consistent with a recently-reported subpopulation of FAPs with higher clonogenicity and reduced adipo-
242 genic differentiation[53]; in Sca1- FAP, Mafg and Cebpg regulons, consistent with IL6-induced oxidative
243 stress response[54].

244 **Cell-type and cell-state proportion changes in obesity and exercise across three tissues**

245 We also deconvolved[55] our tissue-level data using independent single-cell maps[13,56] refined by manu-
246 ally curation (**Supplementary Fig. 3-5**)[56]. For scWAT and vWAT (**Supplementary Fig. 6a**), deconvolu-
247 tion captured 12 cell types: mature adipocytes (22-24% of cells, consistent with previous studies[11]),
248 ASCs, smooth muscle cells, endothelial cells, pericytes, epithelial cells, glial cells, and five immune cell
249 types (B-cell, NK cell, T-cell, macrophage, neutrophils). SkM samples (**Supplementary Fig. 6b**) decon-
250 volved into 7 cell types: type II (fast) and type I (slow) myofibers (64-86% vs. 0-5% of nuclei, as ex-
251 pected for triceps[13]), mature adipocytes (5%), tenocytes, FAPs, endothelial cells, and macrophages. As
252 expected, deconvolution captured primarily high-abundance cell types, but missed the vast majority of
253 the 53 subtypes/states captured by single-cell profiling (**Supplementary Fig. 2**).

254 We used these tissue-deconvolution results to characterize cell type proportion changes in our three
255 intervention comparisons: “obesity” (high-fat vs. standard diet, in sedentary), “training” (training vs. sed-
256 entary, in standard diet), and “rescue” (comparing training vs. sedentary, in high-fat diet). In both adi-
257 pose tissues, obesity significantly decreased mature adipocytes and increased ASCs and myeloid cells
258 (**Fig. 4a,b, Extended Data Fig. 6a,c**), consistent with increased adipocyte necrosis and macrophage
259 infiltration in obesity-associated metabolic decline[33]; rescue reversed these effects in high-fat diet, even
260 though training alone showed no effect (in standard diet). Histology staining in both WAT depots
261 showed that obesity significantly enlarged mature adipocyte size (adipocyte hypertrophy) and increased

bioRxiv preprint doi: https://doi.org/10.1101/2021.11.22.469622; this version posted November 23, 2021. The copyright holder for this preprint (which was not certified by peer review) is the author/funder, who has granted bioRxiv a license to display the preprint in perpetuity. It is made available under aCC-BY-NC-ND 4.0 International license.

262 tissue weight in obesity, which were both reversed by rescue (**Fig. 4d,e**). In SkM, training and rescue
263 decreased type II (fast) myonuclei and increased FAPs, myeloid cells, and endothelial cells (**Fig. 4c**,
264 **Extended Data Fig. 6g**), as in human[16].

265 We also used our single-cell results to annotate changes in cell subtype/state proportions (**Extended**
266 **Data Fig. 6b,d**). In WAT across interventions, ASCs, macrophages and T-cells were the cell types with
267 the most subtype/state proportion changes. In obesity, we found changes in vWAT specifically, with
268 ASCs showing decreased CPs, which likely reflects both an increase in differentiation (into mature adi-
269 pocytes, up-regulated fat cell differentiation in CPs with obesity, **Fig. 4j**) and decrease in CP prolifera-
270 tion. Rescue once more reversed the change, increasing CPs in vWAT (up-regulated cell proliferation
271 in CPs with rescue, **Fig. 4j**). Integrating relative proportion with transcriptomic changes indicate obesity
272 induced compromised hyperplasia with reduced CP proliferation, and rescue restored CP proliferation
273 and improved adipogenesis in vWAT.

274 In addition to ASCs, immune cell subtypes also had relative proportion changes with obesity, training
275 and rescue in vWAT (**Extended Data Fig. 6e,f**). Obesity both increased macrophage proportion and
276 M1 (pro-inflammatory) vs. M2 (anti-inflammatory) ratio in the SVF of vWAT. Rescue restored the
277 M1/M2 ratio toward baseline. In lymphoid lineage we found an increase of Tregs and a decrease of
278 NKT cells in obesity, and these changes were reversed in rescue. Our findings are consistent with the
279 current concept of the pathogenesis of obesity as it relates to the accumulation of Tregs in vWAT[57], and
280 a protective role of NKT cells against obesity via regulatory cytokines such as interleukin (IL)-4 and IL-
281 10[58]. Furthermore, we observed similar changes of Tregs and NKT cells in training, suggesting that the
282 beneficial effects of exercise training on lymphocytes occur regardless of diet. In SkM, within the MSC
283 population, MABs significantly decreased in training and rescue, and showed a trend for an increase in
284 obesity (**Extended Data Fig. 6h**). MABs primarily differentiate into myofibers, although they present a
285 multipotent potential to differentiate into smooth muscle, adipocytes, or even osteocytes upon specific
286 signaling[59], suggesting high-fat diet and exercise training regulate lineage commitment of MABs.

287 Exercise training regulates extracellular matrix (ECM) remodelling and circadian rhythm gene ex- 288 pression across three tissues

289 We next used our single-cell data to infer cell-state-specific and cell-type-specific gene expression
290 changes modulated by high-fat diet and exercise training interventions. In WAT (**Fig. 4f,g, Extended**
291 **Data Fig. 7a, 8a, Supplementary Table 9**), we found 139 scWAT DEGs and 502 vWAT DEGs (3.6-
292 fold more than scWAT) at the cell-state-level, affecting primarily ASCs (65+457 DEGs) followed by T-
293 cells (49+29 DEGs) in both WAT depots. In ASCs, IPCs and CPs accounted for 57% and 59% of the
294 ASC DEGs in scWAT and vWAT, respectively, indicating they are the ASC states most responsive to
295 the two interventions. Between the two fat depots, obesity showed a 2.1-fold enrichment for vWAT
296 DEGs (265 vs. 35), relative to expectation (2.5-fold more DEGs in vWAT). In vWAT, rescue reversed
297 ~12% of ASC obesity DEGs, but 0% of T-cell DEGs, indicating that obesity-induced immune dysregula-
298 tion is potentially longer-lasting compared to ASCs. In SkM, we identified 290 DEGs (13 obesity+74

bioRxiv preprint doi: https://doi.org/10.1101/2021.11.22.469622; this version posted November 23, 2021. The copyright holder for this preprint (which was not certified by peer review) is the author/funder, who has granted bioRxiv a license to display the preprint in perpetuity. It is made available under aCC-BY-NC-ND 4.0 International license.

training+203 rescue, **Fig. 4h, Extended Data Fig. 9a, Supplementary Table 9**). Rescue led to more single-cell DEGs than obesity and training, consistent with our tissue-level results. Sca1+ FAP showed the most DEGs, with IPC_SkM and FAP_Areg accounting for 81% of the Sca1+ FAP DEGs. Cell-type-level DEGs showed similar patterns (**Extended Data Fig. 7b,c, 8b,c, 9b,c**).

In scWAT, pathway analysis of the DEGs indicated that obesity up-regulated core matrisome and down-regulated type I interferon signaling and defense response, which, along with the vWAT increase in M1 macrophage population, suggests a shift from adaptive immune response to inflammation (**Fig. 4i, Extended Data Fig. 7, Supplementary Table 10**). By contrast, rescue enhanced ASC renewal and interferon signaling, and suppressed T-cell-dependent inflammation, likely mediated by increased Prostaglandin E_2 levels, as evidenced by 1.5-fold decrease of prostaglandin degradation gene *Hpgd*. Consistently Prostaglandin E_2 is regulated by cell-to-cell contact, helps maintain ASC self-renewal capacity in an autocrine manner, and enhances immunomodulatory potency[60].

In vWAT, obesity up-regulated and rescue down-regulated two pathways that might mediate hypertrophy-to-hyperplasia adipocyte shifting induced by rescue (**Fig. 4j, Extended Data Fig. 8, Supplementary Table 10**): (a) TGFβ1 stimulus response, an anti-adipogenic inflammatory molecule secreted from hypertrophic, dysfunctional adipocytes and known to inhibit adipocyte differentiation in mice and humans[33]; and (b) ROS metabolic process, whose intracellular accumulation by mitochondrial respiration decreases preadipocyte differentiation[33].

In SkM, obesity up-regulated and rescue down-regulated adipogenesis, immune signaling, and ECM pathways (**Fig. 4k, Extended Data Fig. 9, Supplementary Table 10**). Although FAPs mediate pro-myogenic signals that are critical for muscle homeostasis and regeneration, in myopathies and obesity, FAP adipogenesis has been reported to be released and causing fat infiltrates[61,62]. Rescue altered adipogenesis pathways in two Sca1+ FAP states: in IPC_SkMs, rescue down-regulated adipocyte differentiation, consistent with increased Areg_FAPs (**Extended Data Fig. 6h**), which inhibit adipogenesis in SkM[15]; in Areg_FAPs however, rescue up-regulated adipogenesis pathways, including pro-adipogenic regulator *Klf15*, an Areg regulon in scWAT (but not in SkM). In the immune compartment, obesity up-regulated the IL-18 signaling pathway in conventional type 2 DCs, consistent with IL-18 increase in DCs in inflammatory myopathies[63].

Across the three tissues, ECM-related pathways were up-regulated by obesity and down-regulated by training and rescue, specifically in scWAT IPCs, all the four states of vWAT ASCs (IPC, pre_CP, CP and Areg), and three Sca1+ FAP states (IPC_SkM, Areg_FAP and MAB, **Fig. 4i-k, Extended Data Fig. 7-9, Supplementary Table 10**). WAT ASCs have been explored to generate a dermal scaffold for wound healing, which was shown to produce even more ECM components (fibronectin, collagen, etc.) than fibroblasts[70]. ECM is a highly dynamic structure that is continuously modified in response to several stimuli and energy availability. Excessive deposition of ECM components has been observed with obesity in WAT to provide structural support to the enlarged mature adipocytes and at same time promote tissue fibrosis and hypoxia. In SkM, ECM is essential for muscle development, growth and repair

bioRxiv preprint doi: https://doi.org/10.1101/2021.11.22.469622; this version posted November 23, 2021. The copyright holder for this preprint (which was not certified by peer review) is the author/funder, who has granted bioRxiv a license to display the preprint in perpetuity. It is made available under aCC-BY-NC-ND 4.0 International license.

336 and mechanical support during exercise. In addition, ECM provides a dynamic microenvironment by
337 regulating cellular behavior and fate.

338 We observed another notable pathway commonly-regulated in all three tissues and only observed in
339 single-cell data, circadian rhythm pathway. It was up-regulated by training and rescue, and enriched in
340 MSCs, including FAPs in SkM and ASCs in WAT, consistent with adiposity up-regulation by circadian
341 disruption in mouse preadipocytes[33] (**Fig. 4i-k, Extended Data Fig. 7-9, Supplementary Table 10**).
342 Upstream regulator analysis revealed *Dbp*, *Tef* and *Hlf*, three homologous PAR bZIP TFs sharing motif
343 specificity[64], as potential master regulators of these training-altered circadian pathways in specific MSC
344 states (**Extended Data Fig. 10a,b**). The Dbp regulon was up-regulated by training/rescue in scWAT
345 IPCs and vWAT CPs and Aregs. Tef was up-regulated by training/rescue and down-regulated by obe-
346 sity in vWAT IPCs and Hlf was up-regulated by training/rescue and down-regulated by obesity in SkM
347 Areg_FAPs.

348 DEGs identified using deconvolved tissue-level data were mostly regulated in opposite directions in
349 obesity vs. training/rescue, and indicated similar pathways as detected in our bulk and single-cell data
350 (**Extended Data Fig. 10c-e, Supplementary Table 11**). In scWAT, tissue-deconvolved mature adipo-
351 cytes showed significant regulation of thermogenesis genes/beige markers: obesity down-regulated
352 *Clstn3*, *Cox8b* and *Ppara*, and rescue up-regulated *Acsl1*, *Vegfa* and *Adrb3*. The enriched pathways in
353 both fat depots include lipid metabolism and transport in mature adipocytes, ECM-related pathways and
354 IGF transport and uptake in ASCs and myeloid cells, immune cell activation, regulation of inflammatory
355 response and monocyte chemotaxis in lymphoid and myeloid cells. In SkM, 44 out of the 50 tissue-de-
356 convolved DEGs were found within fast myonuclei, among which *Fbxo32* (highly expressed during
357 muscle atrophy) and *Pdk4* (observed at the tissue level and discussed above) were down-regulated
358 with both training and rescue. At the pathway level, training down-regulated tissue remodeling and up-
359 regulated VEGFA-VEGFR2 signaling, consistent with VEGF rescues muscle loss in mice[65], and rescue
360 down-regulated actin filament-based process, muscle system process, regulation of chemotaxis, lipid
361 modification, and cell growth.

362 **Exercise training reprograms within and cross-tissue cellular communication**

363 Cells function collaboratively, communicating both directly and indirectly to drive physiological re-
364 sponses to interventions across tissues. Taking advantage of our high-resolution single-cell annota-
365 tions, we used co-expression of interacting structure-based ligand-receptor pairs[66] to predict pairwise
366 cellular communication within and across tissues, and how they change in obesity, training, and rescue
367 interventions at both cell-type and cell-state levels (**Fig. 5, Extended Data Fig. 11, Supplementary**
368 **Fig. 7-10, Supplementary Table 12**).

369 Within tissues, we observed MSCs (ASCs in WAT; FAPs in SkM) function as self-regulating and cross-
370 regulating hubs of immune and non-immune cell types in individual intervention groups and in “obesity”,
371 “training”, and “rescue” comparisons (**Fig. 5a,b, Extended Data Fig. 11a,b, Supplementary Fig. 7,8**).

bioRxiv preprint doi: https://doi.org/10.1101/2021.11.22.469622; this version posted November 23, 2021. The copyright holder for this preprint (which was not certified by peer review) is the author/funder, who has granted bioRxiv a license to display the preprint in perpetuity. It is made available under aCC-BY-NC-ND 4.0 International license.

372 In both fat depots, the sedentary high-fat diet group showed more interactions between ASCs and mye-
373 loid cells (DCs and macrophages). In vWAT specifically, fibroblast showed many interactions with
374 ASCs and myeloid cells with exercise training or high-fat diet intervention. By comparing ranks of signif-
375 icant interactions overlapping intervention groups, we observed networks of differential interactions, in-
376 cluding obesity up-regulated non-immune interactions (ASC autocrine regulation in scWAT, and ASC-
377 fibroblast interactions in vWAT), training up-regulated interactions (immune-immune interactions in
378 scWAT, ASC-endothelial-fibroblast interactions in vWAT, and FAP-tenocyte interactions in SkM), and
379 rescue down-regulated immune to non-immune interactions (DC-T-ASC-fibroblast interactions in
380 vWAT, and macrophage-FAP interactions in SkM). These observations implicate obesity mostly up-reg-
381 ulating non-immune interactions involving MSCs and rescue modulating immune-MSC interactions.

382 RANK (encoded by *Tnfrsf11a*, the receptor), RANKL (encoded by *Tnfsf11*, the ligand), and OPG (en-
383 coded by *Tnfrsf11b*, osteoprotegerin, the decoy receptor of RANKL) triad showed a particularly interest-
384 ing expression change pattern in response to high-fat diet and exercise training interventions between
385 fibroblasts and ILCs in vWAT. Obesity up-regulated and training and rescue down-regulated RANKL-
386 OPG interaction (**Extended Fig. 11a**). Looking into expression patterns of the two genes across cell
387 types/states in vWAT, we found OPG was mostly expressed in ASC IPCs and fibroblasts, RANKL was
388 highly expressed in nILC2s and CD27- Tgds, and RANK was expressed mainly in M2 macrophages
389 (**Extended Fig. 11c**). Obesity increased OPG expression in fibroblasts and IPCs and RANKL expres-
390 sion in nILC2 while training and rescue decreased OPG expression (**Extended Fig. 11d**). Interestingly,
391 RANKL expression in CD27- Tgd and RANK expression in M2 macrophages showed an opposite trend
392 of changes in obesity vs. training and rescue. This led us to hypothesize that high-fat diet promoted in-
393 teraction between RANKL in nILC2 and the decoy receptor OPG in fibroblast and IPCs, and on the con-
394 trary, exercise training induced a shift from this relationship to interaction between RANKL from CD27-
395 Tgd and RANK from M2 macrophage.

396 Across tissues, we identified biologically meaningful cellular interactions with differential activities in our
397 three comparisons (**Fig. 5c,d, Extended Data Fig. 11e,f, Supplementary Fig. 9,10**). For example,
398 training increased expression of *Tgfb2* (ligand) in scWAT ASCs and *Tgfbr3* (receptor) in SkM FAPs. We
399 have shown in a previous study that TGF-β2, an exercise-induced adipokine from scWAT, is partially
400 stimulated by lactate released from SkM during exercise, and its secretion improves glucose uptake in
401 SkM[6], for which our prediction suggested a mechanism via TGF-β2 interaction with Tgfbr3 in SkM, alt-
402 hough the function of Tgfbr3 in FAP has not been studied yet[53]. Across all cross-tissue ligand-receptor
403 pairs, obesity increased communication between fat depots, while training and rescue regulated SkM-
404 WAT interactions as reported previously[24]. Although we restricted one of two interacting partners being
405 secretable and the interaction being non-integrin for this analysis, without orthogonal data types such
406 as metabolomics, lipidomics, and proteomics to provide additional evidence, the cross-tissue interac-
407 tions we predicted should be interpreted with caution, especially for interactions between the two fat de-
408 pots since they share most cell types.

bioRxiv preprint doi: https://doi.org/10.1101/2021.11.22.469622; this version posted November 23, 2021. The copyright holder for this preprint (which was not certified by peer review) is the author/funder, who has granted bioRxiv a license to display the preprint in perpetuity. It is made available under aCC-BY-NC-ND 4.0 International license.

409 **Genetics of two exercise-training candidate genes in two independent large-scale human studies**

410 To evaluate the human relevance of our results, we tested anthropometric trait genetic associations in
411 UK biobank[67] and human metabolic tissue expression changes in Metabolic Syndrome in Men
412 (METSIM) study participants[68] for two commonly up/down-regulated genes across our three tissues by
413 our tissue-level, tissue-deconvolution, and single-cell analyses (**Fig. 6a**).

414 Among 18 commonly-upregulated genes, we selected *Dbp*, a key regulator in diet/exercise-regulated
415 circadian rhythm pathways, which is up-regulated in MSCs by exercise training across all three meta-
416 bolic tissues (**Fig. 6b**), and whose homologs *Hlf* and *Tef* were also up-regulated. In human, *DBP*
417 showed a significant negative transcriptional correlation with body mass index (BMI), homeostatic
418 model assessment for insulin resistance (HOMA-IR), fasting insulin and glucose levels, C-reactive pro-
419 tein (CRP, a marker for inflammation), and waist-hip-ratio (WHR) adjusted for BMI, and a significant
420 positive correlation with Matsuda insulin sensitivity index in METSIM (**Fig. 6d,e, Extended Data Fig.**
421 **12a-f**), confirming its obesity and exercise relevance in human phenotypes.

422 Among 15 commonly-downregulated genes, we selected cell proliferation and sentence regulator
423 *Cdkn1a*, down-regulated by training/rescue primarily in MSCs in all three tissues (**Fig. 6c**), whose
424 down-regulation was consistently found with diverse experimental (bulk and single-cell) and computa-
425 tional (different single-cell pipelines) methods. *CDKN1A* showed a significant positive correlation with
426 BMI, HOMA-IR, fasting insulin levels, CRP, and WHR adjusted for BMI and a significant negative corre-
427 lation with Matsuda insulin sensitivity index in METSIM (**Fig. 6d,e**, **Extended Data Fig. 12a-f**).

428 The CDKN1A genetic locus also contained two single nucleotide polymorphisms (SNPs), one intronic
429 (rs762624) and one missense (rs2395655) in linkage disequilibrium (r^2=0.49 in EUR), significantly as-
430 sociated with body weight, fat and fat-free mass, and energy expenditure (basal metabolic rate) in the
431 UK Biobank (**Fig. 6f**). These variants were also significantly associated with hemoglobin A1C (HbA1c),
432 a marker of long-term glucose control in diabetes. The minor allele of both SNPs (C for rs762624, G for
433 rs2395655) showed protective associations with increased body fat-free mass, increased basal meta-
434 bolic rate, and lower HbA1c. These SNPs are significant splicing quantitative trait loci (QTLs) for
435 *CDKN1A* in the METSIM study, with the minor alleles increasing expression of a non-coding transcript
436 isoform (long non-coding RNA, ENST00000462537.3, **Extended Data Fig. 12g,h**). These results sug-
437 gest a potentially causal role for CDKN1A in human metabolic phenotypes, validating the human dis-
438 ease relevance of our results.

439 Discussion

440 Our study, using complementary approaches of single cell, tissue-level, and tissue-deconvolution anal-
441 yses, represents a large and comprehensive characterization of the molecular, gene-level, and path-
442 way-level underpinnings of obesity-exercise changes and interactions in three key metabolic tissues
443 (scWAT, vWAT and SkM). Our single-cell atlas with more than 200,000 cells and 53 annotated cell sub-
444 types/states enabled identification and characterization of rare cell subtypes/states, specifically MSC
445 populations in the three tissues, and revealed shared and distinct, known and novel biology of various

bioRxiv preprint doi: https://doi.org/10.1101/2021.11.22.469622; this version posted November 23, 2021. The copyright holder for this preprint (which was not certified by peer review) is the author/funder, who has granted bioRxiv a license to display the preprint in perpetuity. It is made available under aCC-BY-NC-ND 4.0 International license.

446 cell types/subtypes/states within the three tissues in response to high-fat diet and exercise training (**Fig.**
447 **1b**).

448 Enrichment of rare cell types in our single-cell protocol led to large and high-quality MSC populations
449 from all three tissues. In WAT, we uncovered IPCs, CPs, Aregs, and pre-CPs, a transitional state only
450 observed in vWAT. We identified Foxc1 and Nfil3 as possible lineage-restricting upstream regulators
451 transiently up-regulated in pre-CPs. Our gene regulator prediction for scWAT Aregs implicated regula-
452 tors supporting previously reported discrepancy of this population of ASCs: some consistent with
453 Schwalie *et al*.[37] indicating an adipogenesis inhibitory function, and others supporting an adipogenic
454 function reported by Merrick *et al*[36]. Interestingly, CPs and Aregs in scWAT showed higher transcrip-
455 tional diversity than IPCs, which contrasts the differentiation hierarchy reported before[36] and the hierar-
456 chy inferred in vWAT, but possibly provides transcriptional plasticity for beiging and dedifferentiation
457 that are uniquely observed in scWAT[33]. We also revealed depot-specific signatures of the three ASC
458 states including Irx3 and Foxo1 regulon enrichment in scWAT and vWAT IPCs, respectively.

459 In SkM, we defined seven distinct FAP states: IPC, Cxcl14 +, Prg4+, Areg, post-injury, MAB, and
460 Sca1-. Areg_FAP was shown to inhibit adipogenesis[15]. Based on the enriched pathways and GRNs,
461 Prg4+_FAP is likely to be another state involved in adipogenesis. Additionally, our identification and
462 validation of Sca1- FAP, a novel MSC population in SkM, is reminiscent of a similar population reported
463 in heart (cardiac fibrogenic SCA-1- cell)[69], which were differentiated from PDGFRα+ SCA-1+ cells and
464 showed a pathogenic role in post-myocardial infarction remodeling and arrhythmogenic cardiomyopa-
465 thy[69]. Our Sca1- FAP was possibly differentiated from Sca1+ FAP, and it is a FAP state potentially re-
466 sponsive to exercise-induced IL6 production[24].

467 Our single-cell data indicated that high-fat diet and exercise training modulate cell differentiation capa-
468 bility and proliferation rate, and gene expression of two pathways (ECM and circadian rhythm) within
469 the three tissues, in a cell-state-specific manner. We identified diet-induced compromised **hyperplasia**
470 in vWAT with decreased CP adipogenic capability and proliferation rate[36], and exercise training-en-
471 hanced CP function which led to a shift from **hypertrophy**- to hyperplasia-dominant expansion in this
472 depot. Orthogonal evidence (cell-state and deconvolved proportion and transcriptomics, and H&E stain-
473 ing) supports an exercise-driven shift from hypertrophy to hyperplasia in both adipose depots under
474 high-fat diet.

475 At the pathway level, obesity up-regulated and exercise down-regulated **ECM**-related pathways in
476 MSCs (major ECM contributors) across the three tissues. A recent report showed MSC-produced ECM
477 components potentiate MSC response to differentiation stimuli through intracellular signaling pathway
478 activation[71]. We observed the receptor tyrosine kinase (RTK) signaling pathway, a mediator of funda-
479 mental cellular and metabolic signaling pathways in response to growth factors, hormones, and cyto-
480 kines[72], tracks ECM changes in ASCs and FAPs. Interestingly, both the activity and substrate specificity
481 of RTK signaling can be strongly influenced by ECM interactions, and controlled by ECM biochemistry
482 and stiffness[73]. Besides MSCs, immune cells such as Tregs showed an up-regulation of cell adhesion

bioRxiv preprint doi: https://doi.org/10.1101/2021.11.22.469622; this version posted November 23, 2021. The copyright holder for this preprint (which was not certified by peer review) is the author/funder, who has granted bioRxiv a license to display the preprint in perpetuity. It is made available under aCC-BY-NC-ND 4.0 International license.

483 with obesity potentially through ECM interactions. We highlight ECM as a dynamic entity remodeled by
484 high-fat diet and exercise training to maintain tissue homeostasis by scaffolding and modulating differ-
485 ent cell types.

486 One notable cell-state specific exercise-regulated pathway detected in our study was the **circadian**
487 rhythm pathway, which was up-regulated by exercise training in particular MSC states of the three tis-
488 sues. We identified Dbp and its homologs Tef and Hlf as potential master regulators of the up-regulated
489 rhythmic pathway. Dbp is a PAR-domain TF with expression under circadian control, and emerging evi-
490 dence suggests Dbp as an integral component of the peripheral circadian oscillator[74]. It is one of the
491 circadian genes conserved among murine brown adipose tissue, scWAT, and vWAT[74]. Induction of *Dbp*
492 was reported to ameliorate insulin sensitivity via direct binding to the promoter region of *Pparg*, driving
493 mRNA expression of a splicing variant of *Pparg* (*Ppar-γ1sv*), and enhancing adipogenesis in preadipo-
494 cytes from ob/ob mice vWAT[75]. Promoter activity of *Dbp* as reflected by histone H3 lysine 9 acetylation
495 (H3K9ac) levels, and *Dbp* and *Pparg* expression in omental adipose tissue, were reported to be de-
496 creased in patients with T2D[76]. Our results suggest that exercise-induced circadian rhythm gene ex-
497 pression changes regulated by Dbp may contribute to adipogenesis of ASCs in WAT.

498 Single-cell data also empowered us to look into cell-cell communication within and across tissues. Our
499 within-tissue analysis of vWAT highlighted an interesting protein triad, RANK-RANKL-OPG, with high-
500 fat diet promoting interaction between RANKL in nILC2 and OPG in fibroblast and IPCs, and exercise
501 training inducing a shift from this relationship to interaction between RANKL from CD27- Tgd and
502 RANK from M2 macrophage. Although this triad has been mostly studied in bone and the immune sys-
503 tem[77], its role in WAT has been recently appreciated[78]: serum OPG is a biomarker for T2D, metabolic
504 syndrome and obesity; global knockout of OPG in mice resulted in scWAT browning, resistance to high-
505 fat diet-induced weight gain, and preserved glucose metabolism; and infusion of RANKL in wildtype
506 mice led to scWAT beiging *in vivo*, and differentiation of scWAT-derived SVF and 3T3-L1 cells, but not
507 mature white adipocytes, into beige adipose tissue[78]. Adipose tissue macrophages, the cell type ex-
508 pressing RANK receptor in our single-cell data, is a known player of beige adipogenesis as well[79]. Thus
509 our results give prominence to an exercise-induced communication shift for RANKL secreted from na-
510 ive Tgds to recruit M2 macrophages or re-polarize macrophages into an M2 state via RANK, for both
511 their anti-inflammatory and beiging-eliciting effects.

512 Taking advantage of two independent large-scale human studies, we demonstrated human transla-
513 tional values of two exercise-training-regulated genes: higher expression of *DBP* and lower expression
514 of *CDKN1A* in scWAT are associated with more desirable traits including lower BMI and HOMA-IR; mi-
515 nor alleles of two SNPs within *CDKN1A* (rs762624 and rs2395655) are associated with whole-body fat-
516 free mass and HbA1c in ~440,000 European subjects; these two variants are significant splicing-QTLs
517 with the minor alleles increasing expression of a non-coding transcript isoform of *CDKN1A* in scWAT.
518 Rs2395655 (missense) was associated with triglyceride measurement in ~300,000 multi-ethnic partici-
519 pants of the Million Veteran Program[80].

bioRxiv preprint doi: https://doi.org/10.1101/2021.11.22.469622; this version posted November 23, 2021. The copyright holder for this preprint (which was not certified by peer review) is the author/funder, who has granted bioRxiv a license to display the preprint in perpetuity. It is made available under aCC-BY-NC-ND 4.0 International license.

520 We envision several future directions for extending our study: (1) Surveying endocrine, cognitive, and
521 other functions beyond the metabolic tissues surveyed here; (2) studying sex-specific adaptations[8] be-
522 yond the male mice surveyed here; (3) adding two additional carolic intervention groups of high-caloric-
523 intake exercise and low-carolic-intake no-exercise, to untangle the effects of caloric intake vs. exercise,
524 as training impacted caloric intake in the high-fat-diet group; (4) distinguishing tissue-resident vs. circu-
525 lating immune cells in scWAT by sampling lymph nodes vs. scWAT separately; (5) varying the length of
526 high-fat diet and exercise, and the specific diet and exercise types; (6) testing mice of different ages;
527 and (7) profiling epigenomic, splicing, proteomic, metabolomic, lipidomic, phosphorylation, and other
528 molecular phenotypes.

529 Overall, our work provides a comprehensive and high-quality single-cell obesity-exercise interaction at-
530 las in three metabolic tissues. We derived new insights on the metabolic protective effects of exercise
531 training at single-cell transcriptome and interaction levels. We uncovered both a novel MSC population
532 in SkM and a previously-underappreciated role of MSCs in potentially mediating tissue-specific and
533 multi-tissue obesity and exercise training effects, with promise for new therapeutics development
534 against obesity.

535 ## Tables

536 **Table 1. Number of cells and samples per tissue and phenotypic group used for analysis.**

	Sedentary Std. Diet	Training Std. Diet	Sedentary High Fat Diet	Training High Fat Diet	Tissue Total
Subcutaneous White Adipose Tissue (scWAT)	10,952 cells 3 samples*	18,005 cells 4 samples	12,783 cells 3 samples	16,501 cells 3 samples	58,241 cells 13 samples
Visceral White Adipose Tissue (vWAT)	18,668 cells 3 samples	20,869 cells 4 samples	11,725 cells 3 samples	27,598 cells 3 samples	78,860 cells 13 samples
Skeletal Muscle (SkM)	10,969 cells 3 samples	21,969 cells 4 samples	11,403 cells 3 samples	23,441 cells 4 samples	67,782 cells 14 samples
Total					204,883 cells 40 samples

537 *each sample is a cell suspension

538 **Table 2. Tissue-level differentially expressed genes (DEGs) with high-fat diet and exercise train-**
539 **ing interventions**

	Obesity (Sed. High-fat vs Sed. Std.)	Training (Train Std. vs Sed. Std.)	Rescue (Train High-fat vs Sed. High-fat)	
Common in WAT	**Up: 76; Dn: 75**	**Up: 3; Dn: 0**	**Up: 24; Dn: 17**	**195 (176 unique genes)**
scWAT	Up: 269; Dn: 223	Up: 3; Dn: 0	Up: 70; Dn: 62	627 (568 unique genes)
vWAT	Up: 237; Dn: 241	Up: 19; Dn: 28	Up: 72; Dn: 133	730 (562 unique genes)
SkM	Up: 0; Dn: 0	Up: 64; Dn: 28	Up: 147; Dn: 88	327 (256 unique genes)
	970	142	572	1684 (1386 unique genes)

bioRxiv preprint doi: https://doi.org/10.1101/2021.11.22.469622; this version posted November 23, 2021. The copyright holder for this preprint (which was not certified by peer review) is the author/funder, who has granted bioRxiv a license to display the preprint in perpetuity. It is made available under aCC-BY-NC-ND 4.0 International license.

540 ## Materials and methods

541 ### Abbreviations

542 In many of the figure legends, abbreviations are used for tissues, intervention groups, cell types/sub-
543 types/states. scWAT, subcutaneous white adipose tissue; vWAT, visceral white adipose tissue; SkM,
544 skeletal muscle; sed, sedentary; train, exercise training; std. diet, standard diet; HFD, high-fat diet;
545 ASC, adipose stem cell; FAP, fibro-adipogenic progenitor; sate, satellite cell; DC, dendritic cell; NF,
546 neutrophil; ILC, innate lymphoid cell; MF, macrophage; mono, monocyte; NK, natural killer cell; teno,
547 tenocyte; SMC, smooth muscle cell; EC, endothelial cell; EP, epithelial cell; epidi, epididymis; follicular,
548 follicular B-cell; memory, memory B-cell; M1, M1 macrophage; M2, M2 macrophage; CD8 naive, CD8
549 naive T-cell; CD8 cyto, CD8 cytotoxic T-cell; CD4 naive, CD4 naive T-cell; CD4 memory, CD4 memory
550 T-cell; Treg, regulatory T-cell; NKT, natural killer T-cell; Tgd CD27+, memory gamma-delta T-cell; Tgd
551 CD27-, naive gamma-delta T-cell; cDC1, conventional type 1 dendritic cell; cDC2, conventional type 2
552 dendritic cell; moDC, monocyte-derived dendritic cell; inflammatory, inflammatory monocyte; patrolling,
553 patrolling monocyte; TSPC, tendon stem/progenitor cells; pre_Dpp4+, transitional Dpp4+ tenocyte;
554 Dpp4+, Dpp4+ tenocyte; Col22a1+, Col22a1+ tenocyte; Pappa2+, Pappa2+ tenocyte; Scx low, Scx-low
555 tenocyte; vSMC, vascular smooth muscle cell; precursor, smooth muscle precursor cell; large vessel,
556 large vessel endothelial cell; large artery, large artery endothelial cell; capillary, capillary endothelial
557 cell; lymphatic, lymphatic vessel endothelial cell; myelinating, myelinating glial cell; non-myelinating,
558 non-myelinating glial cell; IPC WAT, interstitial progenitor cell in white adipose tissue; pre_CP, transi-
559 tional committed preadipocyte; CP, committed preadipocyte; Areg, adipogenesis regulatory/CD142+
560 cell; IPC SkM, interstitial progenitor cell in skeletal muscle; FAP Cxcl14+, Cxcl14+ fibro-adipogenic pro-
561 genitor; FAP Prg4+, Prg4+ fibro-adipogenic progenitor; FAP Areg, adipogenesis regulatory/CD142+ fi-
562 bro-adipogenic progenitor; FAP post injury, post-injury/inflammatory fibro-adipogenic progenitor; MAB,
563 mesoangioblast; FAP_Sca1-, Sca1- fibro-adipogenic progenitor.

564 ### Mouse cohort

565 All experiments were conducted following NIH guidelines and protocols were approved by the Institu-
566 tional Animal Care and Use Committee at Joslin Diabetes Center in Boston, MA. C57BL/6N mice were
567 purchased from the Charles River Laboratories and were housed in singular cages at room tempera-
568 ture (23°c) on a 12 h/12 h light/dark cycle in an AAALAC-approved animal facility at Joslin Diabetes
569 Center. We used 6-week-old male mice for this experiment. For the first 3 weeks, all mice were seden-
570 tary, and half of the mice were fed a chow standard diet (10% kcal fat; 9F5020-LabDiet, Pharma-
571 Serv,Inc.) and the other half a high-fat diet (60% kcal fat; (9F5020-LabDiet, PharmaServ,Inc.) ad libi-
572 tum. High-fat feeding was used as a robust model for the development of impaired glucose tolerance.
573 At the start of week 4, mice were further divided into sedentary and training groups, resulting in four
574 groups: sedentary chow-fed; exercise training chow- fed; sedentary high-fat fed; and exercise training
575 high-fat fed. The mouse cohort consisted of 60 mice: 12 in each sedentary group (12 chow;12 high-fat)
576 and 18 in each training group (18 chow;18 high-fat). Exercise training was done by housing mice in in-
577 dividual cages containing a running wheel. Mice had free access to the wheel at all times, and running

bioRxiv preprint doi: https://doi.org/10.1101/2021.11.22.469622; this version posted November 23, 2021. The copyright holder for this preprint (which was not certified by peer review) is the author/funder, who has granted bioRxiv a license to display the preprint in perpetuity. It is made available under aCC-BY-NC-ND 4.0 International license.

578 distance was recorded daily. Sedentary mice were individually housed in standard cages. All mice had
579 body weights measured every two days. After 21 days, mice underwent a glucose tolerance test (GTT)
580 after a 12-hour fast. Seven days later (day 28), the wheels of the trained mice were locked. Twenty-four
581 hours later, following a 6-hour fast, mice were anesthetized with 5% v/v Isoflurane (NDC 60307-120,
582 Piramal Healthcare) using EZ-150C anesthesia machine (E-Z Systems, Inc.) and blood was drawn by
583 heart puncture. Perigonadal visceral (vWAT) and inguinal subcutaneous white adipose tissue (scWAT)
584 and triceps muscle were rapidly dissected and were either snap frozen or processed fresh to generate
585 cell suspension.

586 **Bulk mRNA sequencing**

587 For the whole-tissue RNAseq, also known as bulkRNAseq, we euthanized 5 mice per group and har-
588 vested inguinal and perigonadal WAT as well as triceps. These tissues were snap frozen in liquid nitro-
589 gen immediately after collection. Total RNA was extracted at the Goodyear lab using an RNA extrac-
590 tion kit (Direct-zol™ RNA MiniPrep, Zymo Research). 10ng of total RNA quantified and quality as-
591 sessed by Advanced Analytical Fragment Analyzer was used for library preparation on Tecan Evo150.
592 3′ DGE-custom primers 3V6NEXT-bmc#1-12 were added to a final concentration of 1 uM. (5'-/5Bi-
593 osg/ACACTCTTTCCCTACACGACGCTCTTCCGATCT[BC6]N10T30VN-3' where 5Biosg = 5' biotin,
594 [BC6] = 6bp barcode specific to each sample/well, N10 = Unique Molecular Identifiers, Integrated DNA
595 technologies), to generate two subpools of 15 samples each. After addition of the oligonucleotides,
596 Maxima H Minus RT was added per manufacturer's recommendations with Template-Switching oligo
597 5V6NEXT (10uM, [5V6NEXT : 5'-iCiGiCACACTCTTTCCCTACACGACGCrGrGrG-3' where iC: iso-dC,
598 iG: iso-dG, rG: RNA G]) followed by incubation at 42℃ for 90' and inactivation at 80℃ for 10'. Follow-
599 ing the template switching reaction, cDNA from 12 wells containing unique well identifiers were pooled
600 together and cleaned using RNA Ampure beads at 1.0X. cDNA was eluted with 17 ul of water followed
601 by digestion with Exonuclease I at 37℃ for 30 minutes, and inactivated at 80℃ for 20 minutes.

602 Second strand synthesis and PCR amplification was done by adding the Advantage 2 Polymerase Mix
603 (Clontech) and the SINGV6 primer (10 pmol, Integrated DNA Technologies 5'-/5Biosg/ACAC-
604 TCTTTCCCTACACGACGC-3') directly to the exonuclease reaction. Eight cycles of PCR were per-
605 formed followed by clean up using regular SPRI beads at 0.6X, and eluted with 20ul of elution buffer
606 (Qiagen). Successful amplification of cDNA was confirmed using the Fragment Analyzer.
607 Illumina libraries were then produced using standard Nextera tagmentation substituting P5NEXTPT5-
608 bmc primer (25µM, Integrated DNA Technologies, (5'-AATGATACGGCGACCACCGAGATCTACAC-
609 TCTTTCCCTACACGACGCTCTTCCG*A*T*C*T*-3' where * = phosphorothioate bonds.) in place of
610 the normal N500 primer. Final libraries were cleaned using SPRI beads at 0.7X and quantified using
611 the Fragment Analyzer and qPCR before being loaded for sequencing using the Hiseq 2000 (Illumina,
612 Inc) in 50bp single-end mode at the BioMicro Center at MIT.

613 **Single-cell RNA sequencing**

bioRxiv preprint doi: https://doi.org/10.1101/2021.11.22.469622; this version posted November 23, 2021. The copyright holder for this preprint (which was not certified by peer review) is the author/funder, who has granted bioRxiv a license to display the preprint in perpetuity. It is made available under aCC-BY-NC-ND 4.0 International license.

614 Tissues from 2-3 mice were pooled to achieve >1x10^6 analyzable cells (final sample size per group= 3-
615 4). Fresh tissues were enzymatically digested and dissociated according to tissue dissociation kit proto-
616 cols (adipose tissue Cat No 130-105-808, skeletal muscle Cat No 130-098-305 by Miltenyi) using the
617 gentleMACS™ Dissociator (Miltenyi). Dissociated tissues were filtered, centrifuged, and the isolated
618 cells were resuspended in 0.1% BSA in PBS and immediately processed for the generation of single-
619 cell RNA (scRNA) libraries using the droplet-based RNA sequencing technology. Briefly, 5000-6000
620 cells were profiled per sample using the Chromium Single Cell 3' RNA reagent kit v3 according to the
621 10X Genomics protocol. The generated cDNA libraries were indexed, pooled, and sequenced in three
622 batches using the NovaSeq 6000 S2 system and reagent kits (100 cycles) (Illumina, Inc) at the BioMi-
623 cro Center Core at MIT.

624 **Analysis of bulk mRNA-seq data**

625 **Pre-processing and DE analysis:** Six FASTQ files for each sample were concatenated for read de-
626 duplication using unique molecular identifiers (UMIs). We then ran Salmon 0.14.2[81] to quantify the num-
627 ber of unique reads for each transcript against Ensembl version 98 mouse transcripts. The transcript
628 level information was summarized to the gene-level using R package tximport[82]. We then clustered all
629 the samples across three tissues unbiasedly to observe potential batch effects and sample outliers.
630 Next for each tissue, genes with a count greater than 10 in all the samples were retained, and differen-
631 tial gene expression analysis for our three comparisons was carried out using R package DESeq2[83].
632 We used Independent Hypothesis Weighting (IHW)[84] to adjust p values and adaptive shrinkage estima-
633 tor (ashr)[85] to adjust fold changes from DESeq2 results. We called significant DEGs at an adjusted p
634 value cutoff of 0.05 (**Supplementary Table 2**).

635 **Deconvolution:** We performed deconvolution on bulk mRNA-seq data using CIBERSORTx[86] and in
636 reference to two publicly available datasets[13,56]: one is a scRNA-seq data in scWAT and the other is a
637 snRNA-seq data in skeletal muscle. We integrated and re-annotated the scWAT scRNA-seq dataset as
638 shown in **Supplementary Fig. 3 and 4**, and confirmed original cell type annotation for the skeletal mus-
639 cle snRNA-seq dataset (**Supplementary Fig. 5**). We ran CIBERSORTx using default parameters for all
640 three analysis modules, including creating signature matrices using the two reference datasets, imput-
641 ing cell fractions, and sample-level gene expression using our bulk data. We calculated expression
642 changes for genes with imputed expression levels in the three comparisons using the Wilcoxon rank
643 sum test.

644 **scRNA-seq data analysis**

645 **Pre-processing, clustering and annotation:** Gene count matrices for each single-cell sample were
646 generated by aligning reads to the mm10 genome (refdata-gex-mm10-2020-A) using 10X Genomics
647 Cell Ranger software v4.0.0 (**Supplementary Table 1**). We clustered pseudo-bulk profiles of individual
648 single-cell samples to determine potential batch effects, and excluded one low-quality sample based on
649 unbiased clustering results. Then for each sample, we removed ambient RNA contamination using

bioRxiv preprint doi: https://doi.org/10.1101/2021.11.22.469622; this version posted November 23, 2021. The copyright holder for this preprint (which was not certified by peer review) is the author/funder, who has granted bioRxiv a license to display the preprint in perpetuity. It is made available under aCC-BY-NC-ND 4.0 International license.

650 SoupX[87] with a fixed contamination fraction of 20%. The 20% fixed threshold performed the best com-
651 pared to no ambient RNA removal, automatic removal implemented in SoupX, 10% and 15% fixed
652 thresholds, and threshold estimated using hemoglobin genes, to reach a desirable de-contaminated
653 visualization and keep the most number of cells. We then excluded low-quality cells using four QC met-
654 rics: (i) number of genes with non-zero expression fewer than 500; (ii) number of UMIs fewer than 200
655 or more than 6000; (iii) percentage of reads mapping to mitochondrial genes more than 10; and (iv)
656 number of reads mapped to Mki67 more than 0. We removed potential cell doublets using Doublet-
657 Finder[88] with default parameters and 3.1% homotypic doublet proportion estimation based on statistics
658 published by 10X Genomics. Next we integrated all the 41 samples across three tissues together for an
659 atlas, and samples belonging to a single tissue together for tissue-specific maps. Integration was done
660 without any batch correction using Seurat v3[89]. We used "sctransform" in Seurat for data normalization,
661 performed principal component analysis (PCA) to obtain the first 50 PCs, used the 50 PCs to build
662 community, and clustered the cells using both a graph-based clustering approach as implemented in
663 Seurat v3 and a density-based clustering approach in R package dbscan[90]. Visualization of the tissue-
664 and atlas-level datasets was through non-linear dimensional reduction techniques such as tSNE and
665 UMAP. We adjusted processing steps for tSNE in reference to this paper[91]. We then annotated cell
666 clusters using SciBet[92], SingleR[93], and cell type-specific markers from *Tabula Muris*[94] and tissue-fo-
667 cused studies in the field[14,36,95,96]. For unknown cell type subclusters like Sca1- FAP, we identified cell
668 type-specific markers using the "FindMarkers" function in Seurat with an expression cutoff of 25% in
669 either of the two tested populations. We further subsetted each cell type and performed sub-clustering
670 within the cell type to identify cell subtypes/states. We annotated identified cell subtypes/states refer-
671 encing markers from the literature (**Supplementary Table 3**).

672 **DE analysis:** We performed cell-type- and cell-state-specific differential expression (DE) analysis on
673 "pseudo-bulk" profiles, generated by summing counts together for all cells with the same combination of
674 cell type/state and sample. This approach leverages the resolution offered by single-cell technologies to
675 define cell types/states, and combines it with the statistical rigor of existing methods for DE analysis in-
676 volving a small number of samples[97]. The DE analysis was performed using quasi-likelihood (QL) meth-
677 ods from the edgeR package[98]. We removed cell type/state and sample combinations containing fewer
678 than 10 cells. Cell-type/state-specific DEGs were determined using an FDR cutoff of 0.05 (**Supplemen-
679 tary Table 9**).

680 **Cellular communication:** For within- and cross-tissue communication prediction, we exported gene-
681 by-cell count matrices and cell type/state assignment for each cell as two input files for CellPhoneDB
682 "statistical analysis"[66]. CellPhoneDB is a publicly available repository of curated receptors, ligands and
683 their interactions with the advantage of taking subunit architecture into consideration. We then imported
684 CellPhoneDB results into R, merged interactions identified in each sample, and compared rank and
685 mean values for all the interacting partners of an interaction in our three defined comparisons ("obe-

bioRxiv preprint doi: https://doi.org/10.1101/2021.11.22.469622; this version posted November 23, 2021. The copyright holder for this preprint (which was not certified by peer review) is the author/funder, who has granted bioRxiv a license to display the preprint in perpetuity. It is made available under aCC-BY-NC-ND 4.0 International license.

686 sity", "training", and "rescue"). Specifically for cross-tissue interactions, we forced ligands to be secreta-
687 ble and interactions to be non-integrin. We then derived log2 fold changes using mean value, and cal-
688 culated statistical significance on ranks using the Wilcoxon rank sum test implemented in base R. Inter-
689 actions with a nominal p value of 0.1 were plotted using RCy3 package[99] and Cytoscape (**Supplemen-**
690 **tary Table 12**).

691 **Gene regulatory network and CytoTRACE:** We inferred per-sample GRNs using SCENIC with GRN-
692 Boost implementation in Python[100], and detected regulons with differential activities between interven-
693 tion groups using the Wilcoxon rank sum test. We estimated differentiation stages of ASCs and FAPs
694 using the script provided with the CytoTRACE framework[38]. All the QC steps and analysis performed on
695 single-cell data were illustrated and summarized in **Extended Data Fig. 1a**.

696 ## Histology

697 Representative samples of scWAT and vWAT were fixed with 3.7% formaldehyde for 24hrs and then
698 stored in 70% ethanol at 4°C. Five-micrometer-thick tissue sections were stained with hematoxylin and
699 eosin (Richard Allan Scientific) and relative adipocyte size was estimated at 20 fold magnification of 5
700 random fields using an inverted fluorescence microscope (IX51Olympus). CellProfiler 3.0 (http://cellpro-
701 filer.org) was used for the automatic measurement.

702 ## FACS-based cell isolation, RNA isolation and quantitative PCR

703 Single cell suspension passed through 40 um (FisherBrand) and dead cell removal MS column (Mil-
704 tenyi Biotec) were stained with anti-CD45 BV650 antibody (1:100, Biolegend), anti-CD34 PE antibody
705 (1:100, Biolegend), anti-CD140 PE-Cy7 (1;100, Biolegend), anti-SCA1 BV421 (1:100, Biolegend) in
706 PBS containing 0.1% BSA at 4°C for 30 min. After 3 times of washing, Cytox green (1:100, Invitrogen)
707 was added as a dead cell marker. Live CD140+ SCA1+ and CD140+SCA- cells from CD45-CD34+
708 populations were sorted on Aria II (BD biosciences), and the RNA were isolated using Trizol in combi-
709 nation with miRNeasy kit (Qiagen). 15 ul of elution buffer was used to elute RNA, and we performed
710 qRT-PCR using RNA to Ct kit on Quant Studio 7 (Thermo Scientific) to detect gene differentially ex-
711 pressed in CD140+SCA1+ and CD140+SCA1-.

712 ## METSIM and UK Biobank analysis

713 **METSIM RNA-seq:** All participants provided informed consent and the study was approved by the eth-
714 ics committee of the University of Eastern Finland. The METSIM cohort consists of 10,197 Finnish men
715 with detailed metabolic phenotyping[68]. Among these, we analyzed 335 participants with RNA-seq data
716 from subcutaneous adipose tissue biopsies. Reads were mapped using STAR v2.5.2b[101] to the
717 GRCh38 genome with Gencode[102] v26 as a transcriptome annotation. Gene read counts were calcu-
718 lated using FeatureCounts. We performed transcriptome-wide differential expression for insulin, glu-
719 cose, Homa-IR, C-reactive protein (CRP), free fatty acids (FFA), Matsuda index, BMI, and waist-hip ra-
720 tio adjusted for BMI (WHRadjBMI). All phenotypes except WHRadjBMI were log-transformed to induce
721 an approximate normal distribution. To improve power, we included RIN, the first PC, and sequencing
722 batch as covariates. Normalization factors for library size were calculated using Trimmed Mean of M-

bioRxiv preprint doi: https://doi.org/10.1101/2021.11.22.469622; this version posted November 23, 2021. The copyright holder for this preprint (which was not certified by peer review) is the author/funder, who has granted bioRxiv a license to display the preprint in perpetuity. It is made available under aCC-BY-NC-ND 4.0 International license.

723 values (TMM). To perform DE, we used edgeR v3.22.5[98] with the quasi-likelihoods to fit the models and
724 obtain p-values. P-values were adjusted for multiple testing using FDR.

725 **METSIM isoform QTL:** To estimate isoform transcript abundance, we ran Kallisto[103] using Gencode
726 v26 as a transcriptome reference. Isoform QTLs were detected with FastQTL[104]. Isoform transcripts per
727 million (TPM) estimates from Kallisto were rank transformed to a standard normal distribution. FastQTL
728 was run using RIN, batch, and the first 35 PCs as covariates. To determine the number of PCs, a QTL
729 analysis was run on chromosome 21 with successively larger numbers of PCs as covariates. We se-
730 lected 35 as this roughly maximized the number of isoform QTLs. We extracted nominal p-values and
731 corrected for multiple testing as follows. For each isoform, we corrected SNP-isoform p-values using
732 Benjamini-Hochberg. Then, we corrected the q-values for the number of isoforms tested using Bonfer-
733 roni.

734 **UK Biobank:** To assess the phenome-wide associations of the genetic variants in *Dbp* and *Cdkn1a*
735 across anthropometric and metabolic traits, we investigated GWAS summary statistics across 8 vari-
736 ants in the two candidate genes and 108 traits in UK Biobank. Briefly, we focused on meta-analyzed
737 GWAS summary statistics on directly genotyped arrays[105] across a total of 451,354 individuals consist-
738 ing of white British (n = 337,129), non-British white (n = 44,632), African (n = 6,497), South Asian (n =
739 7,831), East Asian (n = 1,704), semi-related (n = 44,632), and admixed (n = 28,656) individuals, de-
740 fined from a combination of genotype PCs and self-reported ancestry as described elsewhere[106,107].
741 The association summary statistics was visualized with R 'ggforestplot' package (https://nightin-
742 galehealth.github.io/ggforestplot/index.html) and is available as a part of Global Biobank Engine[108].

743 ## Other computational analyses and data processing remarks

744 Enrichment analysis was performed using the web server Metascape with default parameters[109]. All the
745 heatmaps were generated using R package ComplexHeatmap[110]. All computational analyses were per-
746 formed using R version 3.4.0. All Wilcoxon rank sum tests were unpaired and two-sided. All two way
747 ANOVA followed by Tukey multiple comparison tests were generated in GraphPad Prism v9. All box
748 plots were generated and displayed in R, using the geom_boxplot() function with default parameters.
749 The median value is indicated with a black line, and a coloured box (hinges) is drawn between the 1st
750 and 3rd quartiles (interquartile range, IQR). The whiskers correspond to no further than 1.5 x IQR from
751 the hinge and outliers are omitted. All bar plots for phenotype analysis were generated and displayed in
752 Prism, which display mean values as centres and the standard deviation as error bars. All included mi-
753 croscopy images are representative.

754 ## Data availability

755 All raw and processed bulk mRNA-seq and scRNA-seq data have been uploaded in the GEO database
756 (https://www.ncbi.nlm.nih.gov/gds) with the accession numbers xxx and xxx. We also provide an inter-
757 active data and analysis browser for all the data at xxx.

758 ## Code availability

759 Analysis code is available at xxx.

bioRxiv preprint doi: https://doi.org/10.1101/2021.11.22.469622; this version posted November 23, 2021. The copyright holder for this preprint (which was not certified by peer review) is the author/funder, who has granted bioRxiv a license to display the preprint in perpetuity. It is made available under aCC-BY-NC-ND 4.0 International license.

760 ## Acknowledgements

761 We thank Minna Kaikkonen-Määttä for advice and feedback on the work. We thank Stuart Levine for
762 generating high-quality data and technical support. We thank Carlos Castorena and Angie Bookout for
763 discussions and feedback on the high-fat diet and exercise training-regulated genes. We thank Karen
764 Mohlke for analysis advice on the METSIM cohort. We thank Charlie Whittaker for help with bulk 3′
765 DGE data processing. We thank Ashley Renfro, Nicholas Carbone and Julio Mantero for experimental
766 support. We thank all the members of the Kellis lab at MIT, the Goodyear lab at Joslin Diabetes Center,
767 and the Kaikkonen-Määttä lab at University of Eastern Finland for feedback on the work. This work was
768 supported by Novo Nordisk Research Center, Seattle, WA, USA. J.Y. was supported by the National
769 Institutes of Health (NIH) National Institute of Diabetes and Digestive and Kidney Diseases (NIDDK)
770 grant T32-DK110919. M.V. was supported by the NIH NIDDK grants T32-DK007260 and F32-
771 DK126432. R.J.W.M. was supported by the NIH NIDDK grant K23-DK114550. L.J.G. was supported by
772 R01DK099511, and 5P30-DK-36836. M.K. was supported by U24DK112331, U24HG009446, and
773 UG3NS115064.

774 ## Author Contributions

775 This study was designed and directed by L.J.G. and M.K. M.V. and P. N. performed the mouse proto-
776 col. M.V., P.N., L.H., and K.Ga. collected the tissues. K.Ga. performed the scRNA-seq experiment. J.Y.
777 performed data processing and computational analysis. M.A. performed analysis in the METSIM study.
778 M.L., and P.P. designed and directed the METSIM study. Y.T. performed analysis in UK Biobank. M.V.,
779 P.N., and L.H. performed validation experiments. M.K., L.A., R.J.W.M., and K.Gr. provided scientific
780 feedback. J.Y., M.V., P.N., L.J.G., and M.K. wrote the manuscript.

bioRxiv preprint doi: https://doi.org/10.1101/2021.11.22.469622; this version posted November 23, 2021. The copyright holder for this preprint (which was not certified by peer review) is the author/funder, who has granted bioRxiv a license to display the preprint in perpetuity. It is made available under aCC-BY-NC-ND 4.0 International license.

References

1. Heymsfield, S. B. & Wadden, T. A. Mechanisms, Pathophysiology, and Management of Obesity. *N. Engl. J. Med.* **376**, 254–266 (2017).
2. Ward, Z. J. *et al.* Projected U.S. State-Level Prevalence of Adult Obesity and Severe Obesity. *N. Engl. J. Med.* **381**, 2440–2450 (2019).
3. CDC. Data & Statistics. https://www.cdc.gov/obesity/data/index.html (2021).
4. Bray, G. A. Medical consequences of obesity. *J. Clin. Endocrinol. Metab.* **89**, 2583–2589 (2004).
5. Kirwan, J. P., Sacks, J. & Nieuwoudt, S. The essential role of exercise in the management of type 2 diabetes. *Cleve. Clin. J. Med.* **84**, S15–S21 (2017).
6. Takahashi, H. *et al.* TGF-β2 is an exercise-induced adipokine that regulates glucose and fatty acid metabolism. *Nature Metabolism* vol. 1 291–303 (2019).
7. Stanford, K. I., Middelbeek, R. J. W. & Goodyear, L. J. Exercise Effects on White Adipose Tissue: Beiging and Metabolic Adaptations. *Diabetes* vol. 64 2361–2368 (2015).
8. Nigro, P. *et al.* Exercise Training Promotes Sex-Specific Adaptations in Mouse Inguinal White Adipose Tissue. *Diabetes* vol. 70 1250–1264 (2021).
9. Trevellin, E. *et al.* Exercise training induces mitochondrial biogenesis and glucose uptake in subcutaneous adipose tissue through eNOS-dependent mechanisms. *Diabetes* **63**, 2800–2811 (2014).
10. Effect of a long-term behavioural weight loss intervention on nephropathy in overweight or obese adults with type 2 diabetes: a secondary analysis of the Look AHEAD randomised clinical trial. *The Lancet Diabetes & Endocrinology* **2**, 801–809 (2014).
11. Adipose Tissue. https://www.sciencedirect.com/topics/agricultural-and-biological-sciences/adipose-tissue.
12. Stenkula, K. G. & Erlanson-Albertsson, C. Adipose cell size: importance in health and disease. *Am. J. Physiol. Regul. Integr. Comp. Physiol.* **315**, R284–R295 (2018).
13. Dos Santos, M. *et al.* Single-nucleus RNA-seq and FISH identify coordinated transcriptional activity in mammalian myofibers. *Nat. Commun.* **11**, 5102 (2020).
14. Oprescu, S. N., Yue, F., Qiu, J., Brito, L. F. & Kuang, S. Temporal Dynamics and Heterogeneity of Cell Populations during Skeletal Muscle Regeneration. *iScience* **23**, 100993 (2020).
15. Camps, J. *et al.* Interstitial Cell Remodeling Promotes Aberrant Adipogenesis in Dystrophic Muscles. *Cell Rep.* **31**, 107597 (2020).
16. Rubenstein, A. B. *et al.* Single-cell transcriptional profiles in human skeletal muscle. *Sci. Rep.* **10**, 229 (2020).
17. Fuster, J. J., Ouchi, N., Gokce, N. & Walsh, K. Obesity-Induced Changes in Adipose Tissue Microenvironment and Their Impact on Cardiovascular Disease. *Circ. Res.* **118**, 1786–1807 (2016).
18. Stanford, K. I. & Goodyear, L. J. Muscle-Adipose Tissue Cross Talk. *Cold Spring Harb. Perspect. Med.* **8**, (2018).
19. Pedersen, B. K. & Febbraio, M. A. Muscle as an endocrine organ: focus on muscle-derived interleukin-6. *Physiol. Rev.* **88**, 1379–1406 (2008).
20. Dong, J. *et al.* Inhibition of myostatin in mice improves insulin sensitivity via irisin-mediated cross talk between muscle and adipose tissues. *Int. J. Obes.* **40**, 434–442 (2016).
21. Boström, P. *et al.* A PGC1-α-dependent myokine that drives brown-fat-like development of white fat and thermogenesis. *Nature* **481**, 463–468 (2012).
22. De Micheli, A. J., Spector, J. A., Elemento, O. & Cosgrove, B. D. A reference single-cell transcriptomic atlas of human skeletal muscle tissue reveals bifurcated muscle stem cell populations. *Skelet. Muscle* **10**, 19 (2020).
23. Akhmedov, D. & Berdeaux, R. The effects of obesity on skeletal muscle regeneration. *Frontiers in Physiology* vol. 4 (2013).
24. Castillo-Armengol, J., Fajas, L. & Lopez-Mejia, I. C. Inter-organ communication: a gatekeeper for metabolic health. *EMBO Rep.* **20**, e47903 (2019).
25. Bouassida, A. *et al.* Leptin, its implication in physical exercise and training: a short review. *J. Sports Sci. Med.* **5**, 172–181 (2006).
26. Kiefer, F. W. *et al.* Retinaldehyde dehydrogenase 1 regulates a thermogenic program in white adipose tissue. *Nat. Med.* **18**, 918–925 (2012).
27. Long, J. Z. *et al.* A smooth muscle-like origin for beige adipocytes. *Cell Metab.* **19**, 810–820 (2014).
28. Zeng, X. *et al.* Innervation of thermogenic adipose tissue via a calsyntenin 3β–S100b axis. *Nature* **569**, 229–235 (2019).

bioRxiv preprint doi: https://doi.org/10.1101/2021.11.22.469622; this version posted November 23, 2021. The copyright holder for this preprint (which was not certified by peer review) is the author/funder, who has granted bioRxiv a license to display the preprint in perpetuity. It is made available under aCC-BY-NC-ND 4.0 International license.

29. Leinwand, L. A., Saez, L., McNally, E. & Nadal-Ginard, B. Isolation and characterization of human myosin heavy chain genes. *Proc. Natl. Acad. Sci. U. S. A.* **80**, 3716–3720 (1983).
30. Kim, Y. I., Lee, F. N., Choi, W. S., Lee, S. & Youn, J. H. Insulin regulation of skeletal muscle PDK4 mRNA expression is impaired in acute insulin-resistant states. *Diabetes* **55**, 2311–2317 (2006).
31. Davey, J. R. *et al.* Integrated expression analysis of muscle hypertrophy identifies Asb2 as a negative regulator of muscle mass. *JCI Insight* **1**, (2016).
32. de Wilde, J. *et al.* An 8-week high-fat diet induces obesity and insulin resistance with small changes in the muscle transcriptome of C57BL/6J mice. *J. Nutrigenet. Nutrigenomics* **2**, 280–291 (2009).
33. Ghaben, A. L. & Scherer, P. E. Adipogenesis and metabolic health. *Nat. Rev. Mol. Cell Biol.* **20**, 242–258 (2019).
34. Rufer, A. C., Thoma, R. & Hennig, M. Structural insight into function and regulation of carnitine palmitoyltransferase. *Cell. Mol. Life Sci.* **66**, 2489–2501 (2009).
35. Kalucka, J. *et al.* Single-Cell Transcriptome Atlas of Murine Endothelial Cells. *Cell* **180**, 764–779.e20 (2020).
36. Merrick, D. *et al.* Identification of a mesenchymal progenitor cell hierarchy in adipose tissue. *Science* **364**, (2019).
37. Schwalie, P. C. *et al.* A stromal cell population that inhibits adipogenesis in mammalian fat depots. *Nature* **559**, 103–108 (2018).
38. Gulati, G. S. *et al.* Single-cell transcriptional diversity is a hallmark of developmental potential. *Science* **367**, 405–411 (2020).
39. Farmer, S. R. Transcriptional control of adipocyte formation. *Cell Metab.* **4**, 263–273 (2006).
40. Claussnitzer, M. *et al.* FTO Obesity Variant Circuitry and Adipocyte Browning in Humans. *N. Engl. J. Med.* **373**, 895–907 (2015).
41. Higuchi, M. *et al.* Differentiation of human adipose-derived stem cells into fat involves reactive oxygen species and Forkhead box O1 mediated upregulation of antioxidant enzymes. *Stem Cells Dev.* **22**, 878–888 (2013).
42. Gesta, S. *et al.* Evidence for a role of developmental genes in the origin of obesity and body fat distribution. *Proc. Natl. Acad. Sci. U. S. A.* **103**, 6676–6681 (2006).
43. Mitchell, K. J. *et al.* Identification and characterization of a non-satellite cell muscle resident progenitor during postnatal development. *Nat. Cell Biol.* **12**, 257–266 (2010).
44. Meeson, A. P. *et al.* Cellular and molecular regulation of skeletal muscle side population cells. *Stem Cells* **22**, 1305–1320 (2004).
45. Joe, A. W. B. *et al.* Muscle injury activates resident fibro/adipogenic progenitors that facilitate myogenesis. *Nat. Cell Biol.* **12**, 153–163 (2010).
46. Chapman, M. A., Mukund, K., Subramaniam, S., Brenner, D. & Lieber, R. L. Three distinct cell populations express extracellular matrix proteins and increase in number during skeletal muscle fibrosis. *Am. J. Physiol. Cell Physiol.* **312**, C131–C143 (2017).
47. Giuliani, G., Rosina, M. & Reggio, A. Signaling pathways regulating the fate of fibro/adipogenic progenitors (FAPs) in skeletal muscle regeneration and disease. *FEBS J.* (2021) doi:10.1111/febs.16080.
48. Ancel, S., Mashinchian, O. & Feige, J. N. Adipogenic progenitors keep muscle stem cells young. *Aging* **11**, 7331–7333 (2019).
49. Saito, Y., Chikenji, T. S., Matsumura, T., Nakano, M. & Fujimiya, M. Exercise enhances skeletal muscle regeneration by promoting senescence in fibro-adipogenic progenitors. *Nat. Commun.* **11**, 889 (2020).
50. Asakura, A. Faculty Opinions recommendation of Denervation-activated STAT3-IL-6 signalling in fibro-adipogenic progenitors promotes myofibres atrophy and fibrosis. *Faculty Opinions – Post-Publication Peer Review of the Biomedical Literature* (2019) doi:10.3410/f.733703117.793559648.
51. Stumm, J. *et al.* Odd skipped-related 1 (Osr1) identifies muscle-interstitial fibro-adipogenic progenitors (FAPs) activated by acute injury. *Stem Cell Res.* **32**, 8–16 (2018).
52. Sue, N. *et al.* Targeted disruption of the basic Krüppel-like factor gene (Klf3) reveals a role in adipogenesis. *Mol. Cell. Biol.* **28**, 3967–3978 (2008).
53. Contreras, O., Rossi, F. M. V. & Theret, M. Origins, potency, and heterogeneity of skeletal muscle fibro-adipogenic progenitors—time for new definitions. *Skeletal Muscle* vol. 11 (2021).
54. Forcina, L. *et al.* Increased Circulating Levels of Interleukin-6 Affect the Redox Balance in Skeletal Muscle. *Oxid. Med. Cell. Longev.* **2019**, 3018584 (2019).
55. Newman, A. M. *et al.* Robust enumeration of cell subsets from tissue expression profiles. *Nat. Methods* **12**, 453–457 (2015).

bioRxiv preprint doi: https://doi.org/10.1101/2021.11.22.469622; this version posted November 23, 2021. The copyright holder for this preprint (which was not certified by peer review) is the author/funder, who has granted bioRxiv a license to display the preprint in perpetuity. It is made available under aCC-BY-NC-ND 4.0 International license.

56. Rajbhandari, P. *et al.* Single cell analysis reveals immune cell–adipocyte crosstalk regulating the transcription of thermogenic adipocytes. *Elife* **8**, e49501 (2019).
57. Matarese, G., Procaccini, C., De Rosa, V., Horvath, T. L. & La Cava, A. Regulatory T cells in obesity: the leptin connection. *Trends Mol. Med.* **16**, 247–256 (2010).
58. Satoh, M. & Iwabuchi, K. Role of Natural Killer T Cells in the Development of Obesity and Insulin Resistance: Insights From Recent Progress. *Front. Immunol.* **9**, 1314 (2018).
59. Quattrocelli, M. *et al.* Mouse and human mesoangioblasts: isolation and characterization from adult skeletal muscles. *Methods Mol. Biol.* **798**, 65–76 (2012).
60. Lee, B.-C. *et al.* PGE2 maintains self-renewal of human adult stem cells via EP2-mediated autocrine signaling and its production is regulated by cell-to-cell contact. *Scientific Reports* vol. 6 (2016).
61. Reggio, A. *et al.* Adipogenesis of skeletal muscle fibro/adipogenic progenitors is affected by the WNT5a/GSK3/β-catenin axis. *Cell Death Differ.* **27**, 2921–2941 (2020).
62. Jia, G. & Sowers, J. R. Increased Fibro-Adipogenic Progenitors and Intramyocellular Lipid Accumulation in Obesity-Related Skeletal Muscle Dysfunction. *Diabetes* vol. 68 18–20 (2019).
63. Tucci, M., Quatraro, C., Dammacco, F. & Silvestris, F. Increased IL-18 Production by Dendritic Cells in Active Inflammatory Myopathies. *Annals of the New York Academy of Sciences* vol. 1107 184–192 (2007).
64. Yoshitane, H. *et al.* Functional D-box sequences reset the circadian clock and drive mRNA rhythms. *Commun Biol* **2**, 300 (2019).
65. Grunewald, M. *et al.* Counteracting age-related VEGF signaling insufficiency promotes healthy aging and extends life span. *Science* **373**, (2021).
66. Efremova, M., Vento-Tormo, M., Teichmann, S. A. & Vento-Tormo, R. CellPhoneDB: inferring cell–cell communication from combined expression of multi-subunit ligand–receptor complexes. *Nat. Protoc.* **15**, 1484–1506 (2020).
67. Sudlow, C. *et al.* UK biobank: an open access resource for identifying the causes of a wide range of complex diseases of middle and old age. *PLoS Med.* **12**, e1001779 (2015).
68. Laakso, M. *et al.* The Metabolic Syndrome in Men study: a resource for studies of metabolic and cardiovascular diseases. *J. Lipid Res.* **58**, 481–493 (2017).
69. Soliman, H. *et al.* Pathogenic Potential of Hic1-Expressing Cardiac Stromal Progenitors. *Cell Stem Cell* **26**, 459–461 (2020).
70. Paganelli, A., Benassi, L., Rossi, E. & Magnoni, C. Extracellular matrix deposition by adipose-derived stem cells and fibroblasts: a comparative study. *Arch. Dermatol. Res.* **312**, 295–299 (2020).
71. Novoseletskaya, E. *et al.* Mesenchymal Stromal Cell-Produced Components of Extracellular Matrix Potentiate Multipotent Stem Cell Response to Differentiation Stimuli. *Front Cell Dev Biol* **8**, 555378 (2020).
72. Zhao, M., Jung, Y., Jiang, Z. & Svensson, K. J. Regulation of Energy Metabolism by Receptor Tyrosine Kinase Ligands. *Front. Physiol.* **11**, 354 (2020).
73. Hastings, J. F., Skhinas, J. N., Fey, D., Croucher, D. R. & Cox, T. R. The extracellular matrix as a key regulator of intracellular signalling networks. *Br. J. Pharmacol.* **176**, 82–92 (2019).
74. Zvonic, S. *et al.* Characterization of peripheral circadian clocks in adipose tissues. *Diabetes* **55**, 962–970 (2006).
75. Suzuki, C. *et al.* Induction of Dbp by a histone deacetylase inhibitor is involved in amelioration of insulin sensitivity via adipocyte differentiation in ob/ob mice. *Chronobiol. Int.* **36**, 955–968 (2019).
76. Ushijima, K. *et al.* Expression of clock gene Dbp in omental and mesenteric adipose tissue in patients with type 2 diabetes. *BMJ Open Diabetes Res Care* **8**, (2020).
77. Ono, T., Hayashi, M., Sasaki, F. & Nakashima, T. RANKL biology: bone metabolism, the immune system, and beyond. *Inflamm. Regen.* **40**, 2 (2020).
78. Matsuo, F. S. *et al.* RANKL induces beige adipocyte differentiation in preadipocytes. *Am. J. Physiol. Endocrinol. Metab.* **318**, E866–E877 (2020).
79. Li, Y., Yun, K. & Mu, R. A review on the biology and properties of adipose tissue macrophages involved in adipose tissue physiological and pathophysiological processes. *Lipids Health Dis.* **19**, 164 (2020).
80. Klarin, D. *et al.* Genetics of blood lipids among\ 300,000 multi-ethnic participants of the Million Veteran Program. *Nat. Genet.* **50**, 1514–1523 (2018).
81. Patro, R., Duggal, G., Love, M. I., Irizarry, R. A. & Kingsford, C. Salmon provides fast and bias-aware quantification of transcript expression. *Nat. Methods* **14**, 417–419 (2017).
82. Soneson, C., Love, M. I. & Robinson, M. D. Differential analyses for RNA-seq: transcript-level estimates improve gene-level inferences. *F1000Res.* (2015).

bioRxiv preprint doi: https://doi.org/10.1101/2021.11.22.469622; this version posted November 23, 2021. The copyright holder for this preprint (which was not certified by peer review) is the author/funder, who has granted bioRxiv a license to display the preprint in perpetuity. It is made available under aCC-BY-NC-ND 4.0 International license.

83. Love, M. I., Huber, W. & Anders, S. Moderated estimation of fold change and dispersion for RNA-seq data with DESeq2. *Genome Biol.* **15**, 550 (2014).
84. Ignatiadis, N., Klaus, B., Zaugg, J. B. & Huber, W. Data-driven hypothesis weighting increases detection power in genome-scale multiple testing. *Nat. Methods* **13**, 577–580 (2016).
85. Stephens, M. False discovery rates: a new deal. *Biostatistics* **18**, 275–294 (2017).
86. Newman, A. M. *et al.* Determining cell type abundance and expression from bulk tissues with digital cytometry. *Nat. Biotechnol.* **37**, 773–782 (2019).
87. Young, M. D. & Behjati, S. SoupX removes ambient RNA contamination from droplet-based single-cell RNA sequencing data. *Gigascience* **9**, (2020).
88. McGinnis, C. S., Murrow, L. M. & Gartner, Z. J. DoubletFinder: Doublet Detection in Single-Cell RNA Sequencing Data Using Artificial Nearest Neighbors. *Cell Syst* **8**, 329–337.e4 (2019).
89. Hafemeister, C. & Satija, R. Normalization and variance stabilization of single-cell RNA-seq data using regularized negative binomial regression. *Genome Biol.* **20**, 296 (2019).
90. Hahsler, M., Piekenbrock, M. & Doran, D. dbscan: Fast Density-Based Clustering with R. *Journal of Statistical Software, Articles* **91**, 1–30 (2019).
91. Kobak, D. & Berens, P. The art of using t-SNE for single-cell transcriptomics. *Nat. Commun.* **10**, 5416 (2019).
92. Li, C. *et al.* SciBet as a portable and fast single cell type identifier. *Nat. Commun.* **11**, 1818 (2020).
93. Aran, D. *et al.* Reference-based analysis of lung single-cell sequencing reveals a transitional profibrotic macrophage. *Nat. Immunol.* **20**, 163–172 (2019).
94. Tabula Muris Consortium *et al.* Single-cell transcriptomics of 20 mouse organs creates a Tabula Muris. *Nature* **562**, 367–372 (2018).
95. Giordani, L. *et al.* High-Dimensional Single-Cell Cartography Reveals Novel Skeletal Muscle-Resident Cell Populations. *Mol. Cell* **74**, 609–621.e6 (2019).
96. Ramirez, A. K. *et al.* Single-cell transcriptional networks in differentiating preadipocytes suggest drivers associated with tissue heterogeneity. *Nat. Commun.* **11**, 2117 (2020).
97. Amezquita, R. A. *et al.* Orchestrating single-cell analysis with Bioconductor. *Nat. Methods* **17**, 137–145 (2020).
98. Robinson, M. D., McCarthy, D. J. & Smyth, G. K. edgeR: a Bioconductor package for differential expression analysis of digital gene expression data. *Bioinformatics* **26**, 139–140 (2010).
99. Gustavsen, J. A., Pai, S., Isserlin, R., Demchak, B. & Pico, A. R. RCy3: Network biology using Cytoscape from within R. *F1000Res.* **8**, 1774 (2019).
100. Aibar, S. *et al.* SCENIC: single-cell regulatory network inference and clustering. *Nat. Methods* **14**, 1083–1086 (2017).
101. Dobin, A. *et al.* STAR: ultrafast universal RNA-seq aligner. *Bioinformatics* **29**, 15–21 (2013).
102. Frankish, A. *et al.* GENCODE reference annotation for the human and mouse genomes. *Nucleic Acids Res.* **47**, D766–D773 (2019).
103. Bray, N. L., Pimentel, H., Melsted, P. & Pachter, L. Erratum: Near-optimal probabilistic RNA-seq quantification. *Nat. Biotechnol.* **34**, 888 (2016).
104. Ongen, H., Buil, A., Brown, A. A., Dermitzakis, E. T. & Delaneau, O. Fast and efficient QTL mapper for thousands of molecular phenotypes. *Bioinformatics* **32**, 1479–1485 (2016).
105. Bycroft, C. *et al.* The UK Biobank resource with deep phenotyping and genomic data. *Nature* **562**, 203–209 (2018).
106. Sinnott-Armstrong, N. *et al.* Genetics of 35 blood and urine biomarkers in the UK Biobank. *Nat. Genet.* **53**, 185–194 (2021).
107. Venkataraman, G. R. *et al.* Bayesian model comparison for rare variant association studies. doi:10.1101/257162.
108. McInnes, G. *et al.* Global Biobank Engine: enabling genotype-phenotype browsing for biobank summary statistics. *Bioinformatics* **35**, 2495–2497 (2019).
109. Zhou, Y. *et al.* Metascape provides a biologist-oriented resource for the analysis of systems-level datasets. *Nat. Commun.* **10**, 1523 (2019).
110. Gu, Z., Eils, R. & Schlesner, M. Complex heatmaps reveal patterns and correlations in multidimensional genomic data. *Bioinformatics* **32**, 2847–2849 (2016).

Fig. 1

bioRxiv preprint doi: https://doi.org/10.1101/2021.11.22.469622; this version posted November 23, 2021. The copyright holder for this preprint (which was not certified by peer review) is the author/funder, who has granted bioRxiv a license to display the preprint in perpetuity. It is made available under aCC-BY-NC-ND 4.0 International license.

Fig. 1: Study overview, highlighted results and phenotypic responses. a, We profiled bulk mRNA-seq and scRNA-seq in subcutaneous and visceral white adipose tissue (WAT), and skeletal muscle across 26 lean and 25 obese mice with 6-week diet and 3-week exercise interventions. **b,** Graphical representation and summary of highlighted results in this study. ECM, extracellular matrix. **c-f,** Body weight (**c**), running distance (**d**), caloric intake (**e**), and glucose tolerance test (GTT) result (**f**) in the four intervention groups. Statistical comparisons were performed using two way ANOVA followed by Tukey multiple comparison tests. P values are showns as *, < 0.05, ** < 0.01, *** < 0.001, **** < 0.0001. AUC, area under curve; n.s., not significant. Other abbreviations used in this figure appear in the Methods. Panels **a** and **b** were created with BioRender.com.

bioRxiv preprint doi: https://doi.org/10.1101/2021.11.22.469622; this version posted November 23, 2021. The copyright holder for this preprint (which was not certified by peer review) is the author/funder, who has granted bioRxiv a license to display the preprint in perpetuity. It is made available under aCC-BY-NC-ND 4.0 International license.

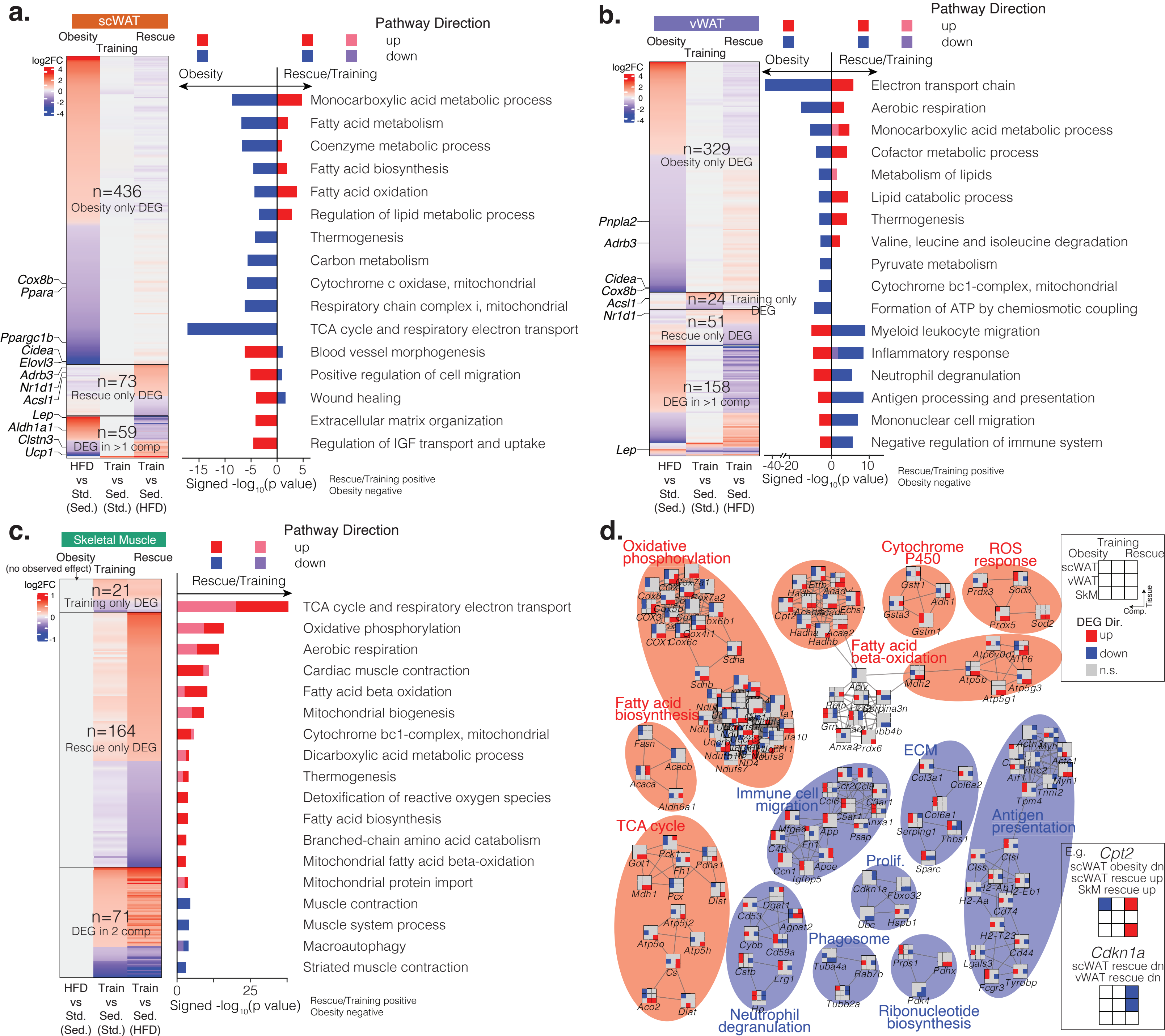

Fig. 2: Tissue-level transcriptomic responses. a-c, Genes (heatmap) and pathways (bar plot) that are significantly differentially expressed and enriched across three comparisons: "obesity" (high-fat vs. standard diet under sedentary conditions), "training" (exercise training vs. sedentary under standard diet), and "rescue" (exercise training vs. sedentary under high-fat diet) in scWAT (**a**), vWAT (**b**), and skeletal muscle (**c**). The gene heat map is coloured by $\log_2$ fold change. The pathway bar plot is coloured by pathway direction in the three comparisons (red/pink: up-regulated, blue/purple, down-regulated). X-axis of the bar plot shows $-\log_{10}$p value with rescue/training pathways being positive, and obesity being negative. DEG, differentially expressed gene. **d,** Gene networks across selected DEGs from the three tissues that encode interacting proteins, clustered by protein-protein interactions with each cluster named by the most significantly enriched pathway. The 3-by-3 grid of each node (gene) is coloured by DEG direction in the three tissues (row) and comparisons (column). The cluster is coloured by DEG direction with exercise training. ECM, extracellular matrix; Prolif, proliferation; ROS, reactive oxygen species. Other abbreviations used in this figure appear in the Methods.

bioRxiv preprint doi: https://doi.org/10.1101/2021.11.22.469622; this version posted November 23, 2021. The copyright holder for this preprint (which was not certified by peer review) is the author/funder, who has granted bioRxiv a license to display the preprint in perpetuity. It is made available under aCC-BY-NC-ND 4.0 International license.

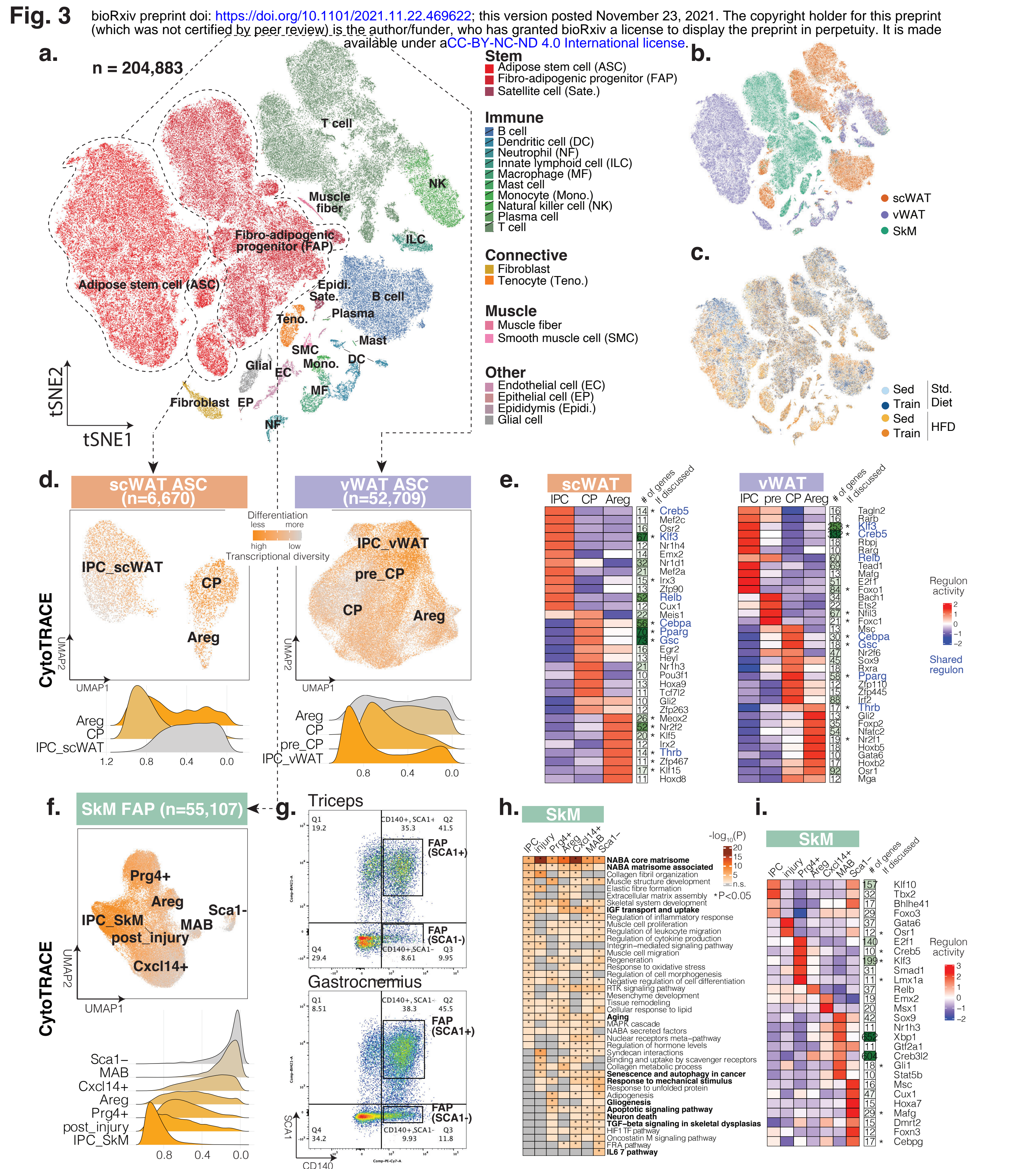

Fig. 3: single-cell atlas and mesenchymal stem cell states characterization. a, Single-cell atlas of 204,883 cells across three tissues and four intervention groups. The tSNE plot is coloured by cell type (warm colours: non-immune cell types, cold colours: immune cell types). **b-c,** Single-cell atlas coloured by tissue (**b**) and intervention group (**c**). **d,** Re-clustering of ASCs in scWAT (left) and vWAT (right), coloured by CytoTRACE -predicted differentiation stage (orange: less differentiated, gray: more differentiated). Ridge plot of individual ASC states is colored similarly. **e.** Clustering of top ASC state-specific regulons (TF with the number of regulated genes as a separate heatmap column) in scWAT (left) and vWAT (right). Shared regulons across the two depots

bioRxiv preprint doi: https://doi.org/10.1101/2021.11.22.469622; this version posted November 23, 2021. The copyright holder for this preprint (which was not certified by peer review) is the author/funder, who has granted bioRxiv a license to display the preprint in perpetuity. It is made available under aCC-BY-NC-ND 4.0 International license.

are coloured in blue, and regulons discussed in text are marked with asterisks. The heat map is scaled by column. **f,** Re-clustering of FAPs in SkM, coloured by CytoTRACE-predicted differentiation stage (orange: less differentiated, gray: more differentiated). Ridge plot of individual FAP states is colored similarly. **g.** FACS dot blot showing the sorting gates for Sca1+ and Sca1- FAPs from mouse triceps and gastrocnemius, with the percentages of the two populations labeled. **h-i.** Top pathways (**h**) and regulons (**i**) enriched in Sca1+ and Sca1- FAPs. The pathway heatmap is coloured by $-\log_{10}$p value. The regulon heatmap is coloured by activity score. A list of abbreviations used in this figure appear in the Methods.

Fig. 4

bioRxiv preprint doi: https://doi.org/10.1101/2021.11.22.469622; this version posted November 23, 2021. The copyright holder for this preprint (which was not certified by peer review) is the author/funder, who has granted bioRxiv a license to display the preprint in perpetuity. It is made available under aCC-BY-NC-ND 4.0 International license.

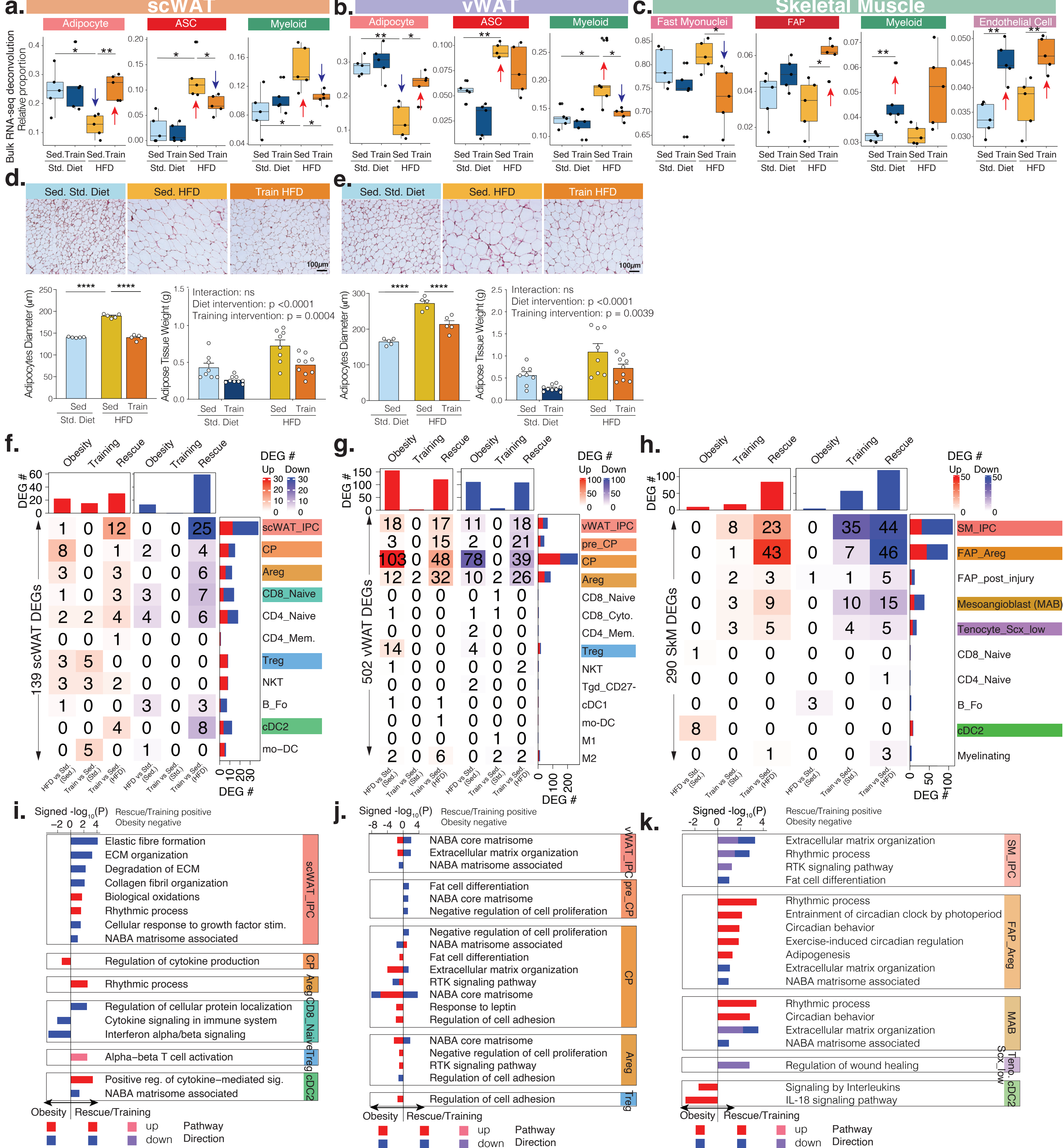

Fig. 4: Single-cell-level proportion and transcriptomic responses across the three tissues. a-c, Sample-specific proportions of cell types across the four intervention groups in scWAT (**a**), vWAT (**b**), and SkM (**c**) after bulk RNA-seq data deconvolution. * p < 0.05, ** p < 0.01. **d-e,** Histology of scWAT (**d**) and vWAT (**e**) across three intervention groups, with bar plots below showing adipocyte diameter and adipose tissue weight changes across intervention groups. ****, p <0.0001. **f-h,** The number of cell state-specific DEGs (heatmap) that are up-regulated (red) or down-regulated (blue) in our three comparisons in scWAT (**f**), vWAT (**g**) and SkM (**h**). **i-k,** Pathways (bar

bioRxiv preprint doi: https://doi.org/10.1101/2021.11.22.469622; this version posted November 23, 2021. The copyright holder for this preprint (which was not certified by peer review) is the author/funder, who has granted bioRxiv a license to display the preprint in perpetuity. It is made available under aCC-BY-NC-ND 4.0 International license.

plot) that are significantly enriched in cell state-specific DEGs across the three comparisons in scWAT (**i**), vWAT (**j**) and SkM (**k**). X-axis of the bar plot shows $-\log_{10}$ p value with rescue/training pathways being positive, and obesity being negative. The bars are coloured by pathway direction in the three comparisons (red/pink: up-regulated, blue/purple, down-regulated). DEG, differentially expressed gene. Other abbreviations used in this figure appear in the Methods.

bioRxiv preprint doi: https://doi.org/10.1101/2021.11.22.469622; this version posted November 23, 2021. The copyright holder for this preprint (which was not certified by peer review) is the author/funder, who has granted bioRxiv a license to display the preprint in perpetuity. It is made available under aCC-BY-NC-ND 4.0 International license.

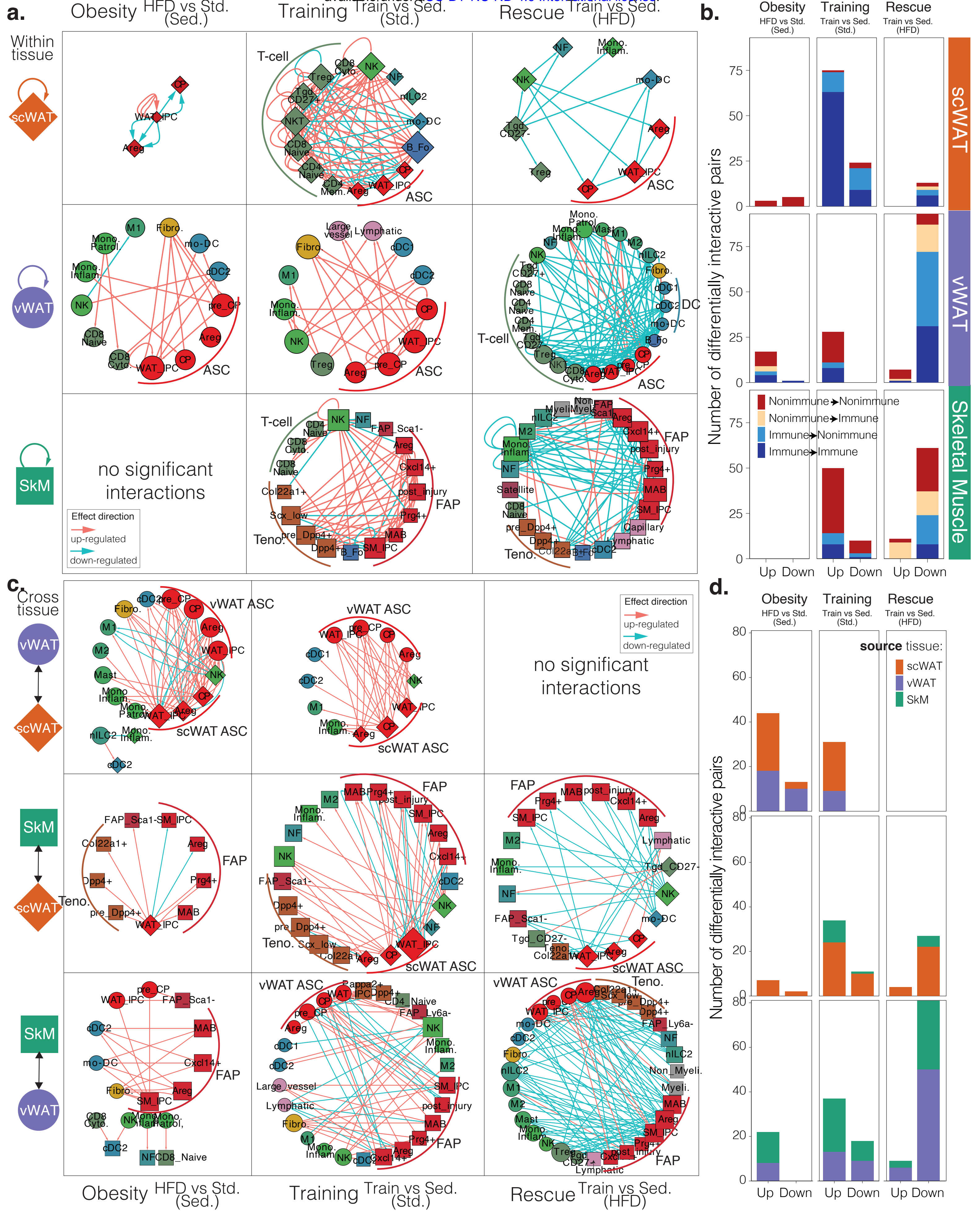

Fig. 5: Within- and cross-tissue communication at cell-state level. a, Within-tissue ligand-receptor networks

bioRxiv preprint doi: https://doi.org/10.1101/2021.11.22.469622; this version posted November 23, 2021. The copyright holder for this preprint (which was not certified by peer review) is the author/funder, who has granted bioRxiv a license to display the preprint in perpetuity. It is made available under aCC-BY-NC-ND 4.0 International license.

across the three tissues and three comparisons. Cell states (nodes) are shaped by tissue (diamond: scWAT, circle: vWAT, square: skeletal muscle) and sized by outdegree. Ligand-receptor interactions (edges) are directed, from ligand to receptor, and coloured by effect direction (pink: up-regulated, blue: down-regulated). **b,** The number of differentially interactive ligand-receptor pairs that are up- and down-regulated across the three tissues and three comparisons at cell-state level. Each bar is coloured by if the ligand or the receptor is from immune or non-immune cell state. **c,** Cross-tissue ligand-receptor networks across three pairs of tissues and three comparisons. The nodes and edges are formatted the same as in panel **a**. **d,** The number of differentially interactive ligand-receptor pairs that are up- and down-regulated across three pairs of tissues and three comparisons at cell-state level. Each bar is coloured by tissue source of the ligand. A list of abbreviations used in this figure appear in the Methods.

bioRxiv preprint doi: https://doi.org/10.1101/2021.11.22.469622; this version posted November 23, 2021. The copyright holder for this preprint (which was not certified by peer review) is the author/funder, who has granted bioRxiv a license to display the preprint in perpetuity. It is made available under aCC-BY-NC-ND 4.0 International license.

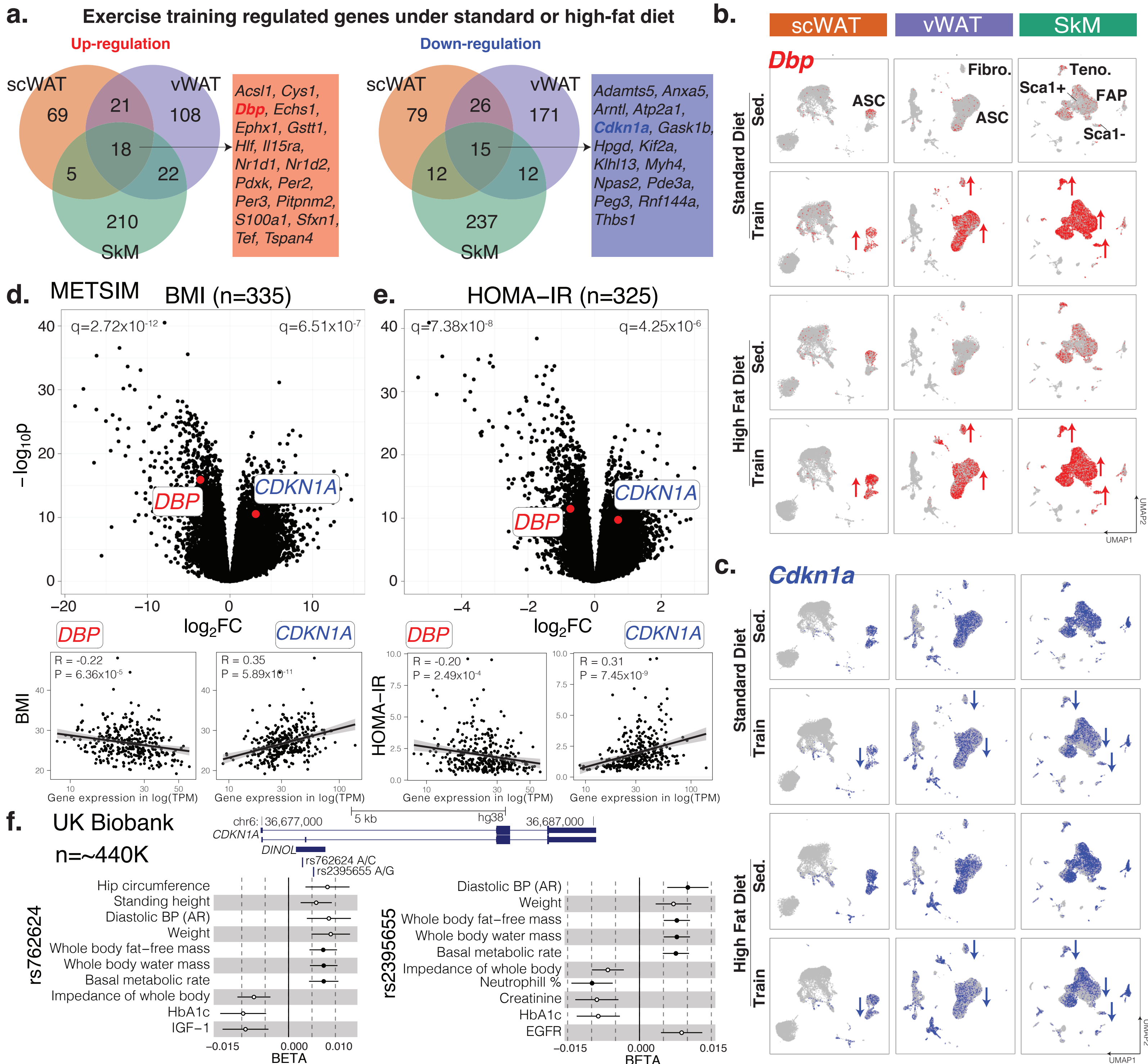

Fig. 6: Two exercise-regulated genes (DBP and CDKN1A) in human. a, Overlap of up- and down-regulated genes by exercise training under standard or high-fat diet across the three tissues. Genes listed are regulated by exercise training in all three tissues. **b-c,** *Dbp* (**b**) and *CDKN1A* (**c**) expression across the three tissues and four intervention groups. Cell types with the most changes are labeled in the top panel. **d-e,** *DBP* and *CDKN1A* association with BMI (**d**) and HOMA-IR (**e**) in scWAT of METSIM subjects. Genes (dots in upper plots) and subjects (dots in lower plots) are plotted. HOMA-IR, homeostatic model assessment for insulin resistance. **f,** Association of two SNPs (rs762624 and rs2395655) in *CDKN1A* with anthropometric and metabolic traits in UK Biobank. The meta-analyzed PheWAS summary statistics (BETAs with standard errors, p < 1e-3) are shown. The filled circles are significant after correction (p < 1e-5). SNP, single nucleotide polymorphism; PheWAS, phenome-wide association study; BP: blood pressure. AR: automated reading. Other abbreviations used in this figure appear in the Methods.

bioRxiv preprint doi: https://doi.org/10.1101/2021.11.22.469622; this version posted November 23, 2021. The copyright holder for this preprint (which was not certified by peer review) is the author/funder, who has granted bioRxiv a license to display the preprint in perpetuity. It is made available under aCC-BY-NC-ND 4.0 International license.

Extended Data Fig. 1

Extended Data Fig. 1: Single-cell analysis pipeline, sample clustering, and cross-comparison tissue-level transcriptomic change correlation. a, Graphical representation of single-cell analysis pipeline and the four QC steps taken. **b,** Unbiased clustering of tissue- and single-cell-level samples with variables that may introduce batch effects colored on the top. The variables include tissue type, exercise group, diet group, and tissue collection time and day. **c,** Global transcriptomic change correlation across “obesity”, “training”, and “rescue” comparisons in scWAT (left), vWAT (middle), and skeletal muscle. The P and r values were obtained from correlation tests. FC, fold change. Other abbreviations used in this figure appear in the Methods.

bioRxiv preprint doi: https://doi.org/10.1101/2021.11.22.469622; this version posted November 23, 2021. The copyright holder for this preprint (which was not certified by peer review) is the author/funder, who has granted bioRxiv a license to display the preprint in perpetuity. It is made available under aCC-BY-NC-ND 4.0 International license.

Extended Data Fig. 2

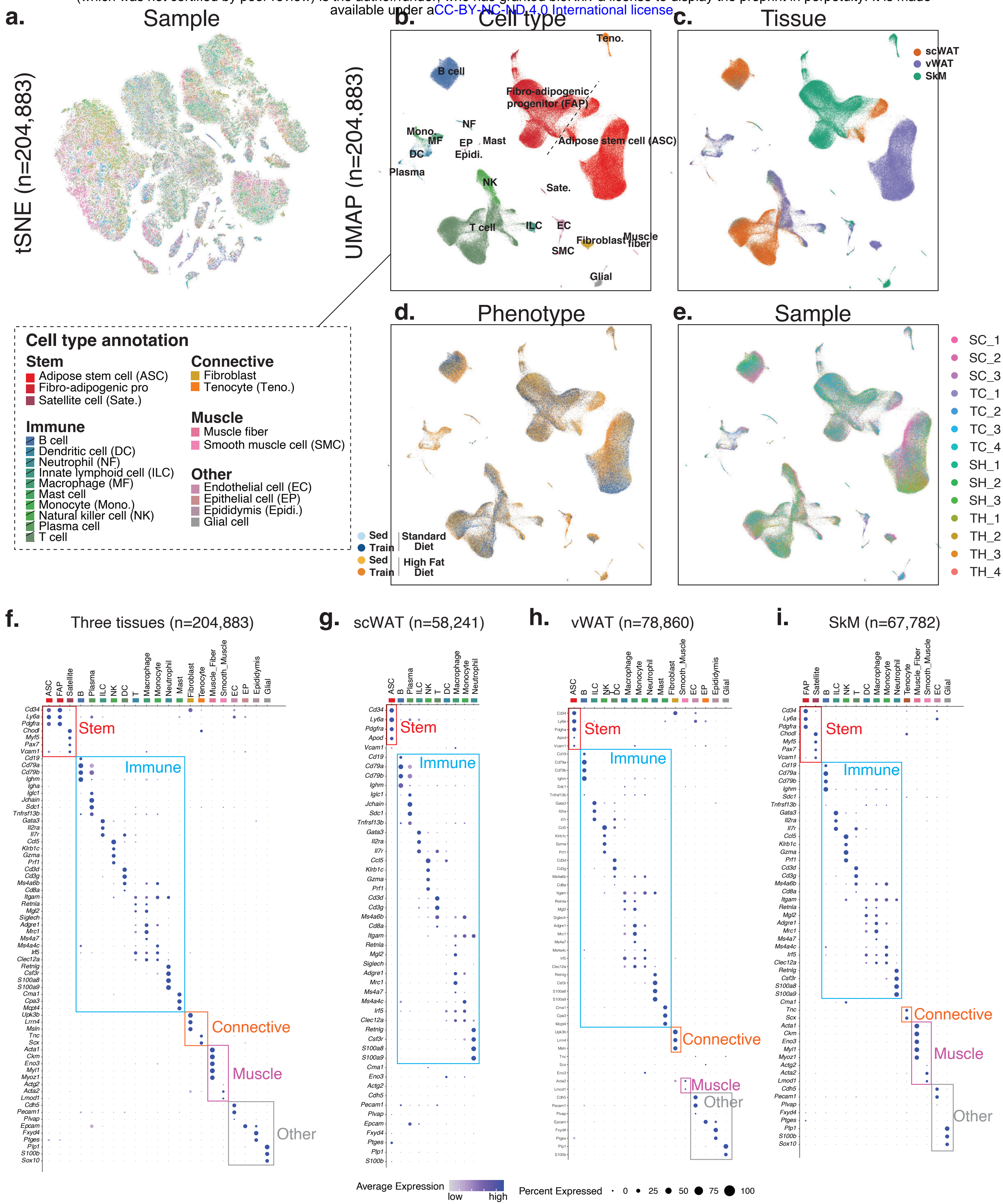

bioRxiv preprint doi: https://doi.org/10.1101/2021.11.22.469622; this version posted November 23, 2021. The copyright holder for this preprint (which was not certified by peer review) is the author/funder, who has granted bioRxiv a license to display the preprint in perpetuity. It is made available under aCC-BY-NC-ND 4.0 International license.

Extended Data Fig. 2: Different representations of single-cell atlas and cell-type-specific marker gene expression. a-e, Single-cell atlas of 204,883 cells across three tissues and four intervention groups. The tSNE (**a**) or UMAP (**c-e**) plot is coloured by sample (**a,e**), cell type (**b**), tissue (**c**), and intervention group (**d**). SC, sedentary chow (standard) diet; TC, training chow (standard) diet; SH, sedentary high-fat diet; TH, training high-fat diet. **f-i,** Cell-type-specific marker gene expression across the three tissues and in each individual tissue. A list of abbreviations used in this figure appear in the Methods.

bioRxiv preprint doi: https://doi.org/10.1101/2021.11.22.469622; this version posted November 23, 2021. The copyright holder for this preprint (which was not certified by peer review) is the author/funder, who has granted bioRxiv a license to display the preprint in perpetuity. It is made available under aCC-BY-NC-ND 4.0 International license.

Extended Data Fig. 3

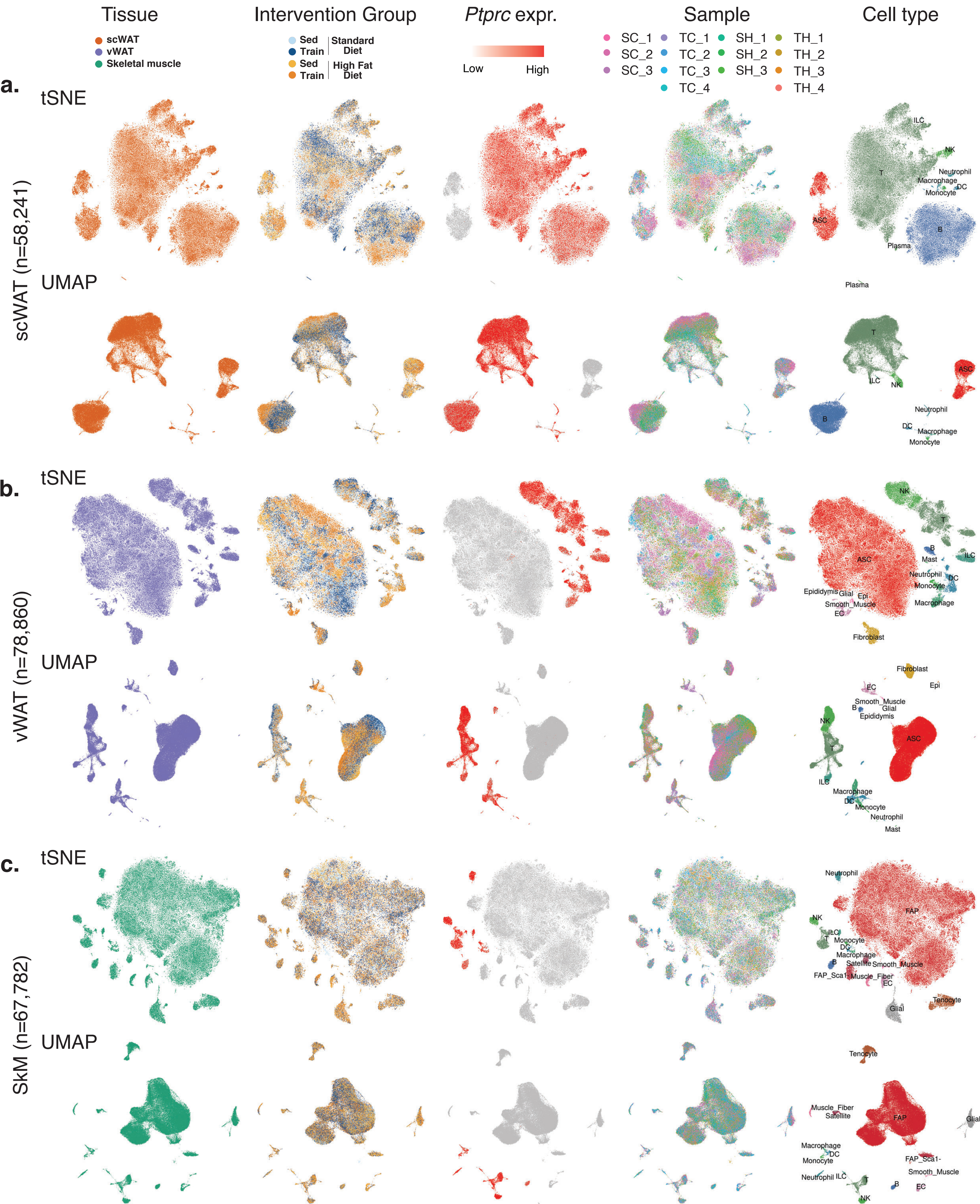

bioRxiv preprint doi: https://doi.org/10.1101/2021.11.22.469622; this version posted November 23, 2021. The copyright holder for this preprint (which was not certified by peer review) is the author/funder, who has granted bioRxiv a license to display the preprint in perpetuity. It is made available under aCC-BY-NC-ND 4.0 International license.

Extended Data Fig. 3: Different representations of single-cell maps for each tissue. a-c, Single-cell maps of scWAT (**a**), vWAT (**b**) and SkM (**c**) across four intervention groups. The tSNE and UMAP plots in each panel are coloured by tissue type, intervention group, *Ptprc* expression, sample, and cell type. A list of abbreviations used in this figure appear in the Methods.

bioRxiv preprint doi: https://doi.org/10.1101/2021.11.22.469622; this version posted November 23, 2021. The copyright holder for this preprint (which was not certified by peer review) is the author/funder, who has granted bioRxiv a license to display the preprint in perpetuity. It is made available under aCC-BY-NC-ND 4.0 International license.

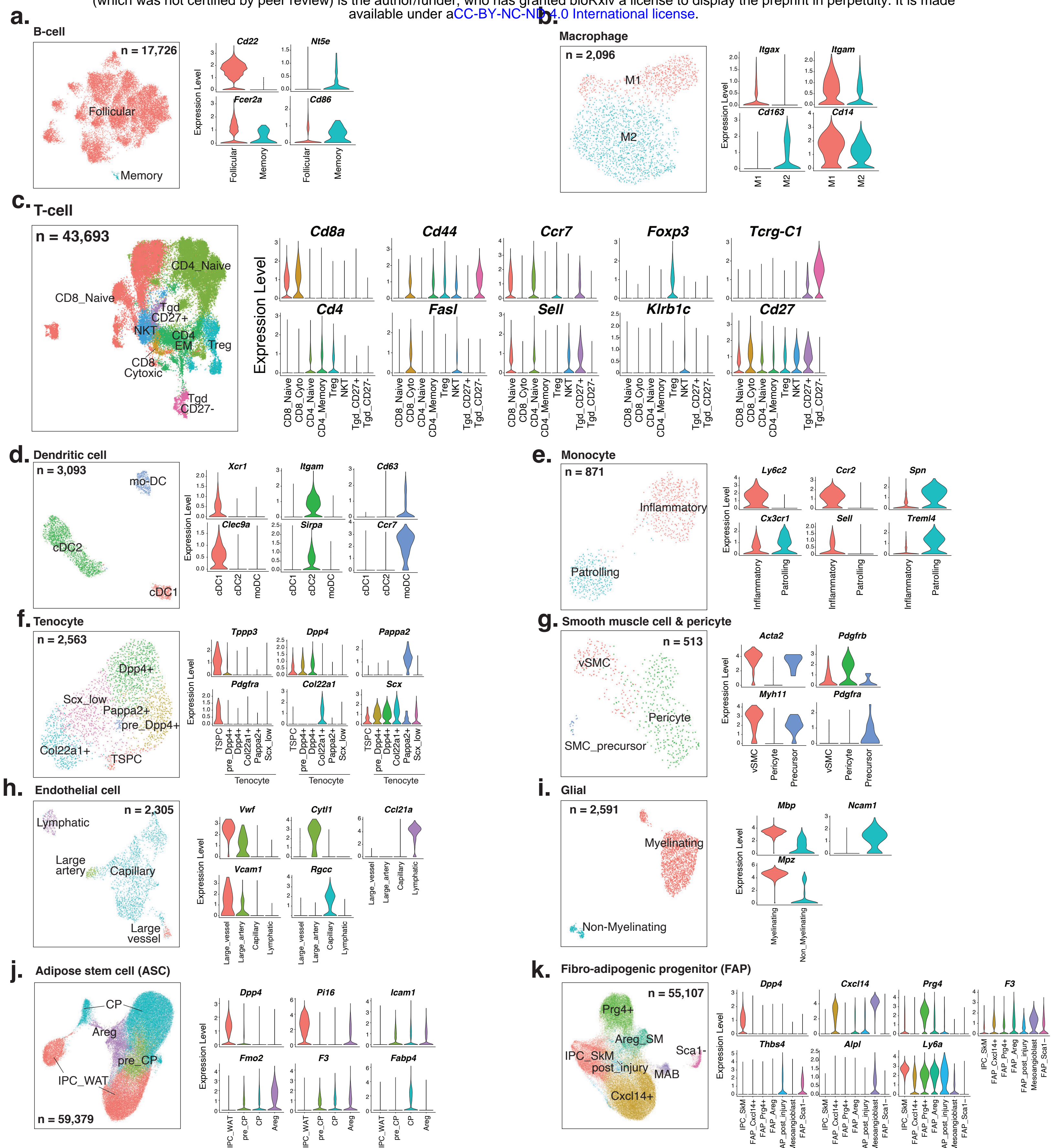

Extended Data Fig. 4: Sub-clustering of cell types across tissues. a-k, Cell subtypes or states of B-cell (**a**), macrophage (**b**), T-cell (**c**), dendritic cell (**d**), monocyte (**e**), tenocyte (**f**), smooth muscle cell (**g**), endothelial cell (**h**), glial cell (**i**), adipose stem cell (**j**), and fibro-adipogenic progenitor (**k**).

bioRxiv preprint doi: https://doi.org/10.1101/2021.11.22.469622; this version posted November 23, 2021. The copyright holder for this preprint (which was not certified by peer review) is the author/funder, who has granted bioRxiv a license to display the preprint in perpetuity. It is made available under aCC-BY-NC-ND 4.0 International license.

Extended Data Fig. 5

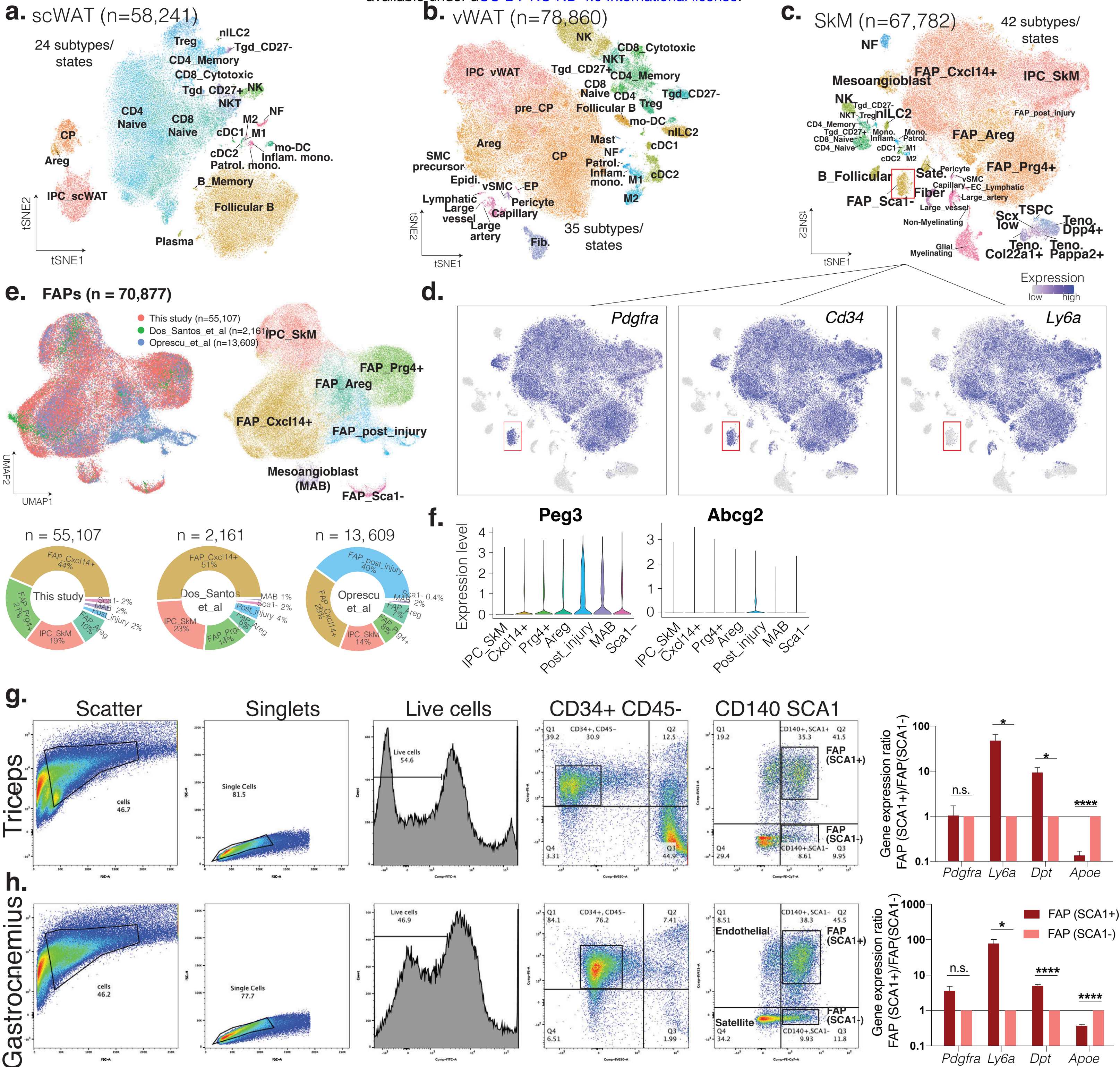

Extended Data Fig. 5: Single-cell subtype/state annotation in the three tissues and fibro-adipogenic progenitor characterization in skeletal muscle. a-c, Single-cell maps of scWAT (**a**), vWAT (**b**) and SkM (**c**) with cells coloured by cell subtype/state. **d,** Single-cell map of SkM with cells coloured by Pdgfra, Ly6a and Cd34 expression. **e,** Re-clustering of FAPs from this study with FAPs from two publicly available datasets. The cells are coloured by study (left) and cell state (right). Proportions of the seven distinct FAP states in each study are shown below. **f,** *Peg3* and *Abcg2* expression across FAP states in our single-cell data. **g-h,** FACS gating strategy and relative proportions of Sca1+ and Sca1- FAP populations in triceps (**g**) and gastrocnemius muscle (**h**). Statistical comparisons were performed using unparied t-test. P values are showns as *, < 0.05, ** < 0.01, *** < 0.001, **** < 0.0001. n.s., not significant. A list of abbreviations used in this figure appear in the Methods.

bioRxiv preprint doi: https://doi.org/10.1101/2021.11.22.469622; this version posted November 23, 2021. The copyright holder for this preprint (which was not certified by peer review) is the author/funder, who has granted bioRxiv a license to display the preprint in perpetuity. It is made available under aCC-BY-NC-ND 4.0 International license.

Extended Data Fig. 6

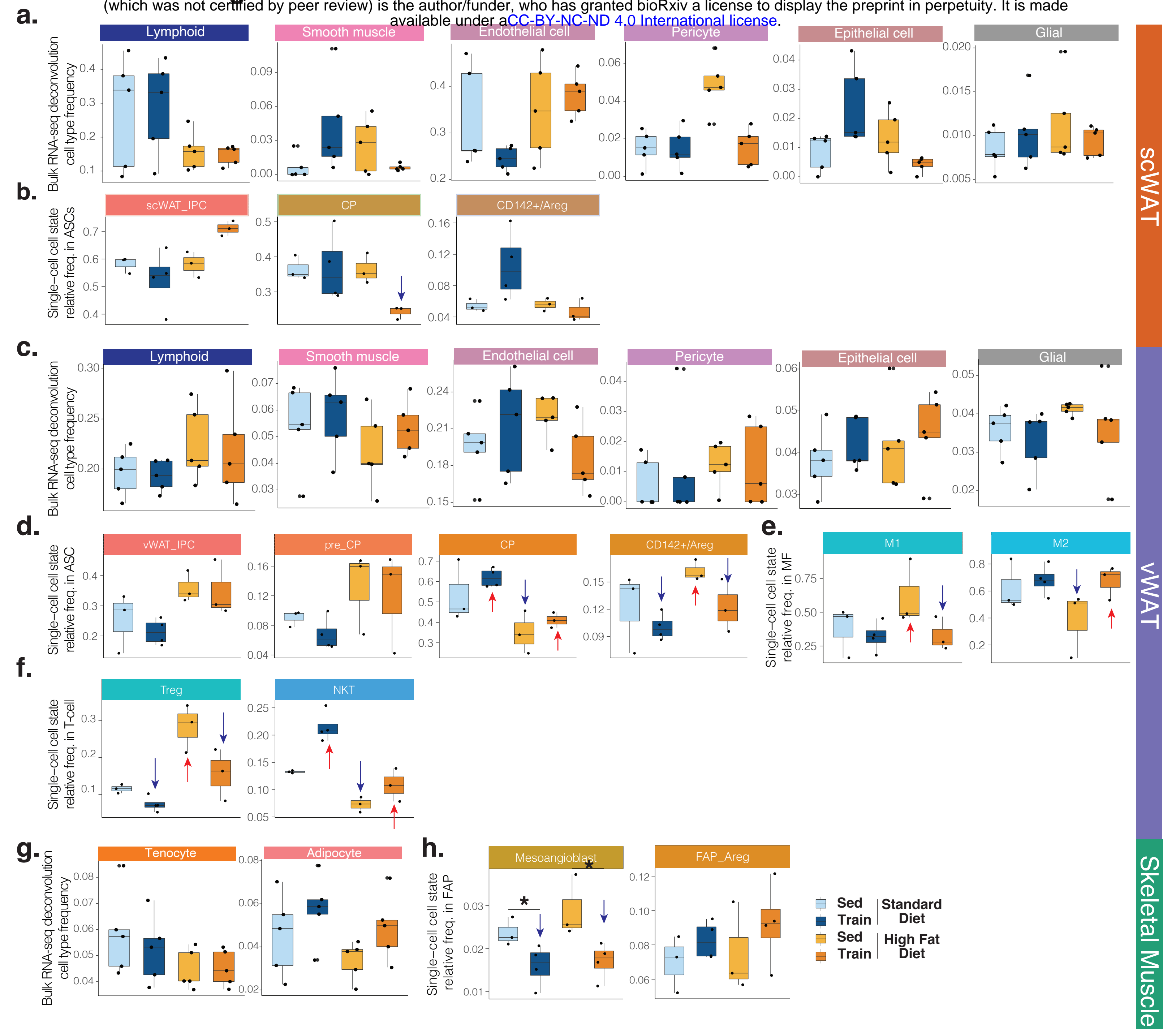

Extended Data Fig. 6: Cell type/state proportion changes with high-fat diet and exercise training. a-b, scWAT results. **a,** Sample-specific proportions of 6 cell types/groups after bulk RNA-seq data deconvolution across the four intervention groups. **b,** Sample-specific proportions of 3 states within ASCs based on our single-cell data in the four intervention groups. **c-f,** vWAT results. **c,** Sample-specific proportions of 6 cell types/groups after bulk RNA-seq data deconvolution across the four intervention groups. **d-f,** Sample-specific proportions of 4 states within ASCs (**d**), 2 states of macrophages (**e**), and 2 states of T-cells (**f**) based on our single-cell data in the four intervention groups. **g-h,** Skeletal muscle results. **g,** Sample-specific proportions of 2 cell types after bulk RNA-seq data deconvolution across the four intervention groups. **h,** Sample-specific proportions of mesoangioblast and Areg_FAP within FAPs. A list of abbreviations used in this figure appear in the Methods.

bioRxiv preprint doi: https://doi.org/10.1101/2021.11.22.469622; this version posted November 23, 2021. The copyright holder for this preprint (which was not certified by peer review) is the author/funder, who has granted bioRxiv a license to display the preprint in perpetuity. It is made available under aCC-BY-NC-ND 4.0 International license.

Extended Data Fig. 7

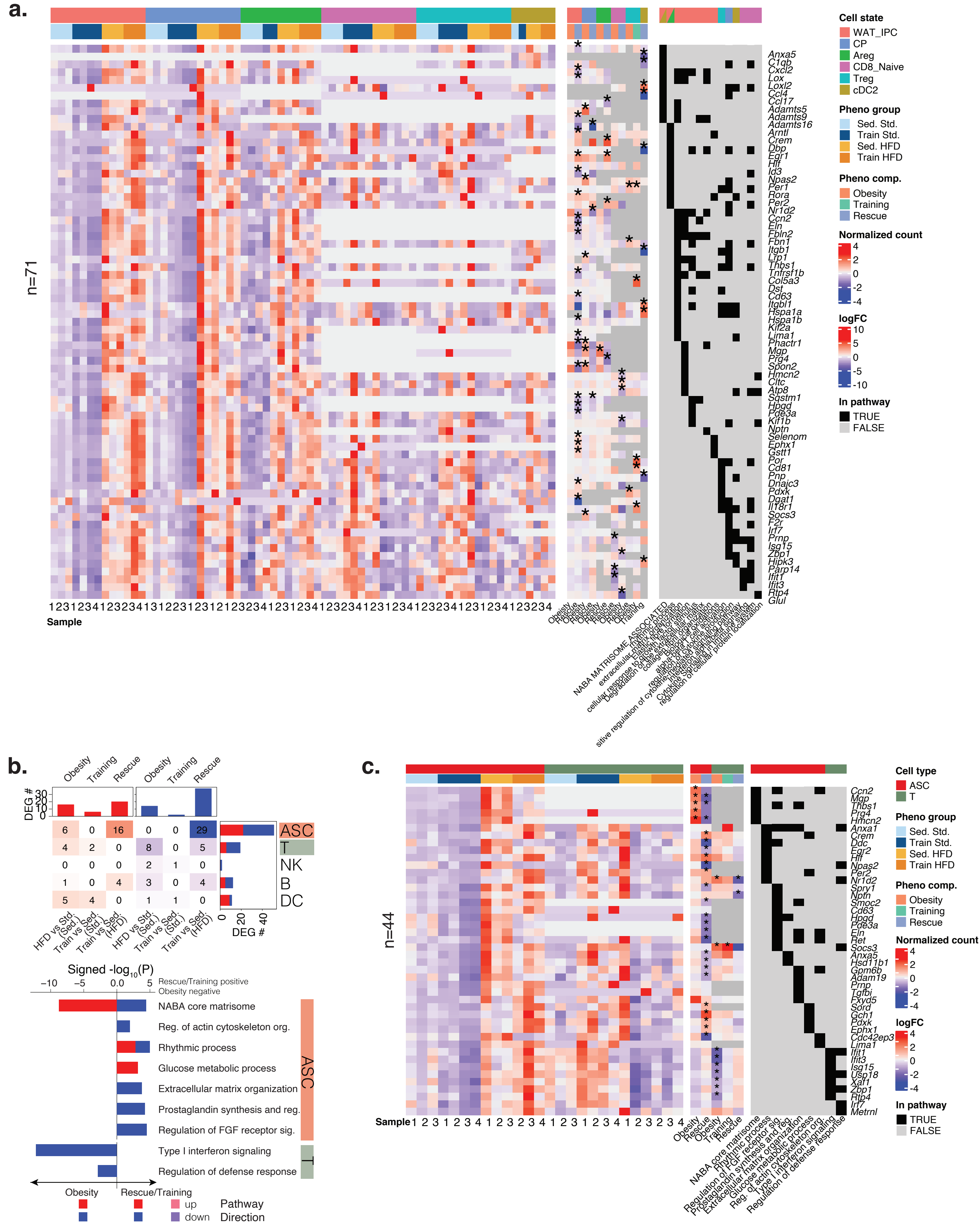

bioRxiv preprint doi: https://doi.org/10.1101/2021.11.22.469622; this version posted November 23, 2021. The copyright holder for this preprint (which was not certified by peer review) is the author/funder, who has granted bioRxiv a license to display the preprint in perpetuity. It is made available under aCC-BY-NC-ND 4.0 International license.

Extended Data Fig. 7: Cell-state and cell-type-specific transcriptomic changes with high-fat diet and exercise training in scWAT. a, Cell-state-specific DEGs and their membership in the significantly enriched pathways: sample-specific mean expression for each gene (left heatmap), their fold changes in the three comparisons whenever available (middle heatmap, * if significant), and their membership in the pathways (right heatmap). **b.** The number of cell-type-specific DEGs (heatmap) that are up-regulated (red) or down-regulated (blue) in our three comparisons. Pathways (bar plot) that are significantly enriched in cell-type-specific DEGs. **c,** Cell-type-specific DEGs and their membership in the significantly enriched pathways. The format is the same as in panel **a**. A list of abbreviations used in this figure appear in the Methods.

bioRxiv preprint doi: https://doi.org/10.1101/2021.11.22.469622; this version posted November 23, 2021. The copyright holder for this preprint (which was not certified by peer review) is the author/funder, who has granted bioRxiv a license to display the preprint in perpetuity. It is made available under aCC-BY-NC-ND 4.0 International license.

Extended Data Fig. 8

a.

n=142

Sample

1 2 3 1 2 3 4 1 2 3 1 3 4 1 2 3 1 2 3 4 1 2 3 1 3 4 1 2 3 1 2 3 4 1 2 3 1 3 4 1 2 3 1 2 3 4 1 2 3 1 3 4 1 2 3 1 2 3 4 1 2 3 1 3 4

Obesity, Rescue, Obesity, Rescue, Obesity, Rescue, Obesity, Training, Rescue, Obesity

core matrisome, matrisome associated, Reg. of cell adhesion, ECM organization, Neg. reg. of cell prolif., fat cell diff., response to leptin, RTK signaling

Cell state: WAT_IPC, pre_CP, CP, Areg, Treg

Pheno group: SC, TC, SH, TH

Pheno comp.: Obesity, Training, Rescue

norm. count: 4, 2, 0, -2, -4

logFC: 6, 4, 2, 0, -2, -4, -6

In pathway: True, False

b.

DEG #	Obesity	Training	Rescue	Obesity	Training	Rescue	
ASC	56	1	37	58	0	30	ASC
Fib.	2	1	3	0	1	2	Fib.
T	51	0	0	1	0	0	T
EC	0	1	0	0	0	0	EC
	HFD vs Std. (Sed.)	Train vs Sed. (Std.)	Train vs Sed. (HFD)	HFD vs Std. (Sed.)	Train vs Sed. (Std.)	Train vs Sed. (HFD)	

DEG # axis: 0, 50, 100; 0, 50, 100, 150

Signed -log$_{10}$(P)

−8 −6 −4 −2 0 2

Rescue/Training positive
Obesity negative

ASC:
Rhythmic process
Monocarboxylic acid transport
Cellular response to TGFb stimulus
Response to growth factor
ROS metabolic process
NABA matrisome associated
G alpha (q) signalling events
NABA core matrisome
Metabolism of lipids
PI3K−Akt signaling pathway
Positive regulation of MAPK cascade
Positive regulation of locomotion

Fib.:
Rhythmic process

T:
PI3K−Akt signaling pathway
NABA matrisome associated
G alpha (q) signalling events

Obesity ← → Rescue/Training

Pathway: up, down
Direction

c.

n=119

Sample

1 2 3 1 2 3 4 1 2 3 1 3 4 1 2 3 1 2 3 4 1 2 3 1 3 4 1 2 3 1 2 3 4 1 2 3 1 3 4

Obesity, Training, Rescue, Obesity, Training, Rescue, Obesity

NABA core matrisome, Pos. reg. of locomotion, PI3K−Akt signaling, Pos. reg. of MAPK cascade, NABA matrisome associated, Response to growth factor, Response to TGFb stimulus, ROS metabolic process, Rhythmic process, G alpha (q) signalling, monocarboxylic acid transport, Metabolism of lipids

Cell type: ASC, Fibroblast, T

Pheno group: Sed. Std., Train Std., Sed. HFD, Train HFD

Pheno comp.: Obesity, Training, Rescue

Norm. count: 4, 2, 0, -2, -4

logFC: 10, 5, 0, -5, -10

In pathway: TRUE, FALSE

bioRxiv preprint doi: https://doi.org/10.1101/2021.11.22.469622; this version posted November 23, 2021. The copyright holder for this preprint (which was not certified by peer review) is the author/funder, who has granted bioRxiv a license to display the preprint in perpetuity. It is made available under aCC-BY-NC-ND 4.0 International license.

Extended Data Fig. 8: Cell-state and cell-type-specific transcriptomic changes with high-fat diet and exercise training in vWAT. a, Cell-state-specific DEGs and their membership in the significantly enriched pathways: sample-specific mean expression for each gene (left heatmap), their fold changes in the three comparisons whenever available (middle heatmap, * if significant), and their membership in the pathways (right heatmap). **b.** The number of cell-type-specific DEGs (heatmap) that are up-regulated (red) or down-regulated (blue) in our three comparisons. Pathways (bar plot) that are significantly enriched in cell-type-specific DEGs. **c,** Cell-type-specific DEGs and their membership in the significantly enriched pathways. The format is the same as in panel **a**. A list of abbreviations used in this figure appear in the Methods.

bioRxiv preprint doi: https://doi.org/10.1101/2021.11.22.469622; this version posted November 23, 2021. The copyright holder for this preprint (which was not certified by peer review) is the author/funder, who has granted bioRxiv a license to display the preprint in perpetuity. It is made available under aCC-BY-NC-ND 4.0 International license.

Extended Data Fig. 9

a.

b.

	HFD vs Std. (Sed.)	Train vs Sed. (Std.)	Train vs Sed. (HFD)	HFD vs Std. (Sed.)	Train vs Sed. (Std.)	Train vs Sed. (HFD)
FAP	0	2	47	0	5	80
FAP_Sca1−	2	0	8	0	0	1
Satellite	3	0	0	0	0	0
Tenocyte	0	3	12	3	11	9
T	6	0	0	0	0	0
NK	0	0	0	2	0	0
B	0	0	0	3	0	0
DC	20	0	0	1	0	0
Glial	0	0	0	0	0	1

c.

bioRxiv preprint doi: https://doi.org/10.1101/2021.11.22.469622; this version posted November 23, 2021. The copyright holder for this preprint (which was not certified by peer review) is the author/funder, who has granted bioRxiv a license to display the preprint in perpetuity. It is made available under aCC-BY-NC-ND 4.0 International license.

Extended Data Fig. 9: Cell-state and cell-type-specific transcriptomic changes with high-fat diet and exercise training in SkM. a, Cell-state-specific DEGs and their membership in the significantly enriched pathways: sample-specific mean expression for each gene (left heatmap), their fold changes in the three comparisons whenever available (middle heatmap, * if significant), and their membership in the pathways (right heatmap). **b.** The number of cell-type-specific DEGs (heatmap) that are up-regulated (red) or down-regulated (blue) in our three comparisons. Pathways (bar plot) that are significantly enriched in cell-type-specific DEGs. **c,** Cell-type-specific DEGs and their membership in the significantly enriched pathways. The format is the same as in panel **a**. A list of abbreviations used in this figure appear in the Methods.

bioRxiv preprint doi: https://doi.org/10.1101/2021.11.22.469622; this version posted November 23, 2021. The copyright holder for this preprint (which was not certified by peer review) is the author/funder, who has granted bioRxiv a license to display the preprint in perpetuity. It is made available under aCC-BY-NC-ND 4.0 International license.

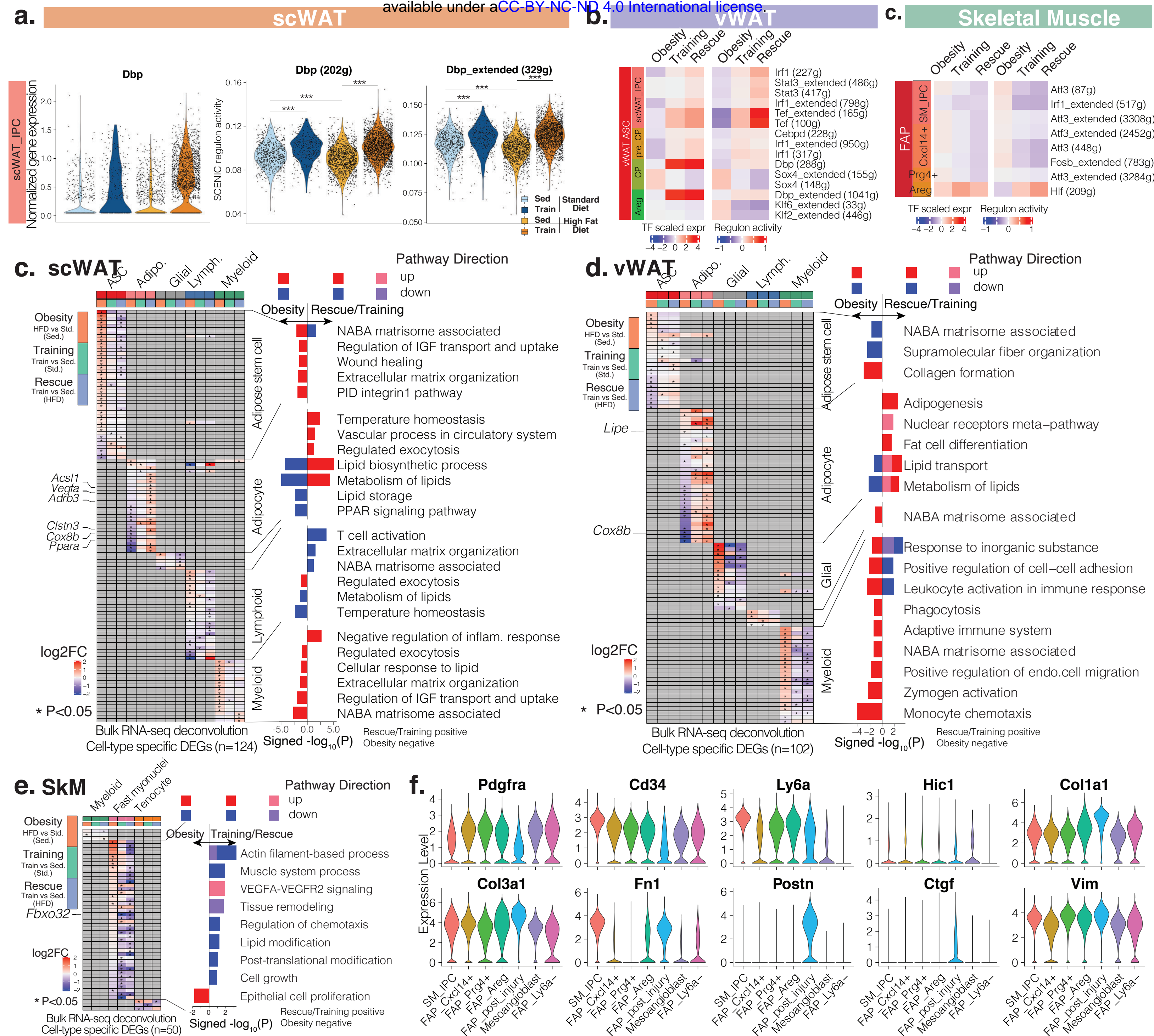

Extended Data Fig. 10: Regulon activity and deconvolved transcriptomic changes. a. Intervention group -specific Dbp expression and regulon activity in IPCs of scWAT. The number of genes regulated by Dbp is in parentheses. ***, p <0.001. **b-c.** Cell state-specific TF expression (left heatmap) and regulon activity (right heatmap) changes with the three comparisons in vWAT (**b**) and SkM (**c**). Only TF and regulon with p value less than 0.05 are shown. The number of genes regulated by each TF is in parentheses. **c-e,** After deconvolution cell group-specific DEGs (heatmap) and pathways (bar plot) that are up-regulated or down-regulated in our three comparisons in scWAT (**c**), vWAT (**d**) and SkM (**e**). X-axis of the bar plot shows -log$_{10}$p value with rescue/training pathways being positive, and obesity being negative. The bars are coloured by pathway direction in the three comparisons (red/pink: up-regulated, blue/purple, down-regulated). **f.** Marker gene expression in Sca1+ and Sca1- FAPs. The markers are from a cell type similar to Sca1- FAP that is identified in heart. A list of abbreviations used in this figure appear in the Methods.

bioRxiv preprint doi: https://doi.org/10.1101/2021.11.22.469622; this version posted November 23, 2021. The copyright holder for this preprint (which was not certified by peer review) is the author/funder, who has granted bioRxiv a license to display the preprint in perpetuity. It is made available under aCC-BY-NC-ND 4.0 International license.

Extended Data Fig. 14

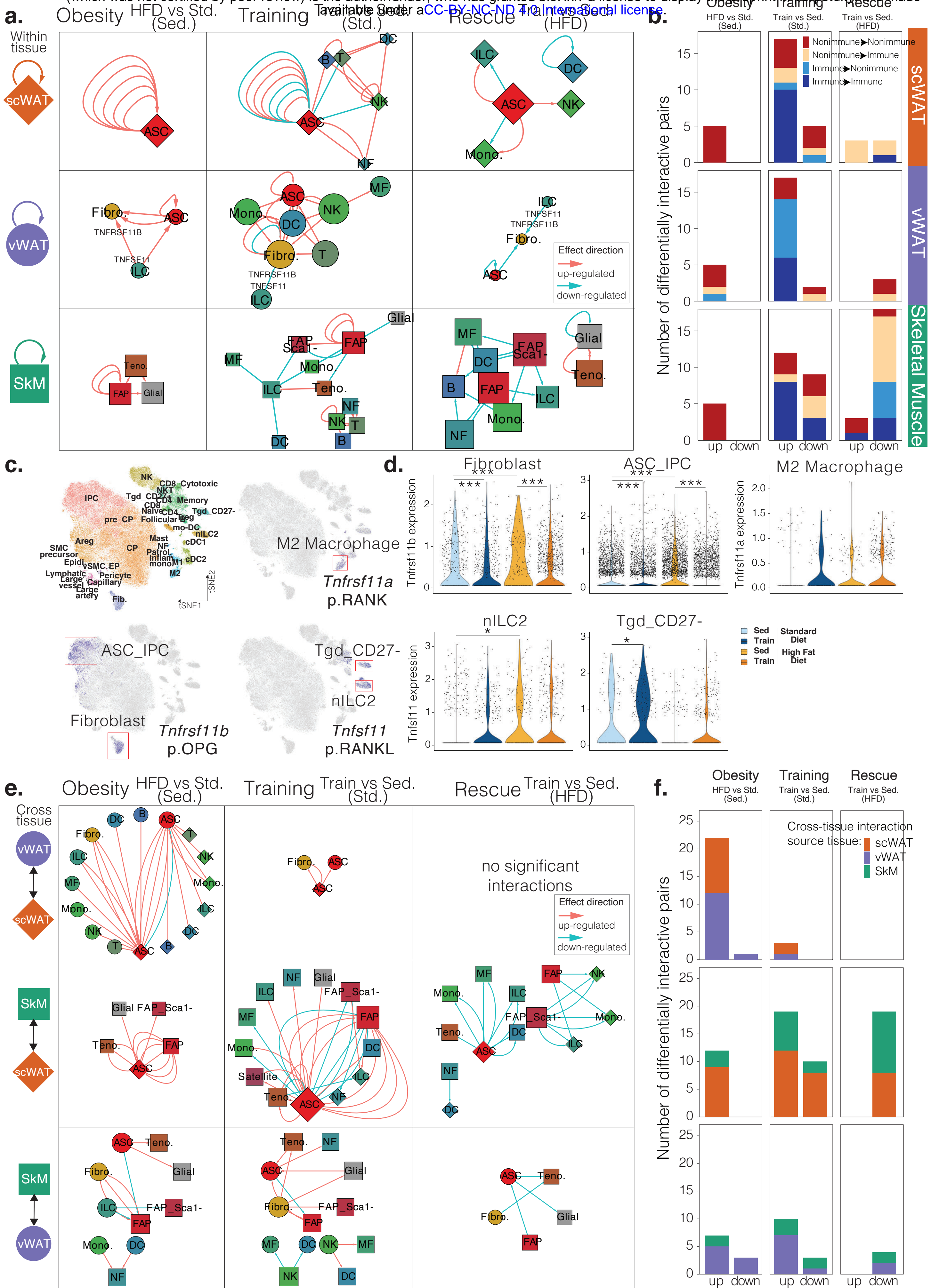

bioRxiv preprint doi: https://doi.org/10.1101/2021.11.22.469622; this version posted November 23, 2021. The copyright holder for this preprint (which was not certified by peer review) is the author/funder, who has granted bioRxiv a license to display the preprint in perpetuity. It is made available under aCC-BY-NC-ND 4.0 International license.

Extended Data Fig. 11: Within- and cross-tissue communication. a, Within-tissue ligand-receptor networks across the three tissues and three comparisons. Cell types (nodes) are shaped by tissue (diamond: scWAT, circle: vWAT, square: skeletal muscle) and sized by outdegree. Ligand-receptor interactions (edges) are directed from ligand to receptor, and coloured by effect direction (pink: up-regulated, blue: down-regulated). **b,** The number of differentially interactive ligand-receptor pairs that are up- and down-regulated across the three tissues and three comparisons at cell-type level. Each bar is coloured by if the ligand or the receptor is from immune or non-immune cell type. **c,** vWAT single-cell map with cells coloured by cell subtype/state, or expression of *Tnfsf11*, *Tnfrsf11a*, or *Tnfrsf11b*. **d,** Cell subtype/state-specific *Tnfsf11*, *Tnfrsf11a*, and *Tnfrsf11b* expression in the four intervention groups. * $p < 0.05$, *** $p < 0.001$. **e,** Cross-tissue ligand-receptor networks across three pairs of tissues and three comparisons. The nodes and edges are formatted the same as in panel **a**. **f,** The number of differentially interactive ligand-receptor pairs that are up- and down-regulated across three pairs of tissues and three comparisons. Each bar is coloured by tissue source of the ligand. A list of abbreviations used in this figure appear in the Methods.

bioRxiv preprint doi: https://doi.org/10.1101/2021.11.22.469622; this version posted November 23, 2021. The copyright holder for this preprint (which was not certified by peer review) is the author/funder, who has granted bioRxiv a license to display the preprint in perpetuity. It is made available under aCC-BY-NC-ND 4.0 International license.

Extended Data Fig. 12

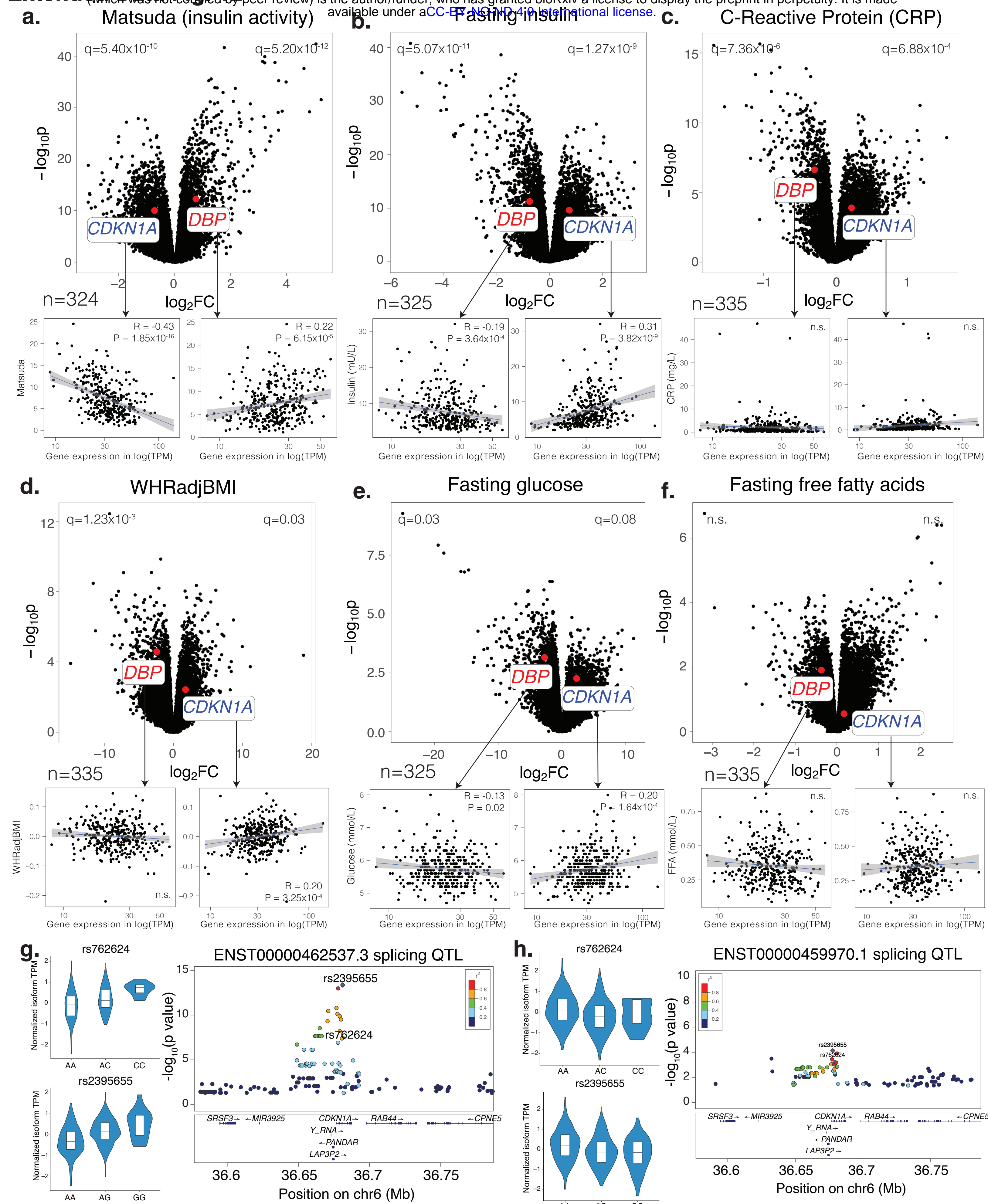

Extended Data Fig. 12: Association of DBP and CDKN1A with metabolic traits, and CDKN1A splicing QTLs

bioRxiv preprint doi: https://doi.org/10.1101/2021.11.22.469622; this version posted November 23, 2021. The copyright holder for this preprint (which was not certified by peer review) is the author/funder, who has granted bioRxiv a license to display the preprint in perpetuity. It is made available under aCC-BY-NC-ND 4.0 International license.

in human. a-f, *DBP* and *CDKN1A* association with matsuda, an indicator of insulin activity (**a**); fasting insulin (**b**); CRP, an indicator of inflammation (**c**); waist hip ratio adjusted for BMI (**d**); fasting glucose (**e**); fasting free fatty acids (**f**) in scWAT of METSIM subjects. Genes (dots in upper plots) and subjects (dots in lower plots) are plotted **g-h,** Association of two SNPs (rs762624 and rs2395655) in *CDKN1A* with one transcript isoform (**g**) but not another (**h**) in METSIM. Violin plots show transcript levels associated with genotypes. Locus plots show splicing QTL p values and r-square values with nearby variants.TPM, reads mapped to transcript per million mapped reads.

bioRxiv preprint doi: https://doi.org/10.1101/2021.11.22.469622; this version posted November 23, 2021. The copyright holder for this preprint (which was not certified by peer review) is the author/funder, who has granted bioRxiv a license to display the preprint in perpetuity. It is made available under aCC-BY-NC-ND 4.0 International license.

Supplementary Fig. 1

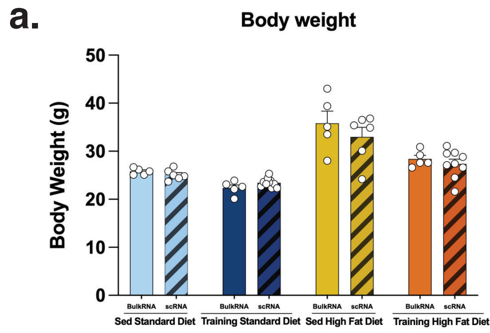

Interaction: ns
BulkRNA vs. scRNA: ns
Diet and training interventions: $p < 0.0001$

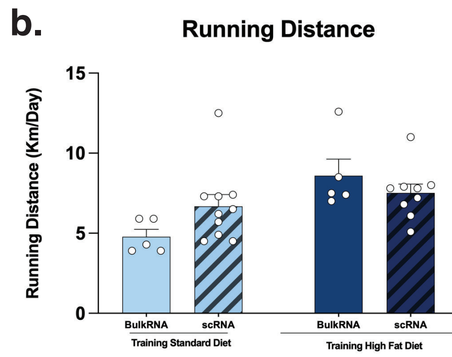

Interaction: ns
BulkRNA vs. scRNA: ns
Diet interventions: p: 0.054

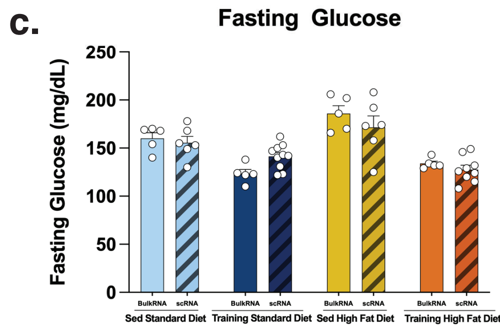

Interaction: ns
BulkRNA vs. scRNA: ns
Diet and training interventions: $p < 0.0001$

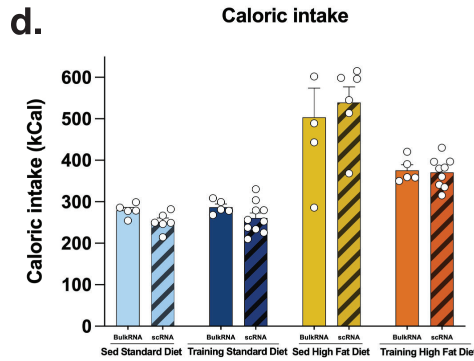

Interaction: ns
BulkRNA vs scRNA: ns
Diet and training interventions: $p < 0.0001$

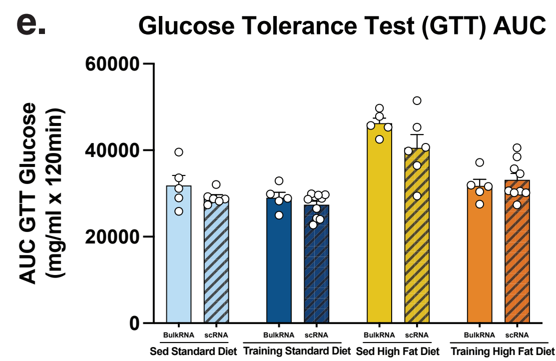

Interaction: ns
BulkRNA vs scRNA: ns
Diet and training interventions: < 0.0001

Supplementary Fig. 1: Phenotypic responses of the bulk and single-cell mouse cohorts. a-e, Body weight (**a**), running distance (**b**), fasting glucose (**c**), caloric intake (**e**), and glucose tolerance test (GTT) result for mice used in bulk and single-cell analysis across the four intervention groups. There is no statistically significant difference between the two cohorts for the meatrics shown. Statistical comparisons were performed using two way ANOVA. ns, not significant; AUC, area under curve. Other abbreviations used in this figure appear in the Methods.

bioRxiv preprint doi: https://doi.org/10.1101/2021.11.22.469622; this version posted November 23, 2021. The copyright holder for this preprint (which was not certified by peer review) is the author/funder, who has granted bioRxiv a license to display the preprint in perpetuity. It is made available under aCC-BY-NC-ND 4.0 International license.

Supplementary Fig. 2

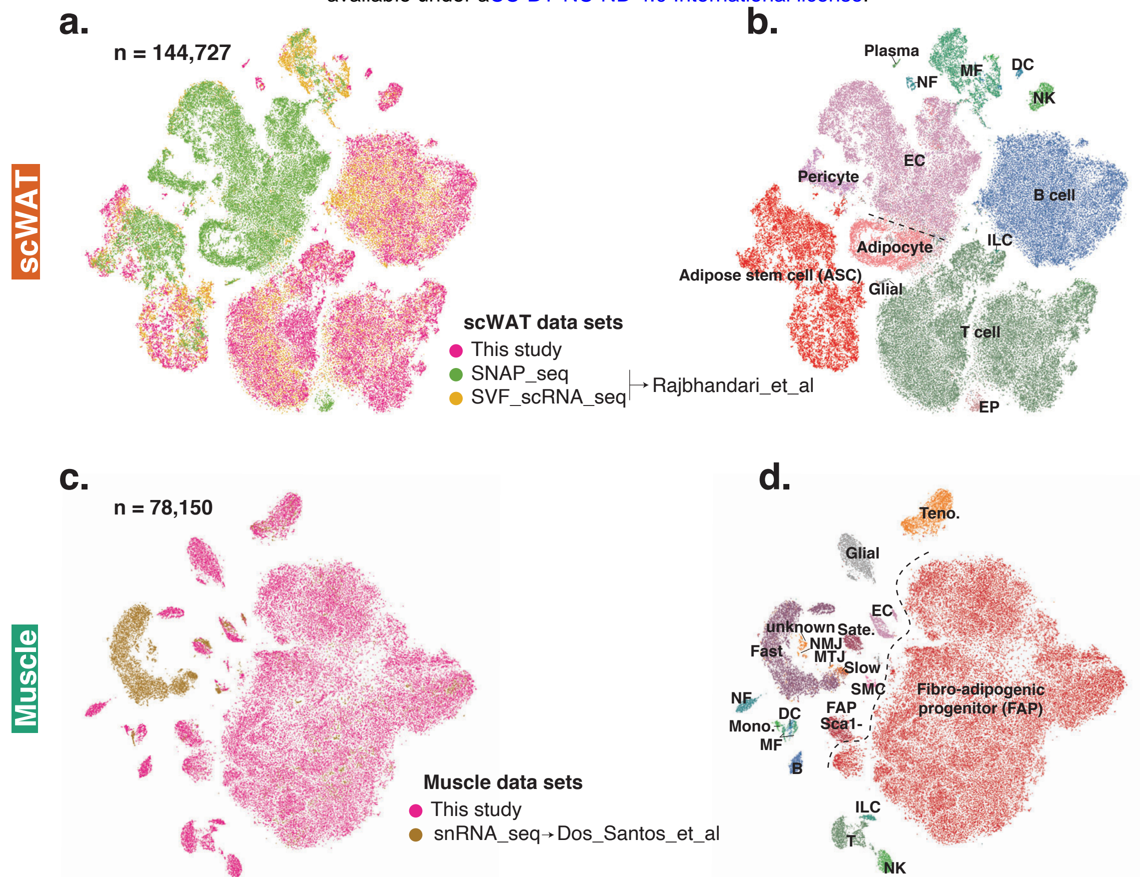

Supplementary Fig. 2: Integration of this study with tissue-matched publicly available single-cell studies. **a-b,** Single-cell clustering of 144,727 cells from this study and GSE133486. The UMAP plot is coloured by study (**a**) and cell type (**b**). **c-d,** Single-cell clustering of 78,150 cells from this study and GSE150065. The UMAP plot is coloured by study (**c**) and cell type (**d**). A list of abbreviations used in this figure appear in the Methods.

bioRxiv preprint doi: https://doi.org/10.1101/2021.11.22.469622; this version posted November 23, 2021. The copyright holder for this preprint (which was not certified by peer review) is the author/funder, who has granted bioRxiv a license to display the preprint in perpetuity. It is made available under aCC-BY-NC-ND 4.0 International license.

Supplementary Fig. 3

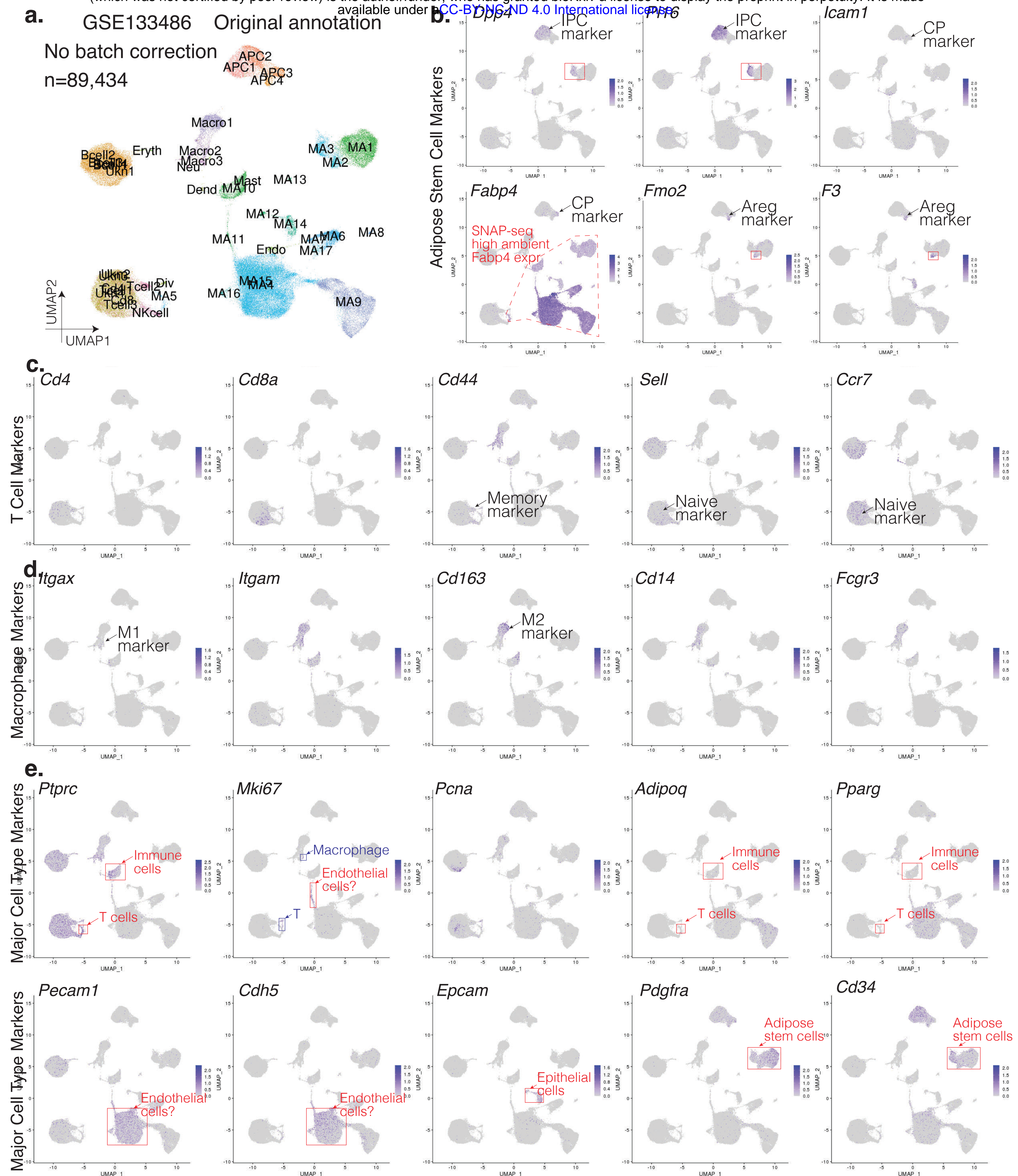

Supplementary Fig. 3: Original cell type annotation and marker gene expression for a single-cell mouse subcutaneous white adipose tissue study. a, Single-cell clustering of 89,434 cells in GSE133486. The UMAP plot is coloured by original cell type annotation provided by the authors. MA, mature adipocyte; APC, adipose progenitor cell; Dend, dendritic cell; Macro, macrophage; Neu, neutrophil; Endo, endothelial cell; Div, dividing

bioRxiv preprint doi: https://doi.org/10.1101/2021.11.22.469622; this version posted November 23, 2021. The copyright holder for this preprint (which was not certified by peer review) is the author/funder, who has granted bioRxiv a license to display the preprint in perpetuity. It is made available under aCC-BY-NC-ND 4.0 International license.

cell; Eryth, erythrocyte; Ukn, unknown. **b–f**, Marker gene expression for adipose stem cell (**b**), T-cell (**c**), macrophage (**d**), and other major cell types (**e**). Cell clusters with uncertain marker gene expression are boxed. A list of abbreviations used in this figure appear in the Methods.

bioRxiv preprint doi: https://doi.org/10.1101/2021.11.22.469622; this version posted November 23, 2021. The copyright holder for this preprint (which was not certified by peer review) is the author/funder, who has granted bioRxiv a license to display the preprint in perpetuity. It is made available under aCC-BY-NC-ND 4.0 International license.

Supplementary Fig. 4

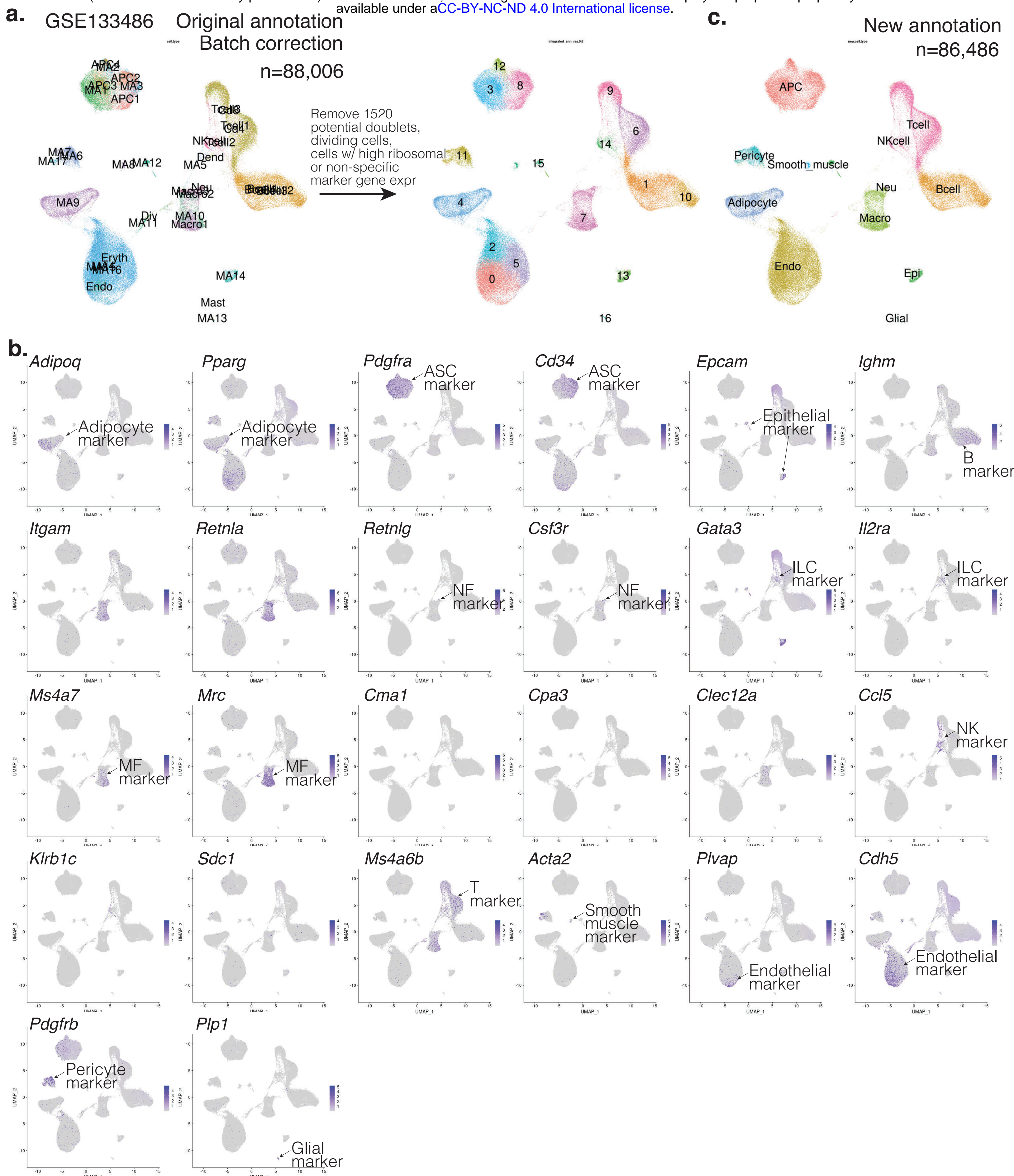

bioRxiv preprint doi: https://doi.org/10.1101/2021.11.22.469622; this version posted November 23, 2021. The copyright holder for this preprint (which was not certified by peer review) is the author/funder, who has granted bioRxiv a license to display the preprint in perpetuity. It is made available under aCC-BY-NC-ND 4.0 International license.

Supplementary Fig. 4 (cont'd)

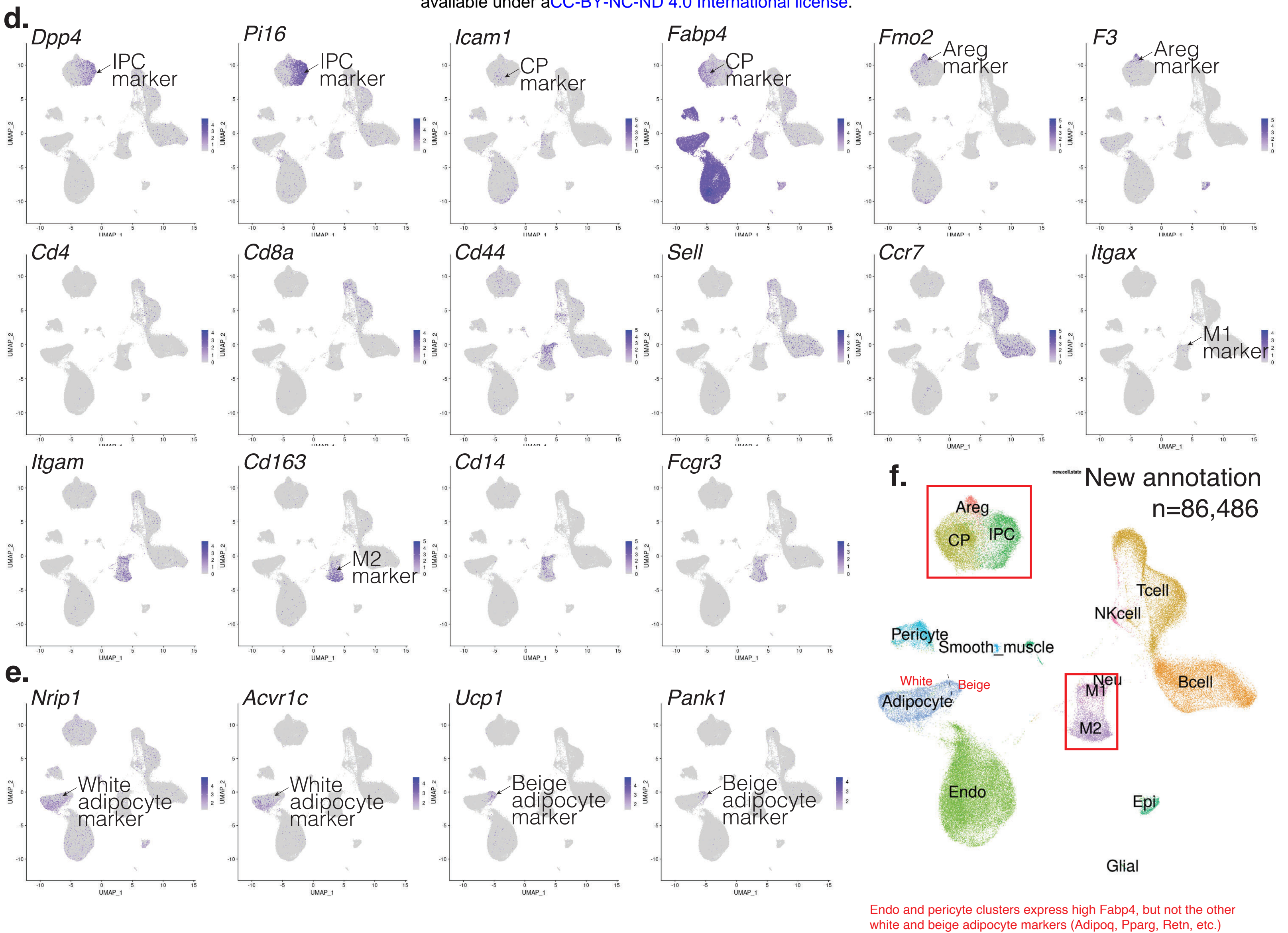

Supplementary Fig. 4: New cell type and state annotation and marker gene expression for GSE133486. **a,** QC, batch correction, and de novo clustering of the single-cell data set. **b,** Cell-type marker gene expression. **c,** New cell type labels assigned to each cluster after QC and batch correction. **d,** Cell-state marker gene expression. **e,** White and beige adipocyte marker gene expression. **f,** New cell state labels. A list of abbreviations used in this figure appear in the Methods.

bioRxiv preprint doi: https://doi.org/10.1101/2021.11.22.469622; this version posted November 23, 2021. The copyright holder for this preprint (which was not certified by peer review) is the author/funder, who has granted bioRxiv a license to display the preprint in perpetuity. It is made available under aCC-BY-NC-ND 4.0 International license.

Supplementary Fig. 5

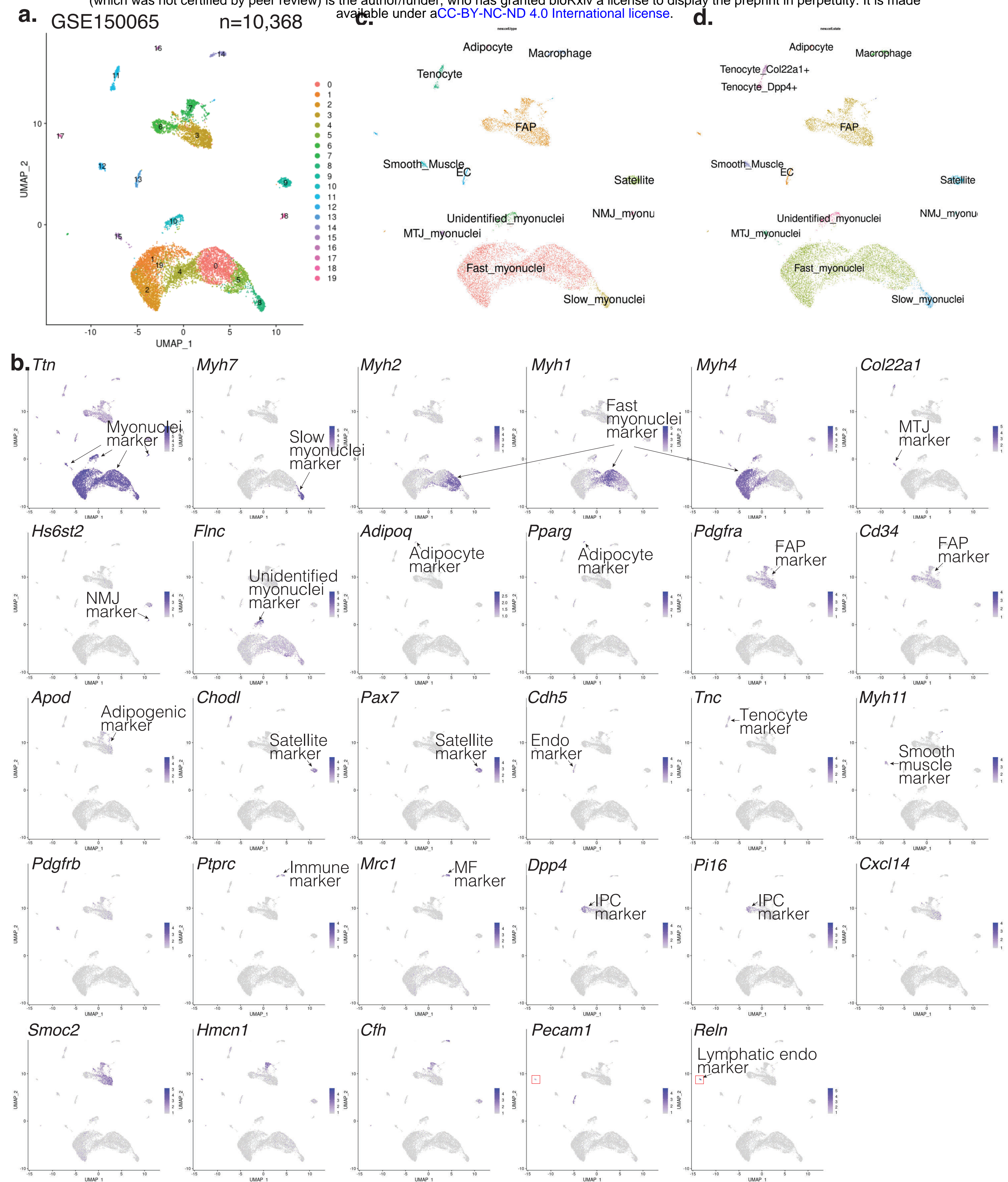

Supplementary Fig. 5: Original cell type annotation and marker gene expression for a single-cell mouse skeletal muscle study. a, Single-cell clustering of 10,368 cells in GSE150065. The UMAP plot is coloured by clusters. **b,** Cell-type marker gene expression. **c,** Same UMAP plot coloured by original cell type labels provided by the authors. **d,** Further split of tenocytes into two states. MTJ, myotendinous junction specialization; NMJ,

bioRxiv preprint doi: https://doi.org/10.1101/2021.11.22.469622; this version posted November 23, 2021. The copyright holder for this preprint (which was not certified by peer review) is the author/funder, who has granted bioRxiv a license to display the preprint in perpetuity. It is made available under aCC-BY-NC-ND 4.0 International license.

neuromuscular junction. Other abbreviations used in this figure appear in the Methods.

bioRxiv preprint doi: https://doi.org/10.1101/2021.11.22.469622; this version posted November 23, 2021. The copyright holder for this preprint (which was not certified by peer review) is the author/funder, who has granted bioRxiv a license to display the preprint in perpetuity. It is made available under aCC-BY-NC-ND 4.0 International license.

Supplementary Fig. 6

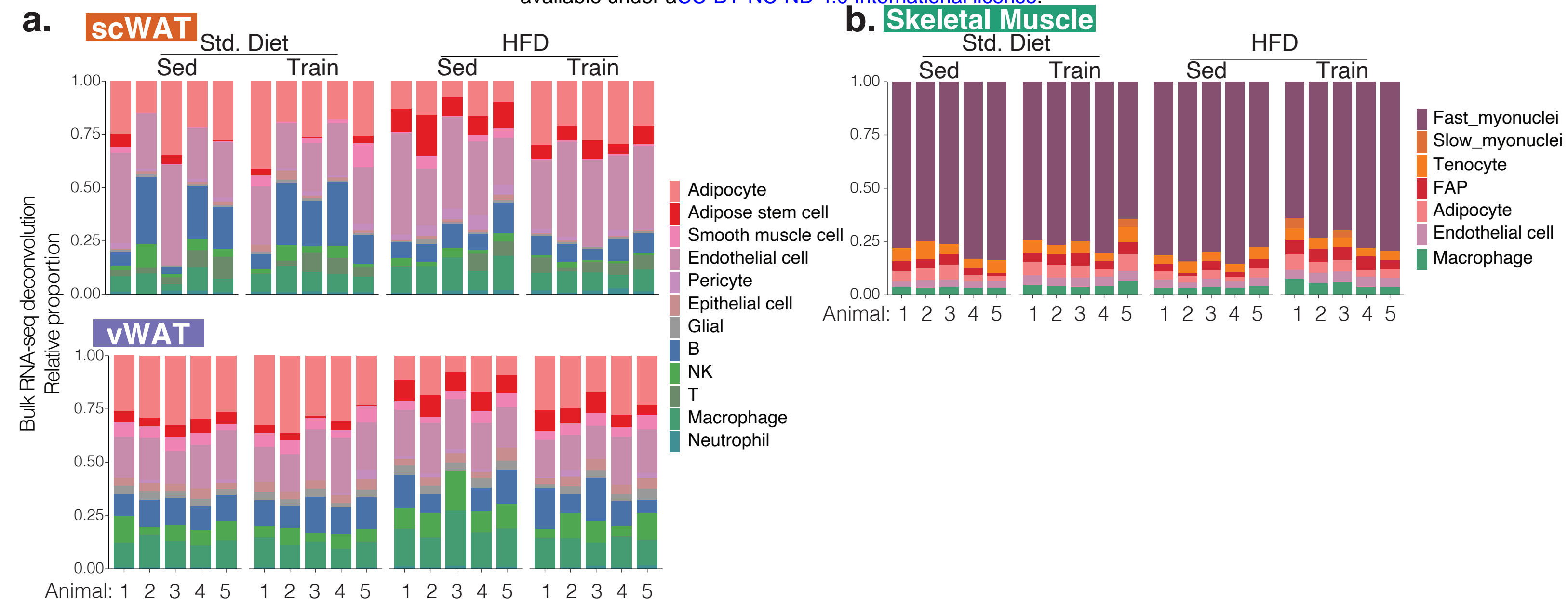

Supplementary Fig. 6: Sample-specific deconvolution. a-b, Relative cell-type proportions in each sample after deconvolving bulk RNA-seq data from two WAT depots (**a**) and skeletal muscle (**b**). Each bar is coloured by cell type.

bioRxiv preprint doi: https://doi.org/10.1101/2021.11.22.469622; this version posted November 23, 2021. The copyright holder for this preprint (which was not certified by peer review) is the author/funder, who has granted bioRxiv a license to display the preprint in perpetuity. It is made available under aCC-BY-NC-ND 4.0 International license.

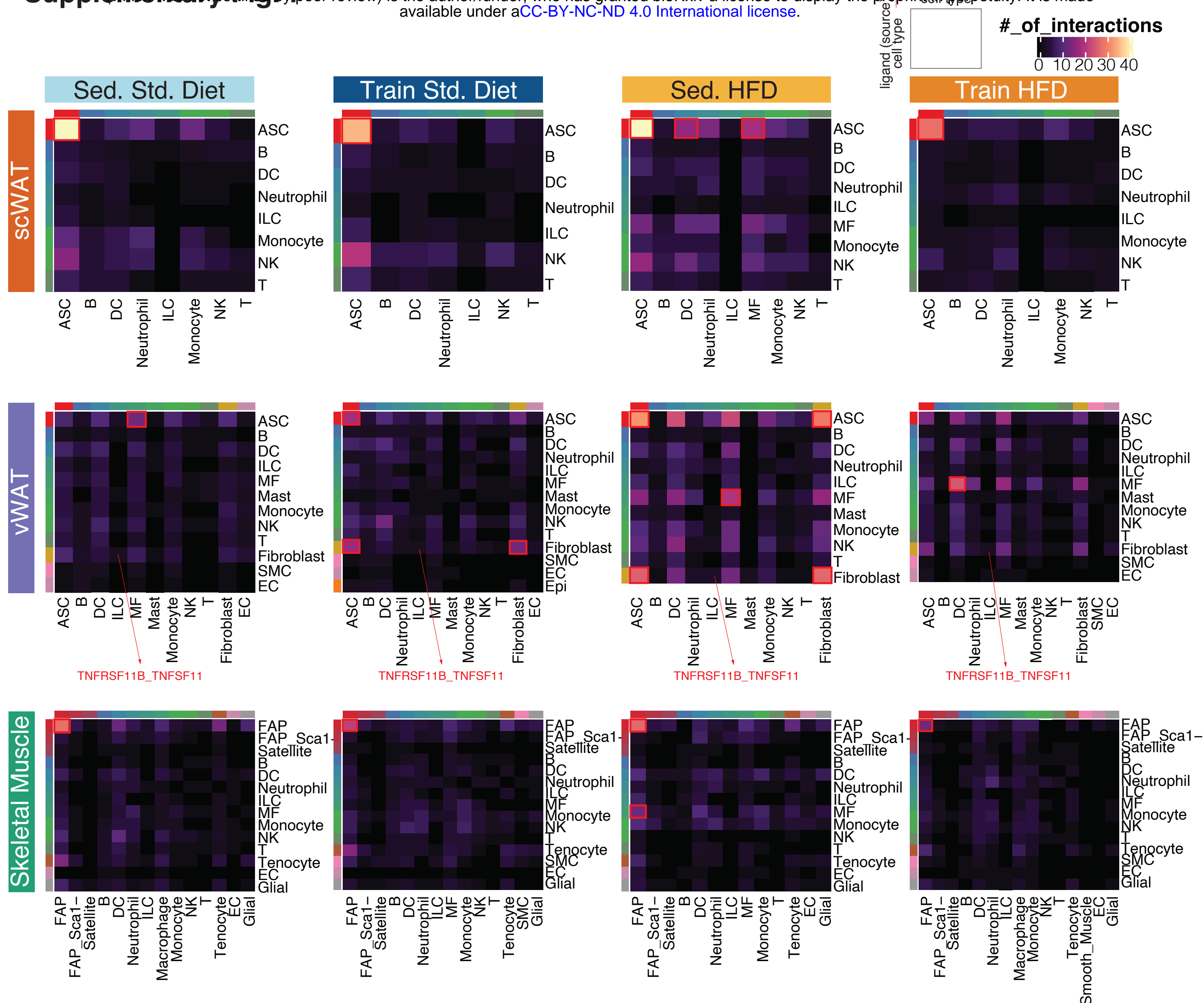

Supplementary Fig. 7: Within-tissue communication at cell-type level. Within-tissue ligand-receptor networks across the three tissues (row panels) in the four intervention groups (column panels). Number of interactions (heatmaps) between source cell types with ligand (rows) and target cell types with interacting receptors (columns) are plotted. Cell-type pairs with relatively higher number of interactions in each heatmap are highlighted using red rectangles. A list of abbreviations used in this figure appear in the Methods.

bioRxiv preprint doi: https://doi.org/10.1101/2021.11.22.469622; this version posted November 23, 2021. The copyright holder for this preprint (which was not certified by peer review) is the author/funder, who has granted bioRxiv a license to display the preprint in perpetuity. It is made available under aCC-BY-NC-ND 4.0 International license.

Supplementary Fig. 8

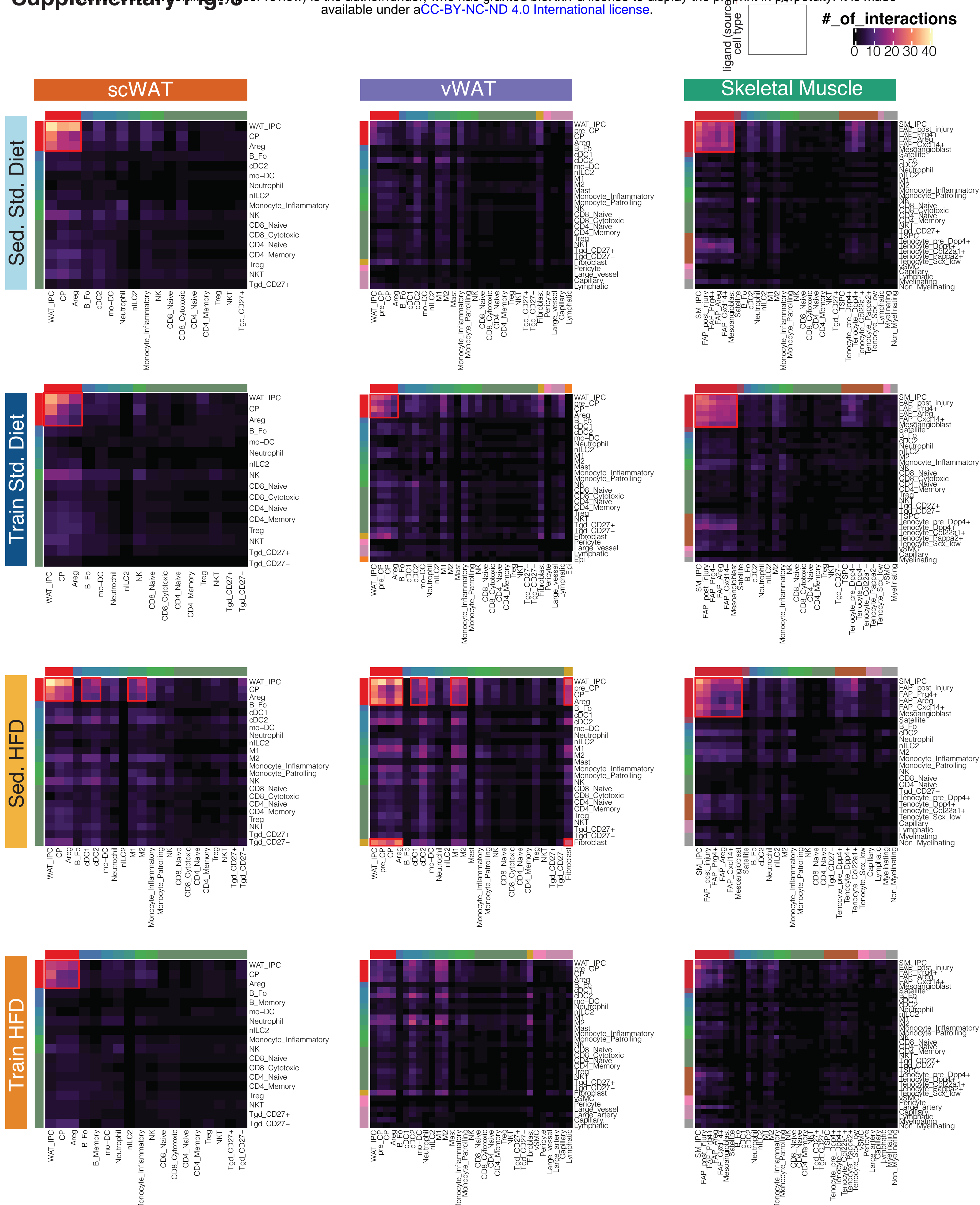

Supplementary Fig. 8: Within-tissue communication at cell-state level. Within-tissue ligand-receptor networks across the three tissues (column panels) in the four intervention groups (row panels). Number of interactions

bioRxiv preprint doi: https://doi.org/10.1101/2021.11.22.469622; this version posted November 23, 2021. The copyright holder for this preprint (which was not certified by peer review) is the author/funder, who has granted bioRxiv a license to display the preprint in perpetuity. It is made available under aCC-BY-NC-ND 4.0 International license.

(heatmaps) between source cell states with ligand (rows) and target cell states with interacting receptors (columns) are plotted. Cell-state pairs with relatively higher number of interactions in each heatmap are highlighted using red rectangles. A list of abbreviations used in this figure appear in the Methods.

bioRxiv preprint doi: https://doi.org/10.1101/2021.11.22.469622; this version posted November 23, 2021. The copyright holder for this preprint (which was not certified by peer review) is the author/funder, who has granted bioRxiv a license to display the preprint in perpetuity. It is made available under aCC-BY-NC-ND 4.0 International license.

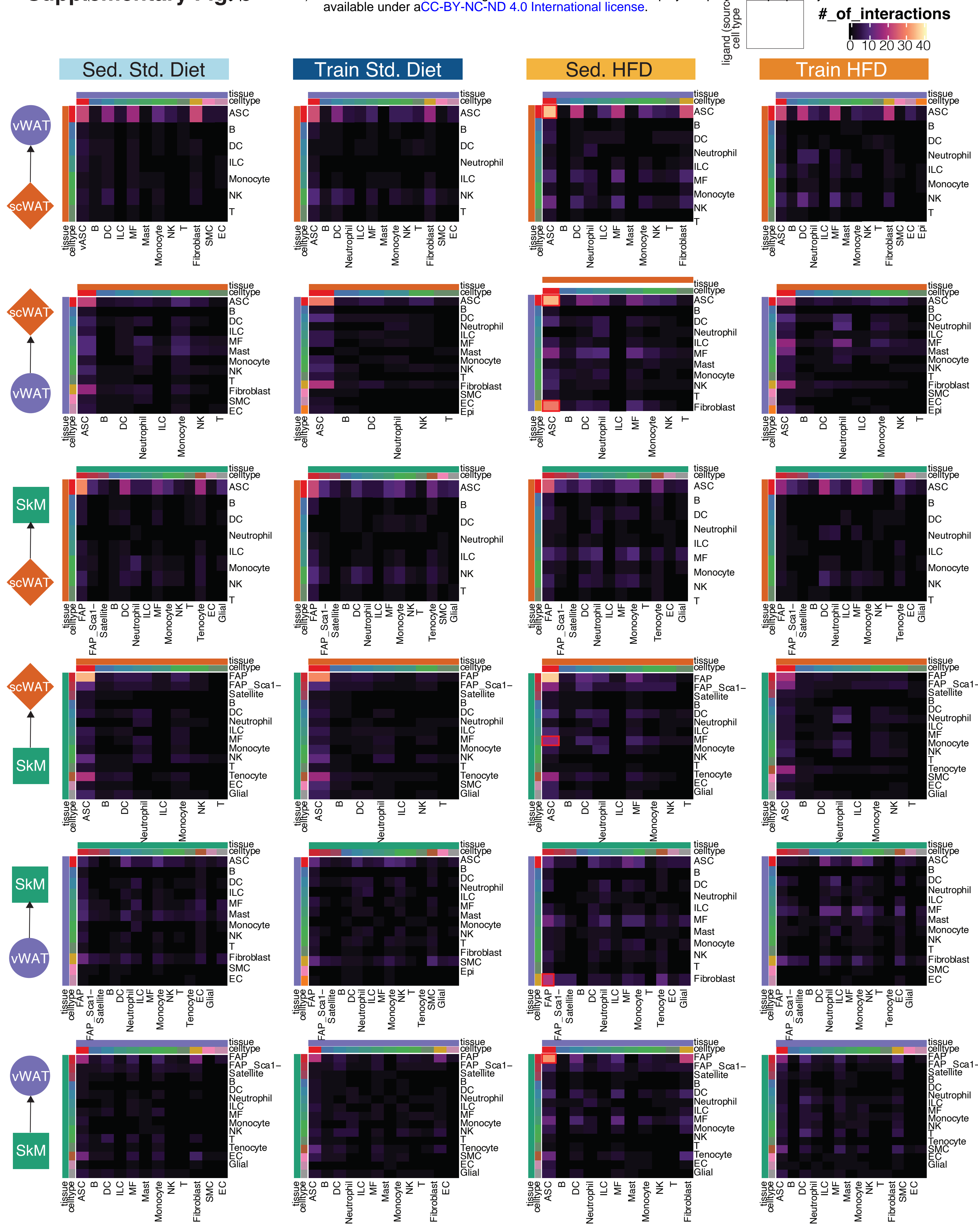

bioRxiv preprint doi: https://doi.org/10.1101/2021.11.22.469622; this version posted November 23, 2021. The copyright holder for this preprint (which was not certified by peer review) is the author/funder, who has granted bioRxiv a license to display the preprint in perpetuity. It is made available under aCC-BY-NC-ND 4.0 International license.

Supplementary Fig. 9: Cross-tissue communication at cell-type level. Cross-tissue ligand-receptor networks across tissue pairs (row panels) in the four intervention groups (column panels). Number of interactions (heatmaps) between source-tissue cell types with ligand (rows) and target-tissue cell types with interacting receptors (columns) are plotted. Cell-type pairs with relatively higher number of interactions in each heatmap are highlighted using red rectangles. A list of abbreviations used in this figure appear in the Methods.

bioRxiv preprint doi: https://doi.org/10.1101/2021.11.22.469622; this version posted November 23, 2021. The copyright holder for this preprint (which was not certified by peer review) is the author/funder, who has granted bioRxiv a license to display the preprint in perpetuity. It is made available under aCC-BY-NC-ND 4.0 International license.

Supplementary Fig. 10

ligand (source) cell type

receptor (target) cell type

#_of_interactions

0 10 20 30 40

	Sed. Std. Diet	Train Std. Diet	Sed. HFD	Train HFD
scWAT → vWAT				
vWAT → scWAT				
scWAT → SkM				
SkM → scWAT				
vWAT → SkM				
SkM → vWAT				

tissue

celltype

WAT_IPC, pre_CP, CP, Areg, B_Fo, B_Memory, cDC1, cDC2, mo–DC, Neutrophil, nILC2, M1, M2, Mast, Monocyte_Inflammatory, Monocyte_Patrolling, NK, CD8_Naive, CD8_Cytotoxic, CD4_Naive, CD4_Memory, Treg, NKT, Tgd_CD27+, Tgd_CD27–, Fibroblast, VSMC, Pericyte, Large_vessel, Large_artery, Capillary, Lymphatic, Epi

SM_IPC, FAP_post_injury, FAP_Prg4+, FAP_Areg, FAP_Cxcl14+, Mesoangioblast, Satellite, TSPC, Tenocyte_pre_Dpp4+, Tenocyte_Dpp4+, Tenocyte_Col22a1+, Tenocyte_Pappa2+, Tenocyte_Scx_low, Myelinating, Non_Myelinating

bioRxiv preprint doi: https://doi.org/10.1101/2021.11.22.469622; this version posted November 23, 2021. The copyright holder for this preprint (which was not certified by peer review) is the author/funder, who has granted bioRxiv a license to display the preprint in perpetuity. It is made available under aCC-BY-NC-ND 4.0 International license.

Supplementary Fig. 10: Cross-tissue communication at cell-state level. Cross-tissue ligand-receptor networks across tissue pairs (row panels) in the four intervention groups (column panels). Number of interactions (heatmaps) between source-tissue cell states with ligand (rows) and target-tissue cell states with interacting receptors (columns) are plotted. Cell-state pairs with relatively higher number of interactions in each heatmap are highlighted using red rectangles. A list of abbreviations used in this figure appear in the Methods.